Thèse présentée pour obtenir le grade de
Docteur de l'Université de Strasbourg

Discipline : Mécanique des Fluides
par **Tanvir Akbar**

Simulation of three-dimensional flows past infinite cylindrical bodies

Thèse soutenue publiquement le 9 novembre 2010

Membres du jury

Directeur de thèse :	M. J. Dušek, Professeur, UdS (Strasbourg)
Rapporteur externe :	M. D. Sipp, DR, ONERA DAFE Meudon
Rapporteur externe :	M. C. Nouar, DR CNRS, LEMTA Nancy
Examinateur :	M. J. E. Wesfreid, DR CNRS, PMMH Paris
Membre invité :	M. G. Bouchet, CR CNRS, IUSTI Marseille

First of all I would like to say thank to almighty GOD who gave me strength, courage and health to fulfill the requirements of this dissertation.

I would like to express the deepest gratitude to my director of thesis, the **Professor Dr. Jan Dušek** whose untiring effort, commitment, guidance and valuable suggestions enabled me greatly in the understanding and writing of this dissertation. He has the attitude and the substance of genius. I know I have not been the best student but I found him always to help when needed. Without his supervision and endless support this dissertation would not have been possible.

I gratefully acknowledge **Dr. Gilles Bouchet**, my co-director of thesis for his advice, assistance and indispensable contribution from learning of code to the writing of this thesis. He provided me support in various ways to during thesis with immense cooperation and guidance. His sincere involvement, active role and helpful suggestions paved the way to complete this study.

I am also pleased to say thanks to **Dr. Yannick Hoarau** for his support in learning CFD softwares and sharing informations about free CFD codes. It will benefit me for a long time to come.

I would like to say thanks to **Professor Dr. Saleem Asghar** who encouraged me to pursue Ph.D in France when I was in a hesitation. I can not forget his sincerity and encouragement.I also thankful to **Dr. Tasawar Hayat** for his help in my studies.

I am thankful to all Ph.D. students at IMFS especially students of ITD group whose presence created a good environment and made my three years stay more enjoyable. A bundle of thanks in particular to Miroslav Kotouč, Vít Nováček, Thibaut Deloze, Cyril Loux, Hassan Ilmi, Monisha Mridha, Emilie Diaz, Elena, Marcin Chrust, Tapia-Padilla Gabriela, Abdel Hakim Benslimane, Quentin Araud and Rabih Ghostine who made my each day in the laboratory pleasant. It is pleasant to mention: Qamar Iqbal, Elise and Ayman Hazzouri for their moral support and making sure life is not suppressing and dull.

I extends my sincere gratitude to HEC, Pakistan for financial support through out my stay in France.

Words fail to express the tremendous support and love from my family. My mother deserves special mention for her inseparable support and prayers. She waited long time to see me again. I am thankful to my brothers and a sister for their love and care.

Finally, I would like to thank many individuals and friends who have not been mentioned here but were important to accomplish this work successfully.

Contents

Latin letters :

c	[m]	Chord length
d	[m]	Diameter of cylinder
D	[m]	Large diameter of torus
E_m	[J]	Energy
f	[s^{-1}]	Frequency
$\mathbf{F}_D$	[N]	Drag force
$\mathbf{F}_L$	[N]	Lift force
m	[–]	Fourier mode
M	[–]	Fundamental mode
p	[Pa]	pressure
t	[s]	Time
T	[s]	Time period
t_{eff}	[m]	Effective thickness
$\mathbf{U}_\infty$	[m/s]	Free stream velocity
u, v, w	[m/s]	Velocity components
$\mathbf{v}$	[m/s]	Velocity field

Greek letters :

α	[degree]	Angle
ρ	[kg/m^3]	Density of the fluid
ν	[m^2/s]	Kinematic viscosity
λ	[m]	Wavelength
ξ		Percent shift of Strouhal number

Nondimensionlized numbers :

Ar	Aspect ratio
C_D	Drag coefficient
C_L	Lift coefficient
Re	Reynolds number
St	Strouhal number
$C_{f,z,1}$	Skin friction coefficient

Chapter 1

Introduction

The problem of understanding the flow past an airfoil cast the foundation of the present day aerodynamics as early as in the end of the nineteenth century and has remained topical until nowadays. It consists in predicting the lift force acting on an aerodynamically profiled cylindrical body aiming at an optimal design of aircraft wings. Beyond this original application, many machines, such as turbines and compressors, operate on the principle of hydrodynamic lift. The physical origin of the hydrodynamic lift is presented in any textbook introduction of fluid mechanics and is easily understood in terms of the Bernoulli equation and the pressure difference between the pressure and suction side of the airfoil. The quantitative prediction of the lift required, however, a mathematical representation of the velocity field. The simplest model consists in neglecting viscosity effects in the boundary layer and in the wake and solve the problem within the framework of the theory of irrotational (potential) flows. In the case of the well-known Zhukovsky airfoil it is thus possible to derive a very simple analytical formula relying directly the lift coefficient

$$C_L = \frac{F_L}{0.5\rho U^2 c}, \tag{1.1}$$

where F_L is the lift force per unit spanwise length, ρ is the density of the fluid (air), U the (asymptotic) velocity of the flow and c stands for the chord length, to the angle of attack α and the angle β characterizing the camber (see e.g. Chassaing, 1997)

$$C_L = 2\pi \sin(\alpha + \beta). \tag{1.2}$$

In Eq. (1.2) the sign of β is chosen so that the camber enhances the effect of the angle of attack. The simple textbook theory of the Zhukovsky profile agrees amazingly well with experimental observations provided the thickness of the airfoil is thin and the angle of attack is sufficiently small. For this reason, the potential flow theory is known also as a 'thin airfoil theory'. For symmetric thin profiles at angles exceeding 12 degrees the lift suddenly drops. This drop is due to the flow detachment at the suction side of the airfoil. The detached flow is strongly rotational and invalidates the assumption of the potential flow theory. The sudden drop of lift is called stall in aerodynamics. Stall is to be avoided in exploiting the airfoils not only because of the drop of the lift but also because of a sudden increase of the

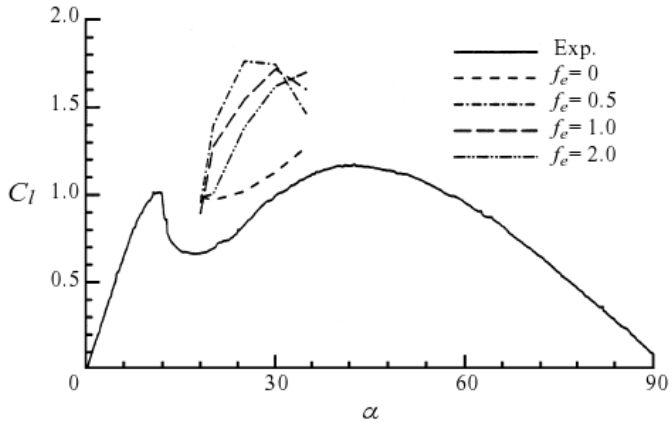

Figure 1.1: Mean lift coefficient of a NACA 0012 airfoil from Wu *et al.* (1998) as a function of the angle of attack (full line). The dotted lines represent numerical results of periodic forcing of the boundary layer close to the leading edge.

drag. Actually, the lift drops only within a limited interval of angles to reach a maximum at an angle close to 45 degrees (see figure 1.1). But, in this case, the 'lift' is nothing more than a projection of a very strong drag. The drop of the lift and the increase of drag combine in reducing the lift/drag ratio, which in aeronautical practice renders planes uncontrollable and causes accidents.

In turbo-machines the stall has less dramatic consequences but limits considerably the flexibility of their operation and reduces their efficiency. In many cases, the movement of the profiles (blades) is accompanied by periodic pitching or rotation, the conditions of the stall onset are dynamic and the stall is called dynamic.

1.1 Simulation of three-dimensional flows past an airfoil

A significant effort has been done to investigate the stall both experimentally and by numerical simulations with the purpose to predict it and, possibly, to delay its onset by flow control. The numerical simulations being, nowadays, an inherent part of any industrial design, many numerical approaches have been used to simulate flows past airfoils. In view of the practical importance of the topic it is natural that the scope of the bibliography is enormous. For a self-contained overview it is therefore necessary to limit, from the start, the bibliographic presentation to publications with a special focus on the stall. The latter being related to the detachment of the boundary layer, it can not be understood without taking into account viscous effects, which puts all inviscid, mostly compressible, simulations outside the scope of the present bibliographic summary. Regarding the airfoil, the length scales are generally non-dimensionalized with respect to the chord length c. The Reynolds and Strouhal numbers mentioned in this section are thus based on the chord length:

$$Re = \frac{U_\infty c}{\nu}, \quad St = \frac{fc}{U_\infty}. \tag{1.3}$$

Still today, the practically most successful method consists in combining potential flow equations with boundary layer ones and a simple turbulence model fitted to observations of the boundary layer detachment (see http://foilivier.free.fr/fr/xfoil.htm). The idea goes back to Prandtl (1905) at the beginning of the 20th century (see also Schlichting, 1955). A very recent paper by Sandham (2008) demonstrates the ability of such a simple model to reproduce not only the detachment and re-attachment of the boundary layer in excellent agreement with experimental data but also to simulate large scale flow oscillations in the resulting wake. The reliability of this type of modeling depends on the 'transition model' using experimental data for tuning the model in such a way that the laminar-turbulent transition in the boundary layer agrees with expectations. For all its practical utility, such an approach has a limited predictivity. To improve the predictivity of the boundary layer theory a significant effort has been done in investigating the details of the boundary layer separation by numerical simulations. In spite of the considerable simplification of the problem configuration, the direct numerical simulations (DNS) of the turbulent boundary require considerable computing resources (see Alam & Sandham, 2000) without contributing to much more than some insight into the structure of the turbulent bubble arising in the case of a small flow detachment. They do not help in predicting the location of the detachment because the latter is determined by large scale factors such as the distance from the front stagnation point, the curvature of boundary layer and the outer flow. For this reason, the simulation of the entire flow past the profile appears to be the only way of obtaining more quantitative predictions.

Originally, the computer power was insufficient to tackle fully three-dimensional simulations. But two-dimensional simulations are still nowadays a frequent compromise between the need for resolving the fine laminar boundary layer and the available computing resources. Virtually all the papers cited below for their three-dimensional simulations present also 2D results. Wu *et al.* (1998) attempt to reproduce numerically the flow control of a post stall massive flow separation. They use a compressible formulation but at a low Mach number (0.2). The considered angle of attacks go from 18 to 35 degrees. To represent a realistic flow at high Reynolds number (5×10^5) turbulence modeling must be used (Baldwin-Lomax and Spalart-Adams models). As is the case in virtually all work based on turbulence modeling, the results are at the best qualitatively correct. Instead of focusing on a quantitative simulation, the paper presents a series of interesting qualitative results that can, however, be observed also in low Reynolds flows, such as the vortex dynamics and frequency lock-in. It is interesting to cite the reasons for the failure to reproduce the lift of the unforced configuration (overestimated by about 25%): "In effect, even for a two-dimensional airfoil, the real turbulent flow is inherently three-dimensional, with wavelength of spanwise fluctuations comparable to the size of eddies that can be resolved by two dimensional Reynolds-averaged computation. Moreover, small eddies formed from the disturbed shear layer could have an important effect on the evolution of massively separated flows and their control, but they could have been smeared out by the Reynolds-averaged approach. Therefore, all two-dimensional computations at Reynolds average level, ... , by no means faithfully simulate these kinds of

complicated flows." It can be concluded that turbulence modeling has rather a negative impact on the predictivity of numerical simulations. This probably explains the large amount of DNS in the latest literature. A similar simulation method is presented also by Mittal & Saxena (2002) to investigate, again just qualitatively, the hysteresis of the detachment and re-attachment of the flow on the suction side of the airfoil when the angle of attack is progressively increased and decreased.

With the recent significant increase of available computer power many fully three - dimensional DNS have been reported. Quite many DNS have been carried out in the compressible formulation but, as a rule, the Mach numbers are small (typically 0.2) and the compressibility effects are inessential. As the result, compressible and incompressible simulations can be considered as comparable. The geometrical configuration is virtually always that of a NACA 0012 airfoil. The considered angle of attacks and Reynolds numbers are almost never the same for two distinct publications and, due to the computing costs, never more than a single 3D simulation is presented each time. A very important feature of the 3 dimensional simulations is the choice of the simulated spanwise length. Assuming the 'real' configuration to be infinite in the spanwise direction, the question is what spanwise length scale is to be considered to capture the essential dynamics. The 'infinity' of the spanwise direction is simulated by a spanwise periodicity condition. It remains, however, clear that the length of the spanwise period seriously limits the spanwise length scale of the simulated structures. The tradeoff is of high importance because the computing resources are always strained to their limit in this type of DNS. As a consequence, the increase of the spanwise length scale implies automatically a worse resolution of the small scales. The choice varies from 0.1 chord length to 4 chord lengths in the available literature.

Hoarau *et al.* (2003*a*), Hoarau *et al.* (2003*b*) and Hoarau *et al.* (2006) present 3D DNS of an incompressible flow past a NACA 0012 profile with 20^o of incidence at $Re = 800$. The spanwise period is 4 and 12 chords. It is remarked that the simulation with a spanwise period of 12 chords yields the same results, which explains why only those obtained with 4 chords are presented. In this case the number of mesh points is 2.6×10^6, the smallest resolved spanwise scale being about 0.04 chord. The focus of the cited papers is on the three-dimensional spanwise structures appearing in the wake. The principal contribution consists in setting the analogy between the circular cylinder wake and that of the wing. Indeed, if the equivalent transverse thickness $D = c \sin\alpha$ where c is the chord length and α the incidence angle (20^o) is introduced, the considered regime ($Re = 800$, based on the chord length) corresponds to $Re = 273$ based on the equivalent thickness D and puts it to the interval in which the mode B (see below) dominates in the circular cylinder wake. The wavelength of spanwise structures is found to be in an excellent agreement with the wavelength of the mode B at the same Reynolds number of 270.

A very similar numerical method to that used several times for simulating the flow past a circular cylinder (see references below) was used by Stoevesandt *et al.* (2006). It consists in a high order finite element (spectral element) discretization of the transverse-downstream plane combined with a spectral Fourier expansion spanwise. This numerical approach is almost optimal because of the possibility to concentrate the computing effort to the boundary layer and the wake and of the high accuracy of the spanwise Fourier expansion. The angle of attack considered in the paper is 12^o, i.e. at the generally accepted incidence at which the

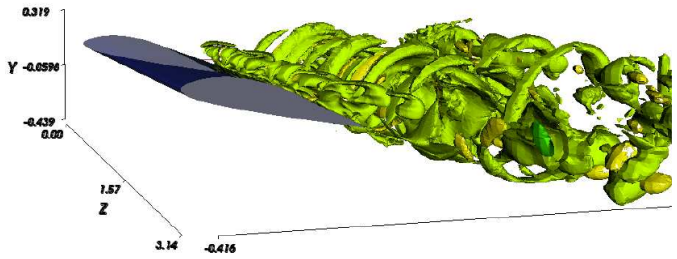

Figure 1.2: Iso surfaces of the spanwise velocity component on the fx-w151a airfoil used in wind turbines (see Stoevesandt *et al.*, 2006).

stall sets in. The Reynolds number 5000 allowed the authors to solve for all the scales present in the flow. Exceptionally, the airfoil is not a NACA 0012 profile but an airfoil used in wind turbines. The latter being non-symmetric, a direct comparison with a simulation of a flow past the (symmetric) NACA 00012 profile at the same incidence is not possible. The spanwise direction is solved with a period of πc and 64 Fourier modes are used in the expansion. A special care is taken to optimize the resolution of the flow in the transverse-streamwise plane. Higher order (up to 9th) elements are used around the airfoil and lower order (5th) in the far flow. Extremely fine elements are generated in the boundary layer. The resulting number of degrees of freedom of the simulation is 3.6×10^6. It is to be noted that the found average lift coefficient $C_L = 0.77$ remains significantly below the value of the potential flow theory of thin symmetric profile with the same angle of attack $2\pi \sin 12^o = 1.3$ although the camber of the airfoil should yield even a higher value. This is given by the still moderate Reynolds number and is in agreement with the boundary layer model calculation by xfoil. The flow is already massively separated at this incidence. The average drag coefficient is reported to be 0.2. The flow is dominated by a strong vortex shedding with a Strouhal number close to 1. These values may provide a good reference for further simulations in view of the care brought to the quality of the resolution, nevertheless, it is regrettable that the paper provides no quantitative data on the spanwise structures. The 3D plot in figure 1.2 of the spanwise velocity makes it possible to estimate the characteristic spanwise wavelength to be close to that found by Hoarau *et al.* (2003*b*).

A series of papers by Shan *et al.* (2005), Deng *et al.* (2007) and Shan *et al.* (2008) solve compressible Navier-Stokes equations at a low Mach number (0.2) using a sixth order finite difference scheme for a NACA 0012 profile with an angle of attack of 4^o in the first two cited papers and 6^o in the last one. The reported Reynolds number is 10^5 although a doubt is allowed concerning the adequacy of the spatial resolution at such a high Reynolds number even if the authors claim a grid size in the direction normal to the wall to be less than one wall unit. The spanwise length of the domain is $0.1c$ only. The used C-mesh contains a total number of points of about 7×10^6. The last cited paper used 9 million of points redistributed so as to bring a better resolution in the spanwise direction. The mesh of the first two papers was apparently insufficient to provide enough resolution in this direction with barely 32 points spanwise. The paper by Shan *et al.* (2005) presents a qualitative

analysis of the uncontrolled flow, the purpose of the paper by Deng *et al.* (2007) is mainly to investigate the effect of flow control. The weakness of the papers consists in the absence of quantitatively easily comparable data. E.g. no values of integral quantities, such as lift or drag are provided. The simulation reveals a flow separation on the suction side about $0.55c$ downstream of the leading edge. In the detached flow 'large' and 'small' turbulent structures are visible but their size is difficult to assess and the numerical parameters of the simulations let the reader assume that both the large and small spanwise structures have been truncated. The Strouhal number of the oscillations of the wake that can be estimated on the basis of the represented time plots lies between 3 and 4. The authors attribute the frequency to the Kelvin-Helmholtz instability. The same frequency dominates, however, the wake downstream of the trailing edge. It may, actually, correspond to that of the von Kármán vortex street. At the incidence of 6^o (see Shan *et al.*, 2008) the flow separates at $0.3c$ downstream of the leading edge. The resulting flow control investigated in the last two papers is relatively deceiving which is attributed by the authors to too small angles of attack considered.

As can be seen in the recent paper by Jones *et al.* (2008), realistic DNS of a flow past an airfoil, albeit at a regime still short of the real experimental conditions, remains a tremendous computational task. The paper presents a simulation of the flow past a NACA 0012 airfoil with incidence 5° at $Re = 5 \times 10^4$. This Reynolds number corresponds to an airfoil of 10cm of chord placed into a flow of 7 m/s. The solved equations are compressible Navier-Stokes equations at a Mach number of 0.4 using a fourth order finite difference scheme. The solver is fully explicit requiring a short time step $\Delta t = 10^{-4}$. The spatial discretization is based on a C-mesh in the downstream-transverse plane and is extended to 3D on a spanwise length of $0.2c$. The spanwise length scale is justified by (unpublished) data on the backward facing step and by the analogy between the flow past the step and past the detachment bubble arising on the suction side of the airfoil. The mesh refinement in the boundary layer and in the wake respect rather scrupulously the constraints resulting from the boundary layer thickness. The 2D mesh has been generated iteratively for this purpose, the spanwise extension appears, however, to be *ad hoc*, likely to fit within available computing resources. In spite of that the 3D mesh contains almost 2×10^8 grid points. A 2D simulation yields a separation of the flow 0.15 c downstream of the leading edge. The separation bubble re-attaches about $0.6c$ downstream of the leading edge where the unsteady vortex structures arise. The average lift coefficient is 0.5 in this case. This is quite close to the potential flow value (0.55), which probably witnesses of the quality of the resolution of the boundary layer. The mean drag coefficient is 0.03. The wake presents a von Kármán vortex street oscillating periodically with a Strouhal number reported to be 3.37. The 3D flow is forced artificially at the start but when the forcing is removed it remains self-sustained. The forcing has, obviously, (in view of the presented figures) the maximum available spanwise length scale. The nonlinear couplings transfer the forcing to all shorter scales in the same way as it occurs in the spectral Fourier expansion (see the chapter 3). The 3D turbulence breaks up the large scale ordered 2D vortex structures (see fig. 1.3) and results in an increase of lift by more than 20%. The figure shows clearly a thinner domain of detached flow as compared to the 2D simulation. Let us, however, note that this increase brings the lift above the potential flow theory prediction which has never been reported experimentally. The 'uncontrolled' turbulence also increases the drag

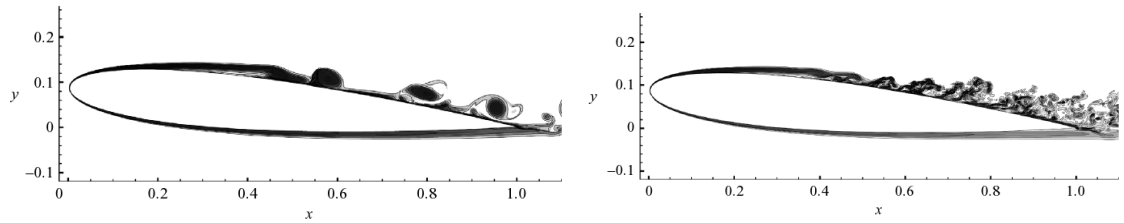

Figure 1.3: Iso-surfaces of vorticity, left figure: 2D simulation, right figure: 3D simulation by Jones *et al.* (2008).

(by 26%), however, the forced large scale spanwise modulation brings, to the contrary, a 10% drag reduction. The pressure coefficient plot (fig. 1.4) shows that this integral effect is the result of a higher pressure drop in the separation bubble and a later boundary layer re-attachment in the 3D case. As convincing as the results may be, there remains a concern with the chosen spanwise length scale. Indeed, the presented spanwise power spectrum not only does not present a maximum witnessing of the capture of the largest integral scale but it also sharply decreases starting from the largest captured length scale (see Fig. 1.5). This is also confirmed by the dominant large scale modulation in the 3D plot in figure 1.5. (The plot represents the invariant of Jeong & Hussain (1995).) The very convincing results of the paper would require some simplifying analysis. That presented by the authors is, however, of little interest. E.g., it is well known (see Noack *et al.*, 2003) that the linear analysis of an average turbulent flow can hardly yield a global instability.

It is clearly seen that, as soon as three-dimensional effects in flows past airfoils are to be taken into account tremendous numerical difficulties arise. In particular, even in the last cited, massive numerical simulation, doubts are allowed whether the most energetic spanwise scales have been captured. This may induce intolerable errors in predicting the onset of the stall which may be triggered by strong transient phenomena as indicated by Mittal & Saxena (2002). In view of the evidenced strong impact of the spanwise structures on the flow behaviour, it is to be feared that very large scale, albeit transient, structures may significantly influence the numerical predictions and can trigger an expected stall. A deeper understanding of the scales to be expected to arise in the spanwise direction is thus essential. The problem is common to all supposedly infinite geometrically cylindrical bodies independently of the form of their cross section. In this sense, the most significant theoretical progress has been achieved in investigating the wake of an infinite circular cylinder. The relevance of the results pertaining to the circular cylinder for the understanding of three-dimensional structures in the wake of airfoils has already been recognized by several authors (e.g. Hoarau *et al.*, 2003*a*). For this reason we devote the next section to an overview of the numerical and theoretical work on the transition to three-dimensionality of the flow past a circular cylinder.

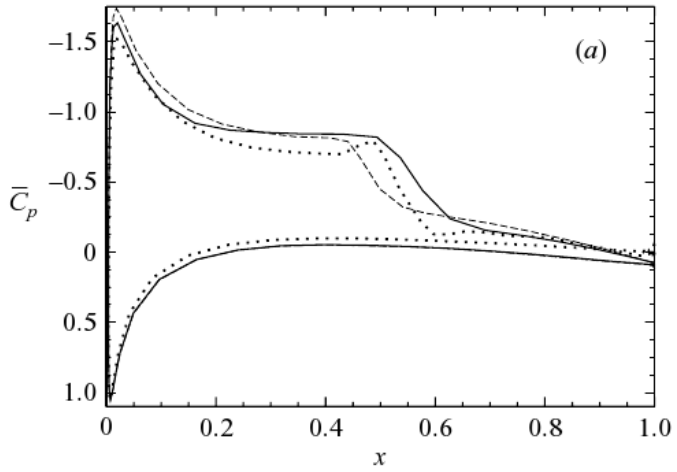

Figure 1.4: Time averaged distribution of pressure coefficient. The dotted line represents the $2D$ case, the dashed line represents the three-dimensional case with forcing and the full line represents unsteady the three-dimensional case without forcing. (Reproduced from Jones *et al.* (2008))

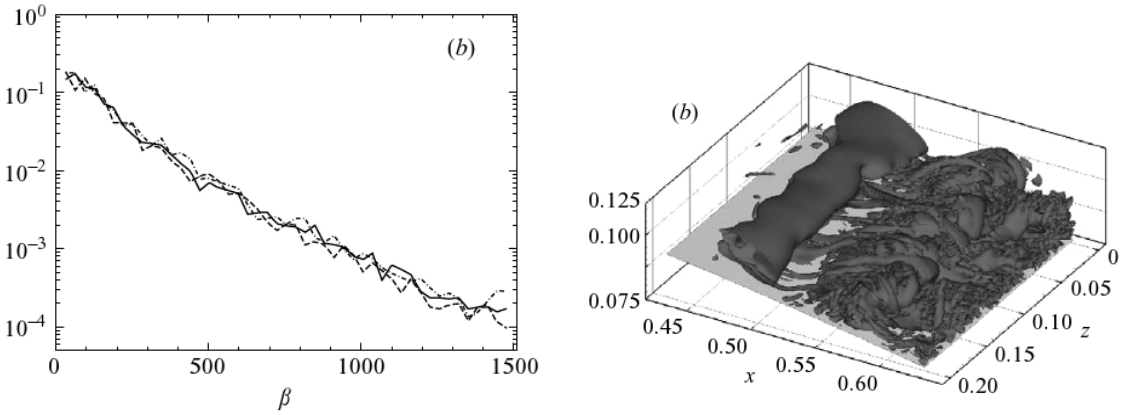

Figure 1.5: Left figure: Spanwise power spectra, integrated over the thickness of the boundary layer in the range of [1,50] wall units, for the three-dimensional case without forcing at $x = 0.8$ (-), $x = 0.9$ (–) and $x = 1.0$ (-.) x being the distance from the leading edge. Right figure: Iso-surfaces of the second invariant of the velocity gradient tensor at $Q = 500$ for the three-dimensional case without forcing. (Reproduced from Jones *et al.* (2008))

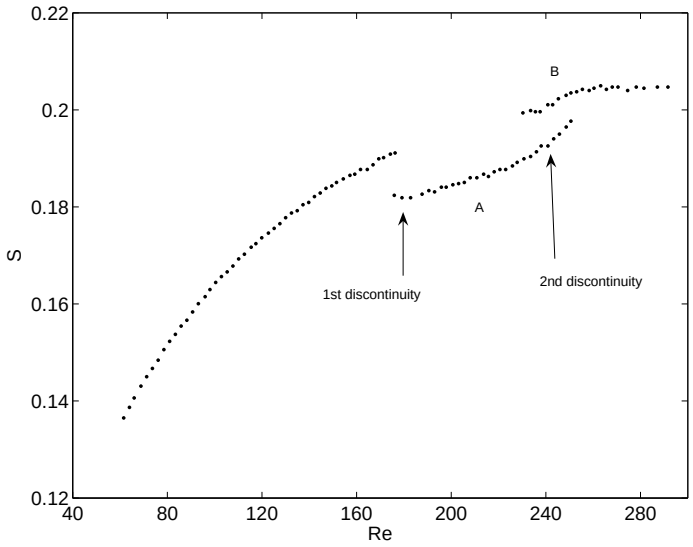

Figure 1.6: Strouhal number vs Reynolds number relationship over laminar and three-dimensional transition regimes. Two different discontinuities are associated to two instability modes, mode A and mode B.

1.2 Transition to three-dimensionality in the flow past a circular cylinder

The onset of turbulence in the wake of a cylinder has been the subject of an extensive research effort for more than 50 years. The leading thread of most papers published during the last 20 years has been the Strouhal (St)–Reynolds (Re) number relationship appearing for the first time in Williamson (1988a) and reproduced virtually in all papers dealing with the topic of the onset of instabilities and turbulence in the cylinder wake (see also fig. 1.6). The relationship aimed at obtaining a "universal and continuous" law relating the Strouhal number to a broad range of Reynolds numbers including the transition to turbulence. Precisely in the latter domain, the scatter of experimental results was impressive. Williamson attempted to improve the Roshko's Strouhal-Reynolds law (Roshko, 1954) by providing more reliable experimental results in the transitional domain. (Roshko published Strouhal number measurements over a wide range of Reynolds numbers and found a transition regime in the velocity fluctuations.) The Williamson's experimental curve appeared, however, to be neither continuous nor universal in spite of its accuracy, which triggered all the mentioned research effort.

The latter can be roughly divided into two main streams trying to bring an agreement between experimental observations on one hand and the theory and numerical results on the other hand. While the experimental work was concentrated on removing what was considered as artefacts, the theoretical and numerical one provided more and more realistic models. The earliest experimental results made it possible to explain the downward shift of

the law as compared to numerical simulations in the range of purely two-dimensional periodic vortex shedding by an obliqueness of shed vortices (Williamson, 1989), which in its turn suggested the idea to force parallel vortex shedding by controlling the end effects (Eisenlohr & Eckelmann, 1988). Williamson presented in detail the clear evidence of the existence of a single Strouhal-Reynolds number relationship at lower Reynolds number by accounting for the obliqueness of the vortex shedding. The phenomenon of oblique shedding is due to end effects and is observed for large cylinder spans even of hundred of diameters in length. Number of authors have reported the Strouhal number discontinuity due to the oblique mode but they were unable to provide a consensus on the critical Reynolds number. Williamson found a critical Reynolds number 64 ± 1 for three cylinders of different diameters. When the oblique and parallel vortex sheddings are out of phase then cells of different frequency are observed. When two neighboring cells shed vortices out of phase, 'vortex dislocation' is observed. Progress in manipulation of end effects allowed the experimentalists to force parallel vortex shedding up to about $Re = 180$. The new striking features of the $St - Re$ relationship were then the two discontinuities, appearing around $Re = 180$ and $Re = 250$, that were insensible to end effects. They have been recognized, as early as in Williamson (1988*b*), to be related to the onset of three-dimensional structures in the wake. In the cited paper, he suggested two stages of transition associated to two different scales of three-dimensional structures in the cylinder wake. The first discontinuity (shifting the Strouhal number to lower values) is of hysteretic nature (two states are found to co-exist as low as at $Re = 172.8$, see fig. 1.7) and is related to the onset of spanwise structures called the 'A-mode' shown in the fig 1.8 . At higher Reynolds numbers finer spanwise structures (B-mode) set in (see fig. 1.9) and shift the Strouhal number upward, back to the previous trend, as can be seen in the fig 1.6. The second discontinuity spreads from $Re = 230 - 260$. A gradual increase of energy between the modes A and B takes place with the increase of the Reynolds number. The second discontinuity does not present a hysteresis, instead, both modes coexist.

The numerical and theoretical, albeit partial explanation of the onset of three dimensionality came several years later. The linear analysis was mostly based on the investigation of Floquet modes. The earliest work of Noack *et al.* (1993) predicted approximately the right critical Reynolds number but failed to provide the correct spanwise wavelength of the 3D structures. They made three-dimensional Floquet stability analysis of periodic flow in the wake of a circular cylinder in order to investigate the onset of three-dimensionality in the wake. Noack *et al.* (1993) found that the periodic flow is unstable to a three-dimensional near wake disturbance at $Re = 170$ with a spanwise wavelength $1.8D$ where D is the diameter of the cylinder. Experimentally, they found a spanwise wavelength $1.7D$ at $Re = 200$ which is slightly less than the wavelength at $Re = 170$ found theoretically. These results proved, however, to be inaccurate.

Accurate results were provided by Henderson & Barkley (1996) and Barkley & Henderson (1996). Their Floquet linear analysis allowed them to set the threshold of the loss of stability of the two-dimensional wake to $Re = 188.5$ and to find the spanwise wavelength of the so arising A-mode to be almost exactly equal to 4 cylinder diameters (d). Though the latter cited paper is more detailed and provides also the linear investigation of the B-mode, the former one is of particular interest for its mention of non-linear effects and a numerical evidence of the subcritical nature of the bifurcation yielding the A-mode. In the latter cited

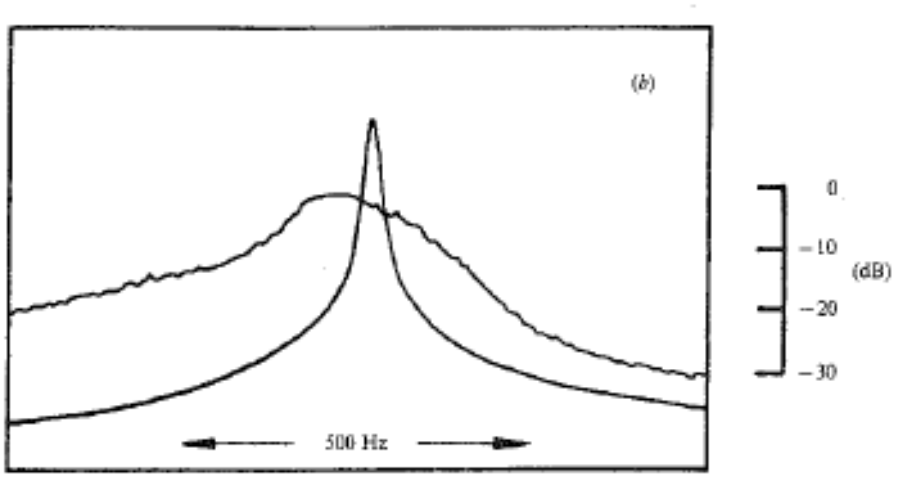

Figure 1.7: Near wake velocity spectra at $Re = 172.8$ showing corresponding to a 2D mode (sharp peak) and a 3D (A) mode reported by Williamson (1988*b*).

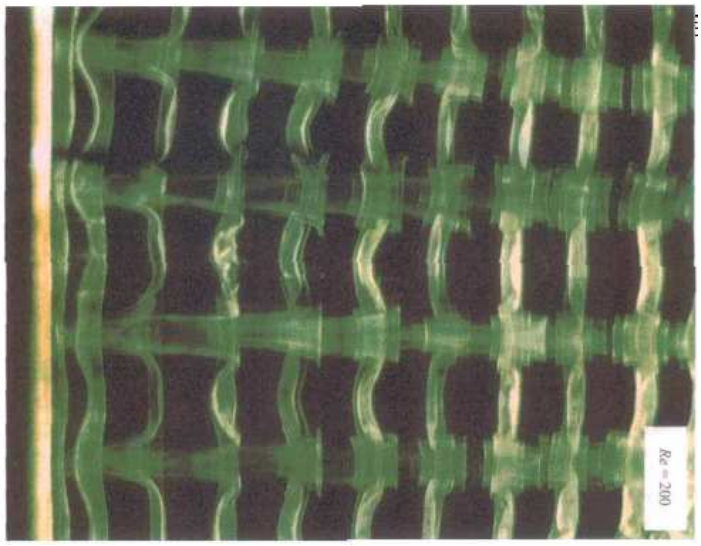

Figure 1.8: Mode A at $Re = 200$, the spanwise wavelength is $4.01d$ (Williamson, 1988*b*).

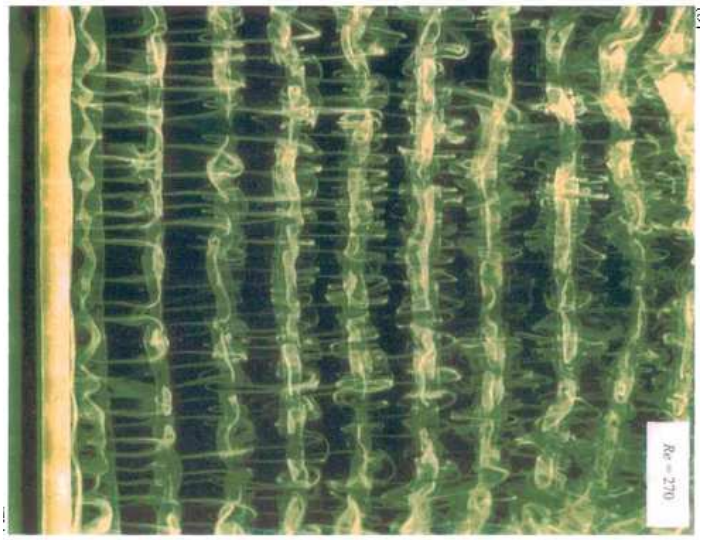

Figure 1.9: Mode B at $Re = 270$, spanwise wavelength $1d$ (Williamson, 1988b).

paper, the Floquet stability analysis of the periodic wake of a circular cylinder was carried out numerically for a range of Reynolds number $140 - 300$. The Floquet multiplier $\mu = exp(\sigma T)$ represents the amplification over one vortex shedding period T. The Floquet multiplier is independent of Reynolds number at the wavenumber $\beta = 0$ and is always equal to one (which corresponds to the 2D limit cycle). Away from $\beta = 0$, i.e. for three-dimensional perturbations, the multiplier depends on the Reynolds number. With the increase of Reynolds number the unstable modes shift to higher wave numbers. At $Re = 188.5$ and $\beta = 1.585$, which corresponds to spanwise wavelength of $3.96d$, the value of the Floquet multiplier was found close to one (more accurately, at $\beta = 1.585$ the multiplier becomes 0.9972) giving the critical values of the onset of three-dimensionality. The authors found two modes of instabilities known as mode A and mode B. The $2D$ flow undergoes a next bifurcation at $Re = 259 \pm 2$ with a spanwise wavelength $(0.822 \pm 0.007)d$. This wavelength corresponds to the mode B.

The linear Floquet analysis was applied with success to the investigation of the onset of three-dimensionality also in several other closely related configurations such as that of straight square cylinder (see Blackburn & Lopez, 2003) or a torus with varying aspect ratio (see Sheard *et al.*, 2003). The main feature of these configurations consists in presenting a third type of three-dimensional unstable mode (C-mode), which has been shown to be subharmonic in the case of the torus and quasi-periodic for a square cylinder and follows as a third bifurcation of the two-dimensional flow. The quasi-periodic mode has also been shown to be unstable for a circular cylinder (Blackburn *et al.*, 2005) starting from $Re = 377$ but it has never been observed in a fully non-linear simulation of the straight circular cylinder wake. In the first mentioned paper (see Blackburn & Lopez, 2003), the Floquet stability analysis was carried out for square and circular cylinders. It showed that a quasi-periodic

Spheres to circular cylinders

Ar range	Asymmetric transition mode		
	Primary transition	Secondary transition	Tertiary transition
$0 \leqslant Ar < 1.6$	Regular mode I $m = 1$ symmetry	Hopf mode I $m = 1$ symmetry	
$1.6 \leqslant Ar \leqslant 1.7$	Hopf mode II $m = 1$ symmetry		
$1.7 < Ar \lesssim 3.9$	Regular mode III $4.7d < \lambda_d < 7.9d$	Hopf mode III $4.7d < \lambda_d < 7.9d$	
$3.9 \lesssim Ar \lesssim 8$	Mode C $\lambda_d \approx 1.7d$	Mode A $\lambda_d \approx 4.0d$	Mode B $\lambda_d \approx 0.8d$
$8 \lesssim Ar \lesssim 13$	Mode A $\lambda_d \approx 4.0d$	Mode C $\lambda_d \approx 1.7d$	Mode B $\lambda_d \approx 0.8d$
$13 \lesssim Ar < \infty$	Mode A $\lambda_d \approx 4.0d$	Mode B $\lambda_d \approx 0.8d$	Mode C $\lambda_d \approx 1.7d$

TABLE Summary of the asymmetric transition modes for bluff ring wakes.

Figure 1.10: Table 4 from Sheard *et al.* (2003).

mode exists in both cases (i.e. a complex conjugate pair of Floquet multipliers exists) and the unstable modes behave as a traveling or standing wave. Blackburn *et al.* (2005) applied the Floquet stability analysis by using a half-period-flip map. Sheard *et al.* (2003) studied numerically the stability and flow dynamics in the wake of a bluff body torus. For large aspect ratio Ar the torus becomes a straight circular cylinder and it becomes a sphere at aspect ratio zero (the aspect ratio is a ratio of torus diameter to the diameter of the cross section of the ring). It is reported that for aspect ratio $Ar \geq 20$, the spanwise wavelength of mode A instability of rings is within 1.1% of that of the straight circular cylinder. It means that the linear analysis yields critical Reynolds numbers of modes A, B and C independent of the aspect ratio starting practically from $Ar > 20$. The spanwise wavelength of mode A instability increases to $4.5d$ for an aspect ratio $Ar = 5$ which is 14.5% greater than in the case of the straight circular cylinder. At $Ar = 5$ an intermediate mode C is observed whose spanwise wavelength lies between the spanwise wavelengths of mode A and mode B. The spanwise wavelength of mode C is $1.7d$ which is 17% smaller than quoted by Zhang *et al.* (1995). Similarly for a shorter wavelength mode B instability, the critical Reynolds number 301 is predicted for rings of the same aspect ratio $Ar = 5$. For rings with increasing aspect ratio $Ar \geq 20$, the critical Reynolds number is 258 which is 1.1% more than the critical value reported for a straight cylinder. Asymmetric transition modes for bluff rings of variable aspect ratio are summarized in figure 1.10. It is to be noted that the 'secondary' and 'tertiary' transitions correspond to perturbations of the axisymmetric flow and do not account for non-linear effects due to the development of the primary (and secondary) instabilities.

Fully non-linear numerical investigations are relatively limited in number although it is clear that two main features of the onset of three-dimensionality cannot be fully described within a linear framework. In experiments, the onset of the B-mode does not occur from a 2D wake but in a state in which the A-mode is already fully developed. The hysteresis

observed at the onset of the A-mode is by itself a strongly non-linear phenomenon and its analysis lies outside the scope of the linear theory. These problems combine with that of the description of the large (theoretically infinite) spanwise scale. The instability in the wake of a circular cylinder is explored by Henderson & Barkley (1996) in a numerical simulation with spanwise period of $4d$. The latter was determined by Floquet analysis by performing first a $2D$ DNS for $Re = 190-300$.The wake period is found from $2D$ simulations and periodic flows are used in Floquet stability analysis. The critical Reynolds number for the 3D instability of the 2D wake flow is determined from the linear stability calculations along with the linearly preferred spanwise wavelength. This spanwise wavelength is then used to determine spanwise periodicity of a non-linear 3D simulation. This is equivalent to assuming that no larger wavelength can arise. The $3D$ DNS are performed near the critical Reynolds number and it is found that the $3D$ amplitude A of $3D$ simulations departs from the exponential growth. Its growth is faster than exponential, i.e. the estimated Landau constant is positive, showing that the secondary instability is subcritical (see fig 1.11). A bistability between a 2D and a 3D flow is observed at $Re = 185$ (below the critical Reynolds number).

The resulting subcritical nature of the secondary instability is qualitatively in agreement with experimental results. The experimentally observed instability interval is, however, substantially larger. A closer look at the 'first discontinuity' of the $St - Re$ curve in Williamson (1988a) and Williamson (1988b) reveals bi-stable states between $Re = 170$ and $Re = 180$. The lowest Reynolds number at which two Strouhal frequencies are reported is 172.8. The linear analysis of Barkley & Henderson (1996) set the linear instability threshold for the A-mode at $Re = 188.5$ and provided a preferred wavelength of $3.96d$. These values have been widely accepted and confirmed by subsequent work. Combined, the experimental observations and linear analysis imply a large hysteresis interval reaching from $Re = 188.5$ down at least to $Re = 172.8$. In Henderson & Barkley (1996) a non-linear simulation with spanwise periodicity corresponding to the preferred linear wavelength confirmed the sub-critical nature of the bifurcation without, however, reproducing as large a hysteresis interval as observed in experiments conducted by Williamson (1988b). Most papers providing non-linear three-dimensional simulations are limited by a very restricted spanwise periodicity: $4d$ in Henderson & Barkley (1996) and Thompson *et al.* (2001), $2.25d$ and $3.72d$ in Persillon & Braza (1998). This strongly limits the captured dynamics. In spite of that, it is important to note that all these simulations predict the drop in Strouhal number after the onset of the A-mode.

The only paper going beyond the scope of these limitations is that by Henderson (1997). This paper shows that allowing for a large spanwise periodic scale (up to $13d$) makes it possible to reproduce large scale disturbances characteristic of experimental observations. The latter are of great importance because they have been associated in Williamson (1996b) to the dispersion of experimental observations at the threshold of three-dimensionality and have been related to end-effects of experimental cylinders. Henderson (1997) shows that large scale structures are inherent to the cylinder dynamics even in the absence of end effects. The numerical simulations of Henderson (1997) provide results for variably forced spanwise periodicity. At $Re = 190$ the spanwise period is limited to roughly $4d$ and the simulation reproduces the already mentioned results of Henderson & Barkley (1996) confirming the subcritical nature of the bifurcation giving rise to the A-mode. If the spanwise period is

limited to that of the B-mode, the A-mode is inhibited and the linear results pertaining to the B-mode are recovered. If a significantly larger spanwise periodicity than $4d$ is allowed for a strongly chaotic flow with many energetically strong subharmonic scales is obtained.

As already stated, the onset of three-dimensionality is characterized by two modes: A and B and the first one has been associated to a subcritical bifurcation. Similarly as for other wake configurations, the basic question is whether the B-mode arises via a well-defined instability and, if so, what the nature of this instability is. E.g., in the case of a sphere wake, the scenario is, at present, very well established (see Natarajan & Acrivos (1993), Johnson & Patel (1999), Ormières & Provansal (1999), Tomboulides & Orszag (2000) and Ghidersa & Dušek (2000)). The two earliest stages of transition correspond to a steady non-axisymmetric and to an unsteady periodic flow. Both changes have been clearly related to well defined supercritical bifurcations with widely accepted thresholds. The scenario in the cylinder wake is far less clearly established excepting the primary Hopf bifurcation. There are two reasons for that: i) the configuration is infinite in the spanwise direction and ii) the phenomena at the onset of three-dimensionality are very strongly non-linear. The bifurcation at the onset of the A-mode has been identified as subcritical. In Barkley & Henderson (1996) the threshold of the B-mode instability of the two-dimensional flow is found at $Re = 259$ with a preferred spanwise wavelength of $0.82d$. Qualitatively, the found values correspond to experimental observations but do not resist a quantitative validation. Indeed, the B-mode is already observed in the studies of Williamson (1996*b*) and Thompson *et al.* (1996) at $Re = 230$. This is not really surprising. A similar, albeit less pronounced phenomenon, exists in the sphere wake. The linear analysis of Natarajan & Acrivos (1993) predicted a secondary instability threshold at $Re = 277.5$ whereas Ormières & Provansal (1999) in their experiments and Ghidersa & Dušek (2000) in their fully non-linear simulations set the threshold rather at $Re = 274$. This is easily explained by the fact that the base-flow of Natarajan and Acrivos is not that from which the secondary instability actually develops. The same certainly holds for the B-mode (see Barkley *et al.*, 2000).

Unlike for the secondary instability of the sphere wake, no unambiguous evidence of a tertiary bifurcation giving rise the mode B has ever been provided. Williamson (1996*b*) reports 'intermittent periods' with 'predominantly small scale instability structures across the span' between $Re = 230$ and 250. Thompson *et al.* (1996) state 'a gradual redistribution of energy between the modes'. The lowest reported Reynolds number values at which the mode B has been observed in the cylinder wake are all of experimental origin. No numerical simulations evidence the presence of the mode lower than at $Re = 250$. Thompson *et al.* (1996) report the presence of the mode B in a simulation with a spanwise period 2π at $Re = 250$. They note a chaotic behavior of the numerical solution at this Reynolds number. Henderson (1997) investigates the mode B at $Re = 265$ but in a simulation with a small spanwise period of $0.82d$ chosen to be equal to the linear preferred spanwise wavelength of the mode. The same paper shows, however, that the spanwise periodicity of the simulation has a tremendous impact on the dynamics of the solution. In particular, the mode A is not at all obtained with this small spanwise period, which makes this sort of simulation far from realistic. If, on the other hand, a sufficiently large spanwise periodicity is allowed for, Henderson (1997) shows (again at $Re = 265$) that very rich chaotic dynamics resembling closely experimental observation arise.

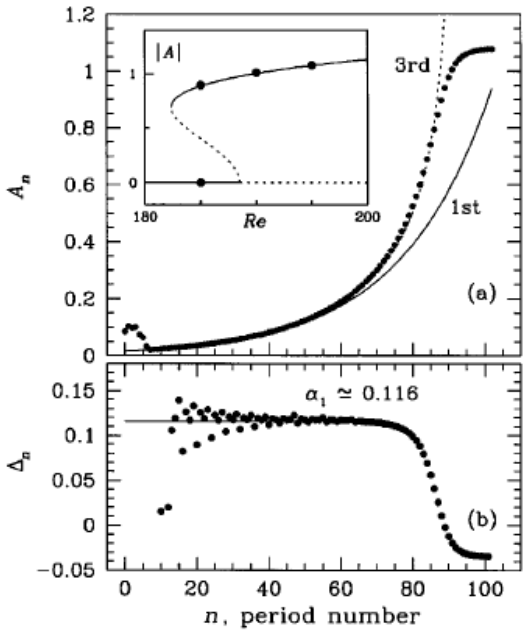

Figure 1.11: Subcritical nature of secondary instability as illustrated by Henderson & Barkley (1996). Upper figure: supra-exponential growth and the bistability at $Re = 185$ (inset). Lower figure: determination of the Landau coefficient.

Actually both modes can be expected to interact via non-linear couplings. A weakly non-linear (5-th order) theoretical model of this coupling can explain why the B-mode is observed experimentally below its linear threshold (see Barkley *et al.*, 2000). However, this model predicts also a specific bifurcation giving rise to the B mode although its threshold is shifted to lower Reynolds numbers due to the non-linear coupling with the mode A.

Moreover, for a large spanwise period, a spatio-temporal chaos is evidenced at $Re = 260$. The simulations show that all large scale spanwise Fourier modes become equally important. In Henderson (1997) it is argued that this is to be explained by the fact that, at $Re = 260$, the interval of unstable wavelengths is so wide that the unstable Fourier modes can combine via non-linear couplings to yield virtually unlimited spanwise length scales. This argument, however accurate it may be at $Re = 260$, prevents Henderson (1997) from focussing on the very threshold of the 3D instability and from investigating its subcritical nature at Reynolds numbers below the linear critical value of 188.5. The lesson to be drawn from Henderson's paper is that the spanwise periodicity has a significant impact on the simulated flow dynamics and that a sufficient spanwise period is needed to get realistic results. It can, namely, be expected that, provided sufficiently large spanwise scales are accounted for, the hysteresis interval reported in experiments can be confirmed by numerical simulations. These points are investigated in chapter 3 of the thesis.

The next main part of the thesis (chapter 4) consists in investigating the specificities of the airfoil as compared to the configuration of the circular cylinder. The knowledge of these specificities might help in designing efficient simulations at higher Reynolds numbers than those considered in chapter 4.

.

Chapter 2

Mathematical formulation and numerical method

This chapter deals with the mathematical formulation of the problem and the numerical method used to solve it. We are interested in the flow past an infinite circular cylinder and past an airfoil NACA 0012. The common feature of both geometries is their infinite dimension along one direction. We take advantage of a numerical method designed to simulate flows in cylindrical domains to represent infinite straight bodies as tori of very large aspect ratio. It is easily shown that the obtained formulation is equivalent to a spectral spanwise (span meaning the infinite direction) discretization common to many publications dealing with the same topic (see e.g. Karniadakis & Triantafyllou, 1992).

2.1 Mathematical formulation in cylindrical coordinates and the available code at the start of the thesis

2.1.1 Flow equations in cylindrical coordinates

The numerical algorithm used in this thesis for solving the Navier-Stokes equations in cylindrical geometries was originally developed by Ghidersa & Dušek (2000) for simulating the flow past a fixed solid sphere (see Fig. 2.1).

The governing equations are time dependent incompressible Navier Stokes equations:

$$\nabla.\mathbf{v} = 0, \tag{2.1}$$

$$\frac{\partial \mathbf{v}}{\partial t} + (\mathbf{v}\cdot\nabla)\mathbf{v} = -\frac{1}{\rho}\nabla p + \nu\nabla^2\mathbf{v}. \tag{2.2}$$

where $\mathbf{v} = (v_x, v_y, v_z)$ is the velocity field represented in Cartesian coordinates, p represents the pressure field, ν the kinematic viscosity and ρ the fluid density. In the present case, ν and ρ are assumed to be constant and uniform in space.

The flow equations are non-dimensionalized with respect to the free stream velocity U_∞ (assumed to be uniform, constant and oriented along the z-axis) and the only physical length

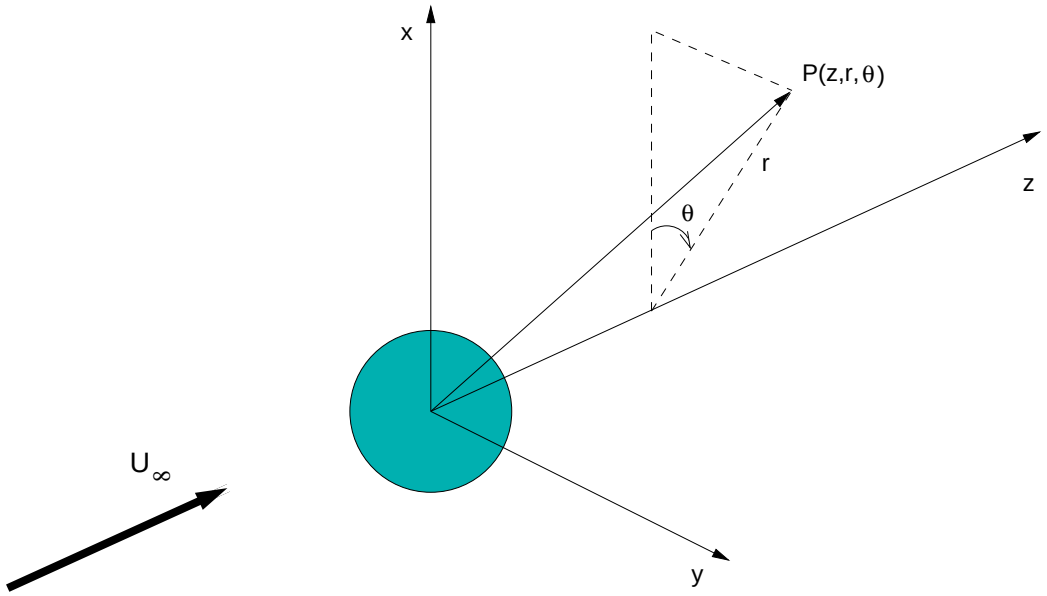

Figure 2.1: Geometrical configuration of the numerical domain in the case of a flow past a solid sphere. The geometry reflects the configuration for which the code was originally developed, not that of the present thesis. The latter is discussed in section 2.2.

scale present in the formulation, i.e. the sphere diameter d. In the non-dimensional form the above equations are written as:

$$\nabla.\mathbf{v} = 0, \tag{2.3}$$

$$\frac{\partial \mathbf{v}}{\partial t} + (\mathbf{v}\cdot\nabla)\mathbf{v} = -\nabla p + \frac{1}{Re}\nabla^2\mathbf{v}. \tag{2.4}$$

where $Re = \frac{U_\infty d}{\nu}$ is the Reynolds number. The unsteady incompressible Navier-Stokes equation in non-dimensionalized form in cylindrical coordinates z, r and θ can be written as

$$\frac{\partial u}{\partial z}+\frac{1}{r}\frac{\partial}{\partial r}(rv)+\frac{1}{r}\frac{\partial w}{\partial \theta}=0, \tag{2.5}$$

$$\frac{\partial u}{\partial t}+u\frac{\partial u}{\partial z}+v\frac{\partial u}{\partial r}+\frac{w}{r}\frac{\partial u}{\partial \theta}=-\frac{\partial p}{\partial z}+\nu\{\frac{\partial^2 u}{\partial z^2}+\frac{1}{r}\frac{\partial}{\partial r}\left(r\frac{\partial u}{\partial r}\right)+\frac{1}{r^2}\frac{\partial^2 u}{\partial \theta^2}\}. \tag{2.6}$$

$$\frac{\partial v}{\partial t}+u\frac{\partial v}{\partial z}+v\frac{\partial v}{\partial r}+\frac{w}{r}\frac{\partial v}{\partial \theta}-\frac{w^2}{r}=-\frac{\partial p}{\partial r}+\nu\{\frac{\partial^2 v}{\partial z^2}+\frac{1}{r}\frac{\partial}{\partial r}\left(r\frac{\partial v}{\partial r}\right)$$
$$+\frac{1}{r^2}\frac{\partial^2 v}{\partial \theta^2}-\frac{v}{r^2}-\frac{2}{r^2}\frac{\partial w}{\partial \theta}\}, \tag{2.7}$$

$$\frac{\partial w}{\partial t}+u\frac{\partial w}{\partial z}+v\frac{\partial w}{\partial r}+\frac{w}{r}\frac{\partial w}{\partial \theta}+\frac{wv}{r}=-\frac{1}{r}\frac{\partial p}{\partial \theta}+\nu\{\frac{\partial^2 u}{\partial z^2}+\frac{1}{r}\frac{\partial}{\partial r}\left(r\frac{\partial w}{\partial r}\right)$$
$$+\frac{1}{r^2}\frac{\partial^2 w}{\partial \theta^2}-\frac{w}{r^2}+\frac{2}{r^2}\frac{\partial v}{\partial \theta}\} \tag{2.8}$$

where u, v, w denote the axial (along the z-axis in Fig. 2.1), radial and azimuthal velocity components, respectively, and $\nu = 1/Re$ in the present case.

2.1.2 $U(1)$ coordinates

The cylindrical geometry implies a 2π periodicity along the azimuthal angle θ which can be taken advantage of for expanding all flow field variables into a Fourier series. Ghidersa & Dušek (2000) showed that, in the same time, the spectral azimuthal Fourier expansion is identical to that into non-linear modes arising at any axisymmetry breaking instability. This makes the method especially efficient for simulating transitional flows and, moreover, enables a simple implementation of a linear stability analysis. However, the cylindrical coordinates present the well-known problem of singularities along the axis both in their original version and after Fourier azimuthal expansion. This difficulty was overcome by S.A. Orszag (1983) by suggesting to replace the radial and azimuthal components by complex combinations. The approach was identified in Jenny (2003) and Jenny & Dušek (2004) as switching from an $O(2)$ to a $U(1)$ representation of the rotation group.

Let $\mathbf{A}$ be an arbitrary vector expressed in Cartesian coordinates and in ordinary cylindrical coordinates by (A_z, A_x, A_y) and (A_z, A_r, A_θ), respectively. If instead of the components A_x, A_y we introduce $A_\pm = A_x \pm iA_y$ a rotation of the frame around the z-axis by an angle α resulting, in Cartesian coordinates, in the transformation:

$$\begin{bmatrix} A_{x'} \\ A_{y'} \end{bmatrix} = \begin{bmatrix} \cos\alpha & \sin\alpha \\ -\sin\alpha & \cos\alpha \end{bmatrix} \begin{bmatrix} A_x \\ A_y \end{bmatrix} \tag{2.9}$$

reduces in $U(1)$ coordinates to

$$A'_\pm = A_\pm\, e^{\mp i\alpha}. \tag{2.10}$$

As a consequence, the transformation from Cartesian $A_\pm$ to cylindrical coordinates $\tilde{A}_\pm \equiv A_r \pm iA_\theta$ writes simply:

$$\tilde{A}_{\pm} = A_{\pm}\, e^{\mp i\theta}. \tag{2.11}$$

2.1.3 Azimuthal Fourier expansion

The simplicity of the transformation between Cartesian and cylindrical coordinates is not the main purpose of the introduction $U(1)$-coordinates. The most important is that the latter obey equations with removable singularities when expanded into a Fourier azimuthal expansion:

$$p(z,r,\theta,t) = \sum_{m=-\infty}^{+\infty} p_m(z,r,t)\, e^{-im\theta} \tag{2.12}$$

$$\mathbf{v}(z,r,\theta,t) = \sum_{m=-\infty}^{+\infty} \mathbf{v}_m(z,r,t)\, e^{-im\theta}. \tag{2.13}$$

The vector field 2.13 is understood in $U(1)$ coordinates as having just two components: the real one u and the complex one $v_+ = v + iw$ because $v_- = \overline{v_+}$ contains the same information. The Fourier coefficients of the real fields p and u satisfy the conditions

$$p_{-m} = \overline{p_m}, \quad u_{-m} = \overline{u_m} \tag{2.14}$$

showing that Fourier modes with non-negative indices m provide the full information. In contrast, the unexpanded variable v_+ being itself complex, the negative modes are independent of the positive ones and must thus be computed. For practical reasons, the implementation of the method works rather with $v_{-,m}$ with positive values of m which is equivalent to providing $v_{+,m}$ with negative values of m due to the condition:

$$v_{\pm,-m} = \overline{v_{\mp,m}}. \tag{2.15}$$

The so defined Fourier modes have been shown by S.A. Orszag (1983) to have the following behavior at the flow axis for $m \geq 0$:

$$v_{z,m}\,|_{r=0} \sim r^m, \quad p_m\,|_{r=0} \sim r^m \tag{2.16}$$

$$v_{-,m}\,|_{r=0} \sim r^{m+1} \tag{2.17}$$

$$v_{+,m}\,|_{r=0} \sim r^{|m-1|}. \tag{2.18}$$

The expanded equations 2.5 through 2.8 are equivalent to the following system:

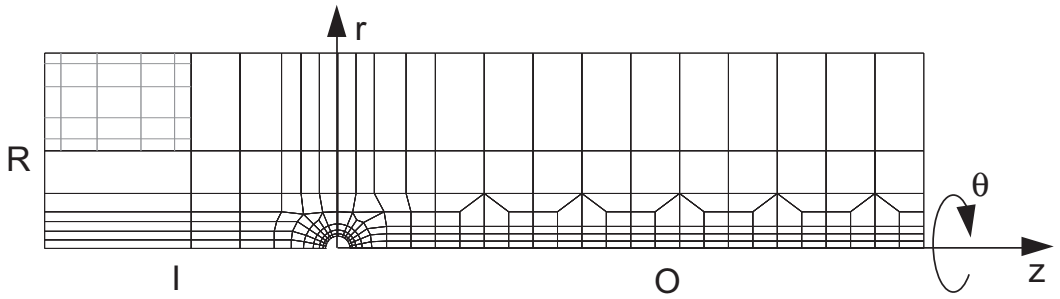

Figure 2.2: Break up of the domain around a sphere into spectral elements. The spectral element mesh contains 230 spectral elements. The internal collocation points are represented for the upper left element (in the case of 6 by 6 internal collocation points).

$$\frac{\partial v_{z,m}}{\partial t} + \hat{\mathcal{F}}_{m,z} = -\frac{\partial p_m}{\partial z} + \nu \nabla^2_{m^2}\, v_{z,m}; \tag{2.19}$$

$$\frac{\partial v_{-,m}}{\partial t} + \hat{\mathcal{F}}_{m,-} = -\left(\frac{\partial p_m}{\partial r} - m\frac{p_m}{r}\right) + \nu \nabla^2_{(m+1)^2}\, v_{-,m} \tag{2.20}$$

$$\frac{\partial v_{+,m}}{\partial t} + \hat{\mathcal{F}}_{m,+} = -\left(\frac{\partial p_m}{\partial r} + m\frac{p_m}{r}\right) + \nu \nabla^2_{(m-1)^2}\, v_{+,m} \tag{2.21}$$

$$\nabla^\dagger_m \cdot \mathbf{v}_m = 0 \tag{2.22}$$

where $\nabla^\dagger_m$ is minus the divergence operator in the m-subspace:

$$-\nabla^\dagger_m = \left(\frac{\partial}{\partial z}, \frac{1}{r}\frac{\partial}{\partial r}r + \frac{m}{r}, \frac{1}{r}\frac{\partial}{\partial r}r - \frac{m}{r}\right) \tag{2.23}$$

adjoint of the gradient operator ∇_m acting on the pressure mode p_m as written in Eqs. (2.19,2.20,2.21) and where

$$\nabla^2_{m^2} = -\nabla^\dagger_m \cdot \nabla_m. \tag{2.24}$$

The scalar product $\cdot$ in Eqs. (2.22,2.24) is to be understood as

$$\mathbf{A} \cdot \mathbf{B} = A_z B_z + \frac{1}{2}(A_+ B_- + A_- B_+). \tag{2.25}$$

$\hat{\mathcal{F}}_{m,z}$ and $\hat{\mathcal{F}}_{m,\pm}$ stand for the Fourier modes of the advective terms. Their computation was originally implemented fully in the Fourier space as described in the appendix of the paper by Ghidersa & Dušek (2000). In what follows a new version switching between the Fourier and the physical space will be described.

2.1.4 Spectral element discretization of the axial-radial plane

The axial-radial plane of the domain is discretized by two-dimensional spectral elements (see Patera, 1984). An example of the breakup of the axial-radial plane of the computational domain around a sphere is presented in Fig. 2.2. The spectral elements must be topologically quadrangles (albeit arbitrarily curved). The are mapped to $[-1,1]^2$ squares and functions defined on such a square are discretized, for elements not touching the symmetry axis, in both direction by the same Gauss-Lobatto-Legendre interpolation formula. Elements one side of which coincides with the symmetry axis account also for the presence of the vanishing weight r in the surface element $dS = rdrdz$ by using a Gauss-Lobatto-Jacobi interpolation in the direction perpendicular to the axis. The elements are conformal, i.e. the number of collocation points is the same in all of them and the collocation points at element interfaces are physically identical. At these points the values of discretized fields are forced to be equal. More details on the implementation of the spectral element method can be found in the thesis by Fischer (1989).

As can be seen in Fig. 2.2, the spectral element method provides a very good geometrical flexibility by making it possible to define elements of very different size. On the other hand, changing just the number of collocation points within each element allows the user to increase uniformly the discretization accuracy and the convergence of this type of mesh refinement can be shown to spectral.

2.1.5 Time discretization

The time discretization has been chosen so as to be as efficient as possible for relatively 'high' Reynolds flows, i.e. for $Re \geq 100$. In this case, the best choice appears to be the time splitting approximation.

The time splitting approximation consists in dividing the advancing from the time t_n to $t_{n+1} = t_n + \Delta t$ into three substeps. Write the decomposed equations (2.19) through (2.22) in a compact vectorial way:

$$\frac{\partial \mathbf{v}_m}{\partial t} + \hat{\mathcal{F}}_m \;=\; -\nabla_m p_m + \nu \Delta_m \, \mathbf{v}_m \tag{2.26}$$

$$\nabla_m^\dagger \cdot \mathbf{v}_m = 0. \tag{2.27}$$

where $m \geq 0$ stands for the azimuthal wave number, $\mathbf{v}_m = (u_m, v_{+,m}, v_{-,m})^T$, $\Delta_m \, \mathbf{v}_m$ represents the diffusion terms and $\hat{\mathcal{F}}_m$ the advective terms. The time-stepping can be expressed as:

$$\frac{\mathbf{v}_m^{(n+1)} - \mathbf{v}_m^{(n)}}{\Delta t} = -\hat{\mathcal{F}}_m^{(n)} - \nabla_m p_m^{(n+1)} + \nu \nabla^2 \mathbf{v}_m^{(n+1)}. \tag{2.28}$$

where, for simplicity, we assume the advective terms to be taken at the previous time step. Actually, the advective terms are extrapolated within a third order accuracy in Δt using the Adams-Bashforth method. The subdivision into three substeps introduces two intermediate velocity fields $\mathbf{v}^*$ and $\hat{\mathbf{v}}$:

$$\frac{\mathbf{v}_m^{(n+1)} - \mathbf{v}_m^{(n)}}{\Delta t} = \frac{\mathbf{v}_m^{(n+1)} - \hat{\mathbf{v}}}{\Delta t} + \frac{\hat{\mathbf{v}} - \mathbf{v}^*}{\Delta t} + \frac{\mathbf{v}^* - \mathbf{v}_m^{(n)}}{\Delta t}. \tag{2.29}$$

and each substeps accounts for one of the terms on the RHS of Eq. (2.28):

$$\frac{\mathbf{v}^* - \mathbf{v}^{(n)}}{\Delta t} = -\hat{\mathcal{F}}_m^{(n)} \tag{2.30}$$

$$\frac{\hat{\mathbf{v}} - \mathbf{v}^*}{\Delta t} = -\nabla_m p_m^{(n+1)} \tag{2.31}$$

$$\frac{\mathbf{v}_m^{(n+1)} - \hat{\mathbf{v}}}{\Delta t} = \nu \Delta_m \mathbf{v}^{(n+1)}. \tag{2.32}$$

The first substep is completely explicit and the third one amounts to solving a very well conditioned Helmholtz equation. Indeed, the explicit substep requires to respect the CFL criterion $\Delta t \leq C\Delta x_{min}/U_{max}$ where x_{min} is the smallest distance of two neighboring collocation points and U_{max} the maximum velocity (taken over all azimuthal modes and velocity components). It is clear that if a discretization is fine, albeit just locally, a very small time step results. As a consequence, along with the assumption that $\nu = 1/Re$ is small, the diagonal term $1/\Delta t$ largely dominates the discretized Helmholtz operator (2.32) and the equation (2.32) is very easily solved by conjugate gradients.

This is far from being the case when solving for the second intermediate velocity $\hat{\mathbf{v}}$ and the pressure p_m. The pressure equation results from the requirement that $\nabla_m^\dagger \cdot \hat{\mathbf{v}} = 0$. It is clear that the final velocity field $\mathbf{v}_m^{(n+1)}$ is no longer exactly divergence-free but due to the above assumptions (short time step, high Reynolds number) the error is negligible. The system to be solved is:

$$\frac{\hat{\mathbf{v}}}{\Delta t} + \nabla_m p_m^{(n+1)} = \frac{\mathbf{v}^*}{\Delta t} \tag{2.33}$$

$$\nabla_m^\dagger \cdot \hat{\mathbf{v}} = 0 \tag{2.34}$$

The discretized form of the equations defining $\hat{p}$, the discretized pressure mode p_m, and $\hat{w}$ the discretized mode of the velocity field can be cast in more detail in the following way (we omit the index m though the equation applies to a given m-th subspace):

$$\frac{1}{\Delta t} I_w D M \hat{w} + I_w D M G \hat{p} = I_w D M \hat{f} \tag{2.35}$$

$$I_p D G^T M \hat{w} = 0 \tag{2.36}$$

where I_w, I_p are masks respecting Dirichlet boundary conditions for the velocity and pressure, respectively and D is the matrix enforcing the identity of values at physically identical points. The operation doing that is called 'direct stiffness sum'. Assume a functional to be discretized as a quadratic form $x^T A x$, where x is an n component array and A an $n \times n$ symmetric, positive-definite matrix. If the components of x are all independent, the gradient

to be applied to obtained equations from a variational formulation yields $\nabla(x^T Ax) = 2Ax$. However, if, say $x_k = x_\ell$, then $\partial x^T Ax/\partial x_k = \partial x^T Ax/\partial x_\ell = \partial x^T Ax/\partial x_k + \partial x^T Ax/\partial x_\ell$. In this case, $\nabla(x^T Ax) = 2DAx$, where

$$D = \begin{pmatrix} 1 & & & & & & \\ & \ddots & & & & & \\ & & 1 & \dots & 1 & & \\ & & \vdots & \dots & \vdots & & \\ & & 1 & \dots & 1 & & \\ & & & & & \ddots & \\ & & & & & & 1 \end{pmatrix} \tag{2.37}$$

the extra ones being situated at the intersection of k-th and ℓ-th line and column. M is the (in a collocation discretization always) diagonal mass matrix and G is the matrix discretizing the gradient operator ∇_m. The matrix G remains real even for the complex azimuthal modes, as a result simply its transposed G^T appears in Eq. (2.34). Finally $\hat{f}$ stands for the discretized RHS of Eq. (2.33). Upon elimination of $\hat{w}$ using Eq. (2.34) we arrive at an equation making it possible to compute $\hat{p}$:

$$I_p D G^T M \tilde{M}^{-1} I_w D M G \hat{p} = I_p D G^T M \tilde{M}^{-1} I_w D M \hat{f} \tag{2.38}$$

where $\tilde{M}$ is the diagonal matrix obtained by applying the direct stiffness sum to the array of diagonal elements of M. It is clear, that unlike in the original implementation of the method at MIT (see Patera, 1984; Fischer, 1989), the pressure matrix in Eq. (2.38) is not $G^T MG$ as would be obtained if the velocity $\hat{\mathbf{v}}$ were eliminated directly in the continuous equations (2.33), (2.34). Indeed, it appeared that in the original version of the code, it was impossible to eliminate significant divergence values at element interfaces. Solving equation (2.38) brought an improvement of the spatial discretization accuracy. The modification was implemented during the PhD thesis of Kotouč (2008).

2.1.6 Direct pressure solver

The matrix of the pressure equation remains, for all its complexity, symmetric and positive-definite and Eq. (2.38) can be solved by conjugate gradients as is commonly done in most spectral element codes. However, this matrix of the pressure equation, even in its less correct but simplified form $G^T MG$ is badly conditioned. As a result, it is quite common to spend more than 90% of CPU time for solving pressure. After implementation of the more accurate version (2.38), the conditioning of the matrix still worsened. A significant improvement of the numerical code was, however, achieved during the PhD thesis of Kotouč (2008) by implementing a direct solver of Eq. (2.38). Because the matrix operates only within a given azimuthal subspace, its size remains reasonable (typically $10^4 \times 10^4$ for a mesh of type represented in Fig. 2.2) and the sparsity of the matrix is still very good (less than 1% of non-zero elements). The pressure matrix on the LHS of Eq. (2.38) is generated as a sparse matrix and decomposed by LDL decomposition as a product LDL^T where L is a

lower triangular and D a diagonal matrix. A ready to use subroutine has been downloaded and implemented for this purpose. It provides still a very sparse triangular matrix that is inverted at very low costs. The solution of the pressure equation is carried out independently for each azimuthal mode m. As many LDL decompositions as the number of azimuthal modes are needed. The CPU time requirements are, actually, negligible because, for fixed geometry, the decomposition is executed just ones at the start of the computing run. The method puts higher requirements on available RAM, however, the increase of the size of used memory was no problem at the moment at which the direct method was implemented because of the arrival of the 64 bit technology and large and cheap memory chips. The costs of inversion of the decomposed matrix completely reversed the ratio of costs of inversion of velocity and pressure equations, the latter becoming negligible. With the previous 90% of computing costs spent for solving the pressure equation the resulting speed up was thus by a factor of 10.

2.2 Straight infinite geometries and code adaptation performed in this thesis

In the present thesis, we face the problem of simulating an infinite cylinder placed in a domain that is infinite in the direction of the cylinder generatrix. For wings, the direction is called span. The same terminology has been retained also in the case of the circular cylinder. The standard approach consists in simulating the spanwise infinite direction by imposing an *ad hoc* spanwise periodicity. Topologically, such a configuration is that of a torus, albeit with zero curvature.

For an infinite circular cylinder, Blackburn *et al.* (2005) noted that, the transition in the wake of a torus 'asymptotes' in the limit of large aspect ratio $Ar = D/d$, D and d being the large and small torus diameters, both qualitatively and quantitatively to that of an infinite straight cylinder. This consideration attracted attention to rings as an experimental configuration without end effects. As we already mentioned in the intoduction to this thesis, linear analysis yields critical Reynolds numbers of modes A, B and C independent of the aspect ratio starting practically from $Ar > 20$. These results suggested us the idea to use the code described in Sec. 2.1 for simulating tori of very large aspect ratio with the purpose of investigating wakes of physically straight cylinders. The code provides directly a possibility to simulate tori of any aspect ratio. The scheme of the configuration is represented in Fig. 2.3. For a torus of a very large aspect ratio the domain does not include the symmetry axis. Instead, only the flow in the domain obtained by revolution about the axis of a rectangle lying off the axis is simulated. For a circular cylinder, the discretization of this rectangle in the axial-radial plane could be obtained essentially by completing the mesh represented in Fig. 2.2 by its mirror image with respect to the horizontal axis. An example of the axial-radial spectral element mesh used to simulate the flow past a circular cylinder is shown in Fig. 2.4

The azimuthal (spanwise) degrees of freedom are discretized, as previously, by Fourier expansion. Assuming that, physically, a relatively small spanwise period of the torus is relevant, it is possible to reduce the spanwise wavelength to some finite value

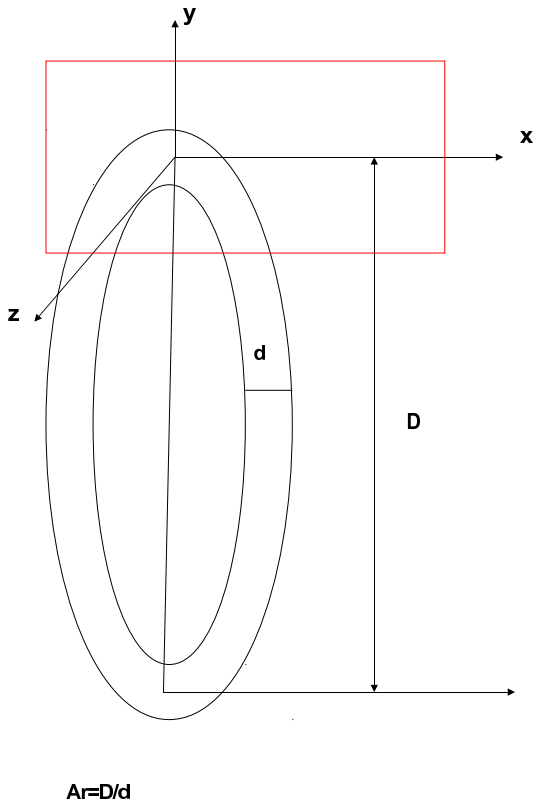

Figure 2.3: Principle of a simulation of a very large torus. The radial-axial plane of the actual computational domain is represented by the red rectangle.

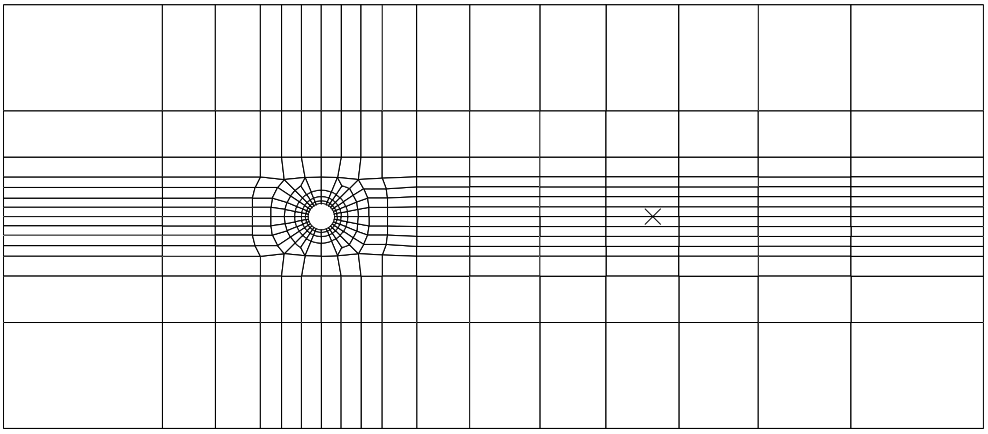

Figure 2.4: The spectral element decomposition of the radial-axial plane of the toroidal domain

$$\lambda = \pi D/M \tag{2.39}$$

where M is a relatively large number of periods around the axis. The standard Cartesian formulation corresponding to an exactly straight body is obtained by replacing the azimuthal Fourier expansion with M periods around the axis by setting $\theta = 2z/D$ (i.e. $M\theta = 2\pi z/\lambda$) and by letting $D \to \infty$ while keeping λ constant. Introducing, in addition to the so defined spanwise Cartesian component z, also the transverse component $y = r - D/2$ (where r is the distance to the axis of the torus) we obtain a traditional Cartesian coordinate discretization of an exactly straight cylinder with a spanwise Fourier decomposition (see e.g. Karniadakis & Triantafyllou, 1992; Henderson & Barkley, 1996). The streamwise component will be denoted x throughout the thesis (unlike it was the case for the mentioned simulation of the flow past a sphere where the flow axis was called z). The number M represents the fundamental mode of the azimuthal Fourier decomposition of a function having M periods of spanwise length (2.39) around the axis. For this purpose, the expansion (2.12,2.13) has been modified as follows:

$$p(z, r, \theta, t) = \sum_{m=-\infty}^{+\infty} p_m(z, r, t)\, e^{-imM\theta} \tag{2.40}$$

$$\mathbf{v}(z, r, \theta, t) = \sum_{m=-\infty}^{+\infty} \mathbf{v}_m(z, r, t)\, e^{-imM\theta}. \tag{2.41}$$

Fig. 2.4 represents a spectral element mesh of 338 elements. The boundary conditions are a Dirichlet condition with a unit streamwise velocity at the inflow boundary and a Neumann (no stress) condition at the outflow and lateral boundaries. The represented mesh extends 12 diameters upstream, 25 diameters downstream and 8 diameters sideways of the cylinder. These are roughly the same numerical parameters considered to obtain satisfactory accuracy in all available literature. The numerical convergence was tested with respect to the following parameters: the distance of domain boundaries, the size and distribution of spectral elements, the number of collocation points and the radius of the torus. As a criterion we chose the critical Reynolds number value of the transition to three-dimensionality obtained from the linear marginal stability curve described in chapter 3.

The tests of the effect of increasing aspect ratio can be seen in Table 2.1. The table presents amplification rates at the onset of the secondary instability, i.e. of the instability leading to three-dimensionality in the wake of tori of increasing aspect ratios. We settled to $Ar = 500$ although, as can be seen, for $Ar \geq 200$ the variation of the amplification rate and, consequently, of the critical Reynolds number is negligible. As will be seen in chapter 3, the reason to choose rather a higher aspect ratio consists in the possibility of finely varying the spanwise wavelength of the period of the domain.

The effect of the number of collocation points can be seen in Table 2.2. The table presents the critical Reynolds number and the preferred wavelength (see chapter 3 for more details) of the transition to three-dimensionality in the wake of a torus of aspect ratio 500, i.e., for all practical purposes, of a straight cylinder for 6 and 8 collocation points per spatial direction.

Ar	$Re = 189$	$Re = 190$	Re_{crit}
100	-1.46E-03	3.4E-04	189.81
200	-1.14E-03	6.7E-04	189.63
300	-1.09E-03	7.2E-04	189.60
400	-1.06E-03	8.1E-04	189.57
500	-1.05E-03	9.9E-04	189.51

Table 2.1: Linear amplification rates just below ($Re = 189$) and above ($Re = 190$) the threshold of the transition to three-dimensionality for increasing aspect ratio of the torus for the 338 element mesh in Fig. 2.4 and 6 collocation points per spatial direction of spectral elements.

	Re_{crit}	λ_{crit}
$N = 6$	189.5	3.93 d
$N = 8$	188.33	3.965 d
B. & H. 1996	188.5 $\pm$ 1	3.96 $\pm$ 0.02 d

Table 2.2: Results of linear analysis on the mesh with 6 and 8 collocation points. Our results have been obtained for a torus of $Ar = 500$. B. & H. 1996: Barkley & Henderson (1996).

The values reported by Barkley & Henderson (1996) are also given for comparison. For the mesh represented in Fig. 2.4 and 6 collocation points per spatial direction in each spectral element the critical Reynolds number is found to be 189.5, i.e. still within bounds set by Barkley & Henderson (1996). If all the outer elements are left out, the critical Reynolds number increases only by 0.9 (i.e. by about 0.5 %) if an additional layer is added a variation of Re by less than 0.1 is obtained. Eight collocation points par spatial direction provide a perfect agreement with published results: a critical Reynolds number of 188.3, a preferred spanwise wavelength of $3.965d$ and a Strouhal number $St = 0.196$ at $Re = 200$. It is seen that 6 collocation points yield already an acceptable accuracy. To liberate computing resources for simulations with many degrees of freedom in the spanwise direction we shall use the lower accuracy in the axial-radial plane.

The short-wave truncation, i.e. the number of terms in expansions (2.40,2.41) was tested by computing the saturated amplitude of the mode A at $Re \in [185, 190]$ with the linearly preferred spanwise period ($\lambda_A = 4d$). As will be seen in the following chapter, the bifurcation leading to three-dimensionality is subcritical and, in the interval $Re \in [185, 190]$, the amplitude remains almost independent of the Reynolds number. A decrease of less than 2% of the spanwise velocity oscillation amplitude was observed when increasing the highest harmonic taken into account from 4 to 6. The short scale truncation was optimized in order to allow for an as large as possible spanwise period. So far the largest considered period being that of Henderson (1997) (3 times the linear preferred wavelength of mode A, more exactly $13d$) we chose to consider a spanwise periodicity of as much as $10\pi d$, i.e. about 8 times the preferred wavelength of the mode A. This brought the number of terms of the real

spanwise decomposition to 32. It is clear that this number of Fourier modes can no longer be treated efficiently in the spectral space. A modification of the code allowing for switching between the spectral and the physical space when computing the advective terms had to be implemented.

2.2.1 New method of computation of advective terms

By adding Eq. (2.7) and $i \times$ Eq. (2.8) we obtain advective terms in the equation for the $U(1)$ component v_+ in the form:

$$\mathcal{F}_+ = u\frac{\partial v_+}{\partial z} + v\frac{\partial v_+}{\partial r} + \frac{w}{r}\left(\frac{\partial}{\partial \theta} + i\right) v_+. \tag{2.42}$$

where v and w are, respectively, the real and imaginary part of v_+. If computed fully in the spectral space, the computation of the term (2.42) involves convolutions (see Ghidersa & Dušek, 2000), which cease to be efficient as soon as the total number of azimuthal modes approaches 10. It is then more efficient to compute this term by applying first the differential operators in the (original) spectral space to the azimuthal modes $v_{+,m}$, by transforming the results, along with the component v_+ itself, to the physical space (by summing the Fourier expansions), by carrying out the multiplications in the physical space and by decomposing the result back into azimuthal modes $v_{+,m}$. The same method is, of course, also to be applied, to the advective terms in Eq. (2.6). The transformation to the physical space and back has been written alternatively as a 'naive' sum of the Fourier series and, for a number of modes m_{max} such that $2*(m_{max}+1)$ equals to a power of two, also using the fast Fourier transform (FFT). We used the original algorithm by Cooley & Tukey (1965) limited to powers of 2. The FFT operates on a circle and must be computed as complex. If we truncate the development (e.g. (2.12)) as:

$$p(z, r, \theta, t) = \sum_{m=-m_{max}}^{m_{max}} p_m(z, r, t)\, e^{-im\theta} \tag{2.43}$$

it involves $2 \times m_{max} + 1$ terms, whereas a classical FFT requires an odd number (actually $N = 2^n$) of points on a circle. We distribute the modes 0 through m_{max} along the upper half circle and the modes -1 through $-m_{max}$ along the lower half circle as shown in Fig. 2.5. The point opposite to the origin remains thus unused. This explains why $N = 2*(m_{max}+1)$. The loss of efficiency due to the presence of one dummy mode is negligible. For transforming real quantities, a complex FFT must still be used. This causes twice as high computing costs as if a real procedure were available. In our case, we, however, do not transform scalar quantities but long arrays of values. The loss of efficiency is avoided by introducing complex arrays of half the original length by combining their values pairwise as real and imaginary parts of a complex array that is transformed by FFT. As will be seen in chapter 3 we worked with FFTs on $N = 64$ modes, i.e. for $m_{max} = 31$. If the non-linear terms are computed in the spectral space or by the 'naive' summation, for such a number of terms of the expansion, the computing costs needed for their evaluation are higher that for the implicit part of the time stepping (i.e. for solving the velocity equations). Switching to FFT allowed us to render the costs of the explicit terms negligible again.

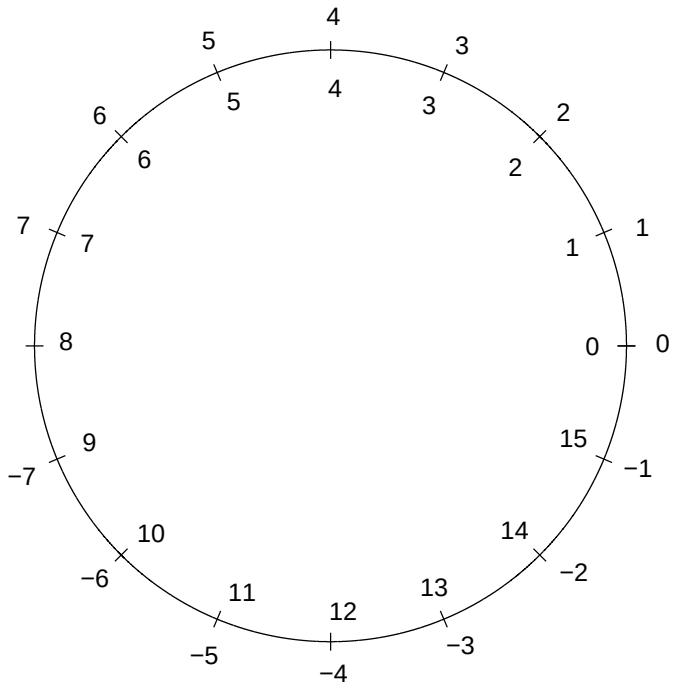

Figure 2.5: Distribution of azimuthal modes along a unit circle for the computation of the FFT

2.2.2 Code performance and limitations

The resulting code, written mainly in Fortran 90, is optimized for tackling parametric numerical investigation of flows in transition to turbulence. In such flows diffusion terms are relatively very small while the explicit (centered) treatment of non-linear terms requires diffusion for assuring numerical stability. This lead the choice of the time discretization which is globally only of first order accuracy due to the implicit treatment of the diffusive terms. The dominant advective terms are, however, accounted for with a third order accuracy (using an Adams-Bashforth method) and, moreover, the CFL stability criterion sets severe limitations to the time step because of a very fine spatial resolution. Typically, on the order of thousands of time steps are needed for solving a single vortex shedding period. As a result, numerical tests never provided evidence of insufficiently accurate time discretization.

In contrast, as mentioned throughout the presentation of the numerical method, a great attention has been paid to the quality of the spatial discretization, which is essential for yielding high quality results. The effort of obtaining a high quality spatial resolution can very rapidly result in prohibitive computing costs. This problem has been avoided by virtually eliminating the effect of costs of the pressure solver (usually a dominant stage of the computation of incompressible flows) and of the computation of advective terms. The resulting version of the code used in this thesis spends most of the time for solving velocity equations.

The applications of the code are limited to topologically cylindrical geometries, the code is inaccurate at very low Reynolds numbers and is unstable at too high Reynolds numbers. It has been run sofar on PC computers. At present the multi-core technology is used for running efficient parametric investigations requiring a large number of parallel runs (sometimes exceeding 1000). The code has not yet been parallelized although the Fourier expansion would provide a convenient framework for parallelization.

.

Chapter 3

Subcritical bifurcation at the onset of three-dimensionality in the cylinder wake

3.1 Introduction

The original intention of the present thesis was to focus essentially on the wake of an airfoil. The numerical results of flows past airfoils are, however, extremely dispersed as far as the cross-section and incidence is concerned and, moreover, relatively few concern direct simulations of fully incompressible flows. To validate the numerical method we turned to the, seemingly, well known and well investigated configuration of the infinite circular cylinder. The known, both experimental and numerical results, have been summed up in chapter 1. As can be concluded from Sec.1.2, in spite of more than 50 years of investigation effort (dated from the paper by Roshko (1954)), there still remains a discrepancy between the experimental observations and numerical and theoretical results as far as the predictions of the onset of three-dimensionality is concerned. As the onset of three-dimensional structures is of fundamental importance for designing an appropriate numerical simulation of a flow past an infinite body we considered it necessary to elucidate the reasons of these discrepancies before tackling the problem of flow past an airfoil. The present chapter is devoted to the presentation of results that fill the existing gap.

In what follows, we show that the results of linear investigations, such as that by Barkley & Henderson (1996) are reliable and of very high numerical quality. We used them to validate our numerical method and, not surprisingly, because our numerical method is almost identical, we very accurately reproduced the bibliographic data. In contrast, we show that the non-linear investigations performed in the past are incomplete and mostly suffer from the unfounded assumption that the spanwise periodicity of the fully three-dimensional flow remains that given by the linearly preferred wavelength. Actually, non-linear couplings trigger the onset of subharmonic scales. If the latter are correctly accounted for, the experimental observations can be reproduced by numerical simulations.

Ar	N=6
100	0.2015
200	0.2018
300	0.2018
400	0.2017
500	0.2017
∞ (2D)	0.2017

Table 3.1: Strouhal numbers of axisymmetric simulations of the flow past a torus of increasing aspect ratio and for an exactly 2D calculation obtained using the 338 element mesh in Fig. 2.4 with $N = 6$ at $Re = 190$.

3.2 Two-dimensional flow

The two-dimensional flow represents the base flow for the onset of three-dimensionality. Because the 2D flow past an infinite cylinder becomes unsteady due to a Hopf bifurcation at a Reynolds number as low as 46 (see e.g. Dušek *et al.*, 1994) the flow is unsteady at Reynolds numbers approaching 200 at which the onset to three-dimensionality sets in. As explained in Sec. 2.2, we simulate a straight circular cylinder as a torus of a very large aspect ratio. It has been argued in Table 2.1 that for aspect ratio $D/d = 500$ the linear results of the transition to three-dimensionality are no longer affected by the finite curvature of the torus. This will be further confirmed by the perfect agreement with bibliographic data obtained for exactly straight geometry. Moreover, the 2D flow is also expected to be obtained as a limit of the axisymmetric flow for very large aspect ratio of the torus. The principal physical characteristics of the 2D flow being the vortex shedding frequency measured in terms of the Strouhal number $St = fd/U_\infty$ we present the comparison of the Strouhal number obtained in a 2D computation with that of an axisymmetric one past a torus of increasing aspect ratio in table 3.1. It can be seen that the effect of curvature is negligible at $Ar = 500$ but, taking account of the accuracy with which the Strouhal numbers are given in bibliography, to obtain agreement with bibliographic results (see Fig. 3.1) the higher spatial discretization accuracy (8 collocation points) is needed.

3.3 Linear and non-linear marginal stability curve

3.3.1 The method

Because the base flow of the bifurcation triggering the three-dimensionality is periodically oscillating the standard method of numerical investigation of its linear stability is the Floquet stability analysis (see Barkley & Henderson (1996) for the case of straight cylinder and Sheard *et al.* (2003) for the case of tori of various aspect ratios). In our case we proceeded by adapting the 3D simulation for this purpose. As already mentioned, we settled to a torus of aspect ratio $Ar = 500$ to simulate the straight geometry. The expected linearly preferred wavelength being $4d$ (Barkley & Henderson, 1996) the corresponding number of periods M

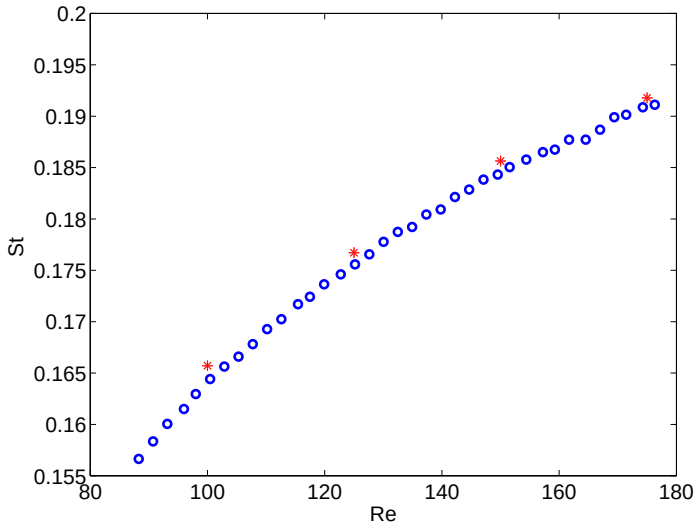

Figure 3.1: Strouhal numbers of the 2D flow past an infinite cylinder obtained with 8 collocation points per spatial direction of the spectral elements (red asterisks). Blue circles: experimental data by Williamson (1989).

around the torus is $\pi Ar/4 = 393$. The number M appears in the expansion (2.40) and (2.41) as a variable (integer) fundamental azimuthal wavenumber. The aspect ratio is large enough to provide a possibility of incrementation of the spanwise period by 0.25 %. The simulation has thus two parameters: M, equivalent to defining the spanwise period

$$\lambda(M)/d = \pi Ar/M, \tag{3.1}$$

and the Reynolds number Re. We are interested in the linear growth (decay) of the instability. In this case the only relevant mode of the expansion (2.40), (2.41) is $m = 1$. It is thus sufficient to truncate the expansion to modes $m = 0$ and 1. The non-linear coupling between both modes must be maintained because the mode 0 is unsteady and cannot be fixed unlike in Ghidersa & Dušek (2000) where the axisymmetry breaking occurs in a steady flow. As a consequence, some caution must be taken in order to avoid the reduction of the amplification (decay) rates due to saturation. This is done by keeping the perturbation of the mode $m = 1$ small and by verifying that the amplification (decay) is exponential. The numerical representation of individual Fourier modes being independent, the perturbation can be made virtually arbitrarily small without any loss of accuracy. The amplification (decay) of the mode breaking the two-dimensionality can be monitored by several ways. We followed the oscillations of one velocity component (mostly the transverse one) of the mode 1 at one or two 'history' points arbitrarily chosen in the cylinder wake and of the mode $m = 1$ of the spanwise skin friction coefficient

$$C_{f,z,1} = \frac{2}{U_\infty^2 d}\int_0^\lambda F_z(z)e^{2\pi iz/\lambda}dz = \frac{2}{U_\infty^2 d}F_{z,1} \tag{3.2}$$

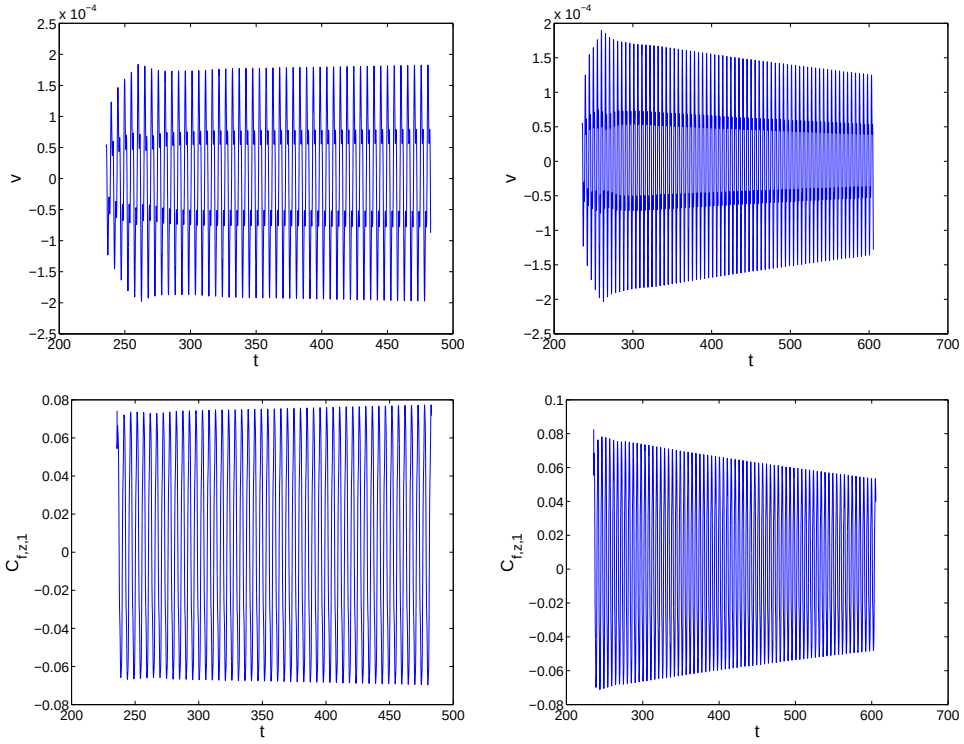

Figure 3.2: Amplification for $M = 373$ (left figures) and decay ($M = 360$, right figures) of the three-dimensional mode $m = 1$ at the Reynolds number $Re = 190$ (spanwise periods $\lambda/d = 4.21$ and 4.36, respectively). Upper row of figures: transverse velocity at the point $x = 12.5, y = 0, z = 0$, lower figure, the fundamental mode of the spanwise friction coefficient (3.2). Used mesh: see Fig. 2.4 with 6 collocation points per spatial direction.

where $F_z(z)$ is the spanwise force par unit span at the spanwise position z. There is no spanwise projection of the pressure force, so this force corresponds to the skin friction oscillating both in time and spanwise. The spanwise force is actually obtained by integrating the friction constraint of the mode $m = 1$ of the flow (see Jenny & Dušek, 2004, for more details) at the cylinder surface along the circle at the spanwise position z. In Fig. 3.2 we present both ways of monitoring of the growth of the spanwise mode for a subcritical and a supercritical Reynolds number.

The obtained numerical 'signals' are post-processed by extracting the oscillation amplitudes. The variation of the latter is verified to be exponential by checking if the logarithm varies linearly. The amplification rates are then obtained by linear regression (see figure 3.3).

3.3.2 Results

To capture the interval of unstable wavelengths for the instability responsible for the transition to instability (i.e. for the onset of mode A - see Sec.1.2) the procedure described above

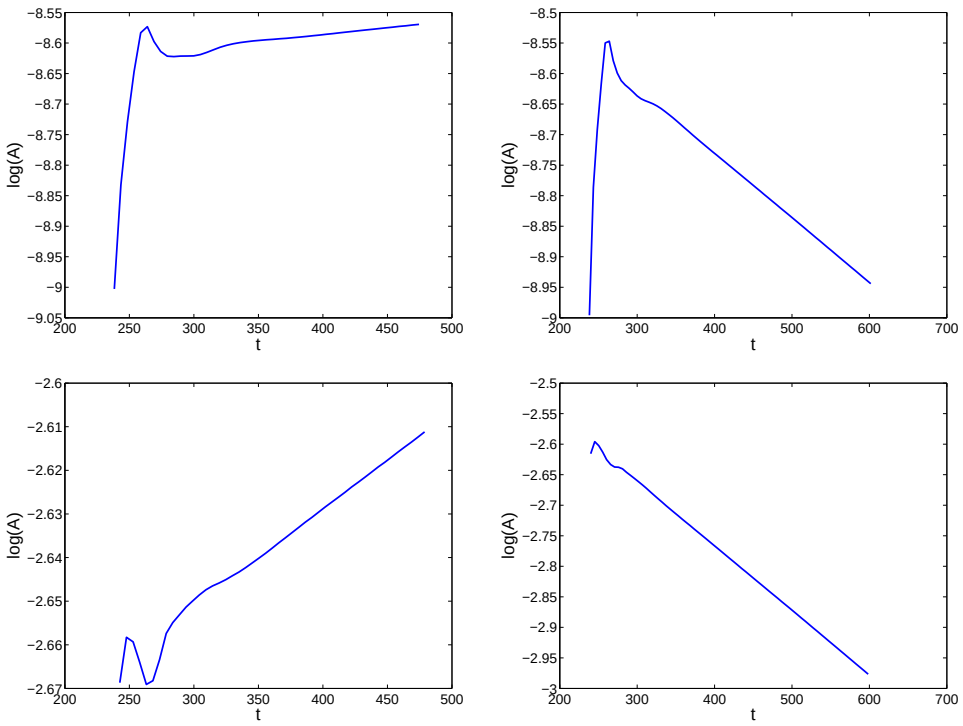

Figure 3.3: Logarithms of the amplitudes of oscillations of Fig. 3.2. The corresponding amplification rates are $\gamma = 2.25E-04$ for $M = 373$ and $\gamma = -1.06E-03$ for $M = 360$. By interpolation, the critical wavenumber is $M = 370.7$. In this figure and fig. 3.2, we chose to represent two cases of wavenumbers that are farther from the critical one than actually used for interpolation. We actually increased M by a unit. As a result, the accurate value of the critical wavenumber is i.e.$M = 370.2$, which corresponds to the spanwise wavelength $\lambda_{crit} = 4.24d$ at this Reynolds number (190).

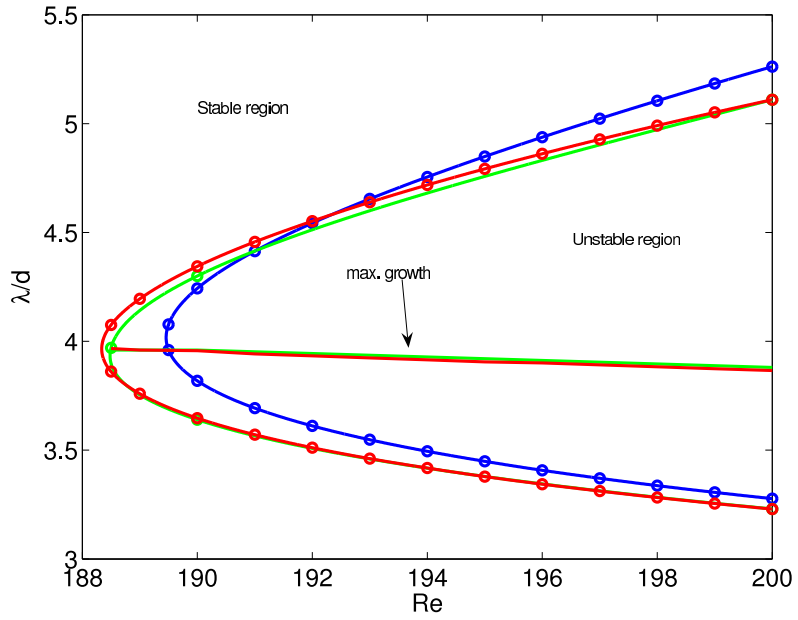

Figure 3.4: Linear marginal stability curve for low and higher resolution (6 and 8 collocation points per spatial direction) - blue and red lines with circles respectively, the circles represent computed values. The green line with circles interpolates 5 data points by Henderson & Barkley (1996). The present study with 6 and 8 collocation points gives the critical Reynolds number 189.5 and 188.3 respectively and both lie in the interval given by Henderson & Barkley (1996).

(Sec. 3.3.1) was repeated for Reynolds numbers starting from 189.5 and then increasing by one from 190 until 200. In the process, not only the critical wavelengths but also those corresponding to a maximum growth rate were determined. The so obtained marginal stability curve is represented in Fig. 3.4. The linearly stable region lies to the left of this curve and the region linearly unstable to three-dimensional perturbations lies to the right of the curve. The critical Reynolds number and the preferred wavelength correspond to the $Re - \lambda$ coordinates of the cusp (the left-most point) of the curve. For comparison, results obtained with 6 and 8 collocation points are plotted and the marginal stability curve of Henderson & Barkley (1996) is also represented. In the first case we obtain a critical Reynolds number of 189.5 and a preferred wavelength of $4.02d$ in the second case 188.3 and $3.97d$, respectively. Both lie within the interval set in Henderson & Barkley (1996), the second values are in excellent agreement with those of Henderson & Barkley (1996). However, since the investigation of non-linear effects requires high computing costs, we preferred to keep the lower spatial resolution when investigating non-linear effects. The figure represents also the line of maximal growth known to have the trend towards shorter wavelengths for increasing Reynolds number.

3.4 Non-linear marginal stability curve

3.4.1 Aim of the investigation

The paper by Henderson & Barkley (1996) presents a subcritical bifurcation diagram (inset of Fig. 5 of the cited paper) reproduced in Fig. 1.11 of chapter 1. Although it has become well-known that the instability is subcritical, it is the only evidence of its subcriticality found in the bibliography. The evidence of Henderson & Barkley (1996) is, however, far from complete. Firstly, the demonstration of the bi-stability is limited to only one Reynolds number value ($Re = 185$). Does it mean that at a lower Reynolds number the bi-stability no longer exists or was the value chosen fortuitously? Secondly, only the preferred spanwise wavelength has been chosen as a spanwise period of the simulation. What happens if the spanwise period is varied? Thirdly, as indicated in Sec. 1.2, the bibliography is marked by an implicit assumption that the preferred spanwise wavelength is the physically relevant period for 3D simulations. If so, what is the explanation of the fact that the evidenced bi-stability interval of Reynolds numbers $(185, 188.5)$ is so small in comparison with the experimental observation of bi-stability of a state of parallel vortex shedding and of a flow dominated by the mode A as low as at Re =172.8 (Williamson, 1988*b*). To bring an answer to the first two questions we varied the spanwise period of the non-linear simulation described in Henderson & Barkley (1996) relatively slightly about the preferred spanwise wavelength of $4d$. The maximal spanwise wavenumber of the spectral Fourier spanwise expansion (2.40,2.41) was taken to be $m = 6$ which guaranteed an independence of the truncation of the spanwise expansion. In view of the large number of relatively long simulations necessary for the investigation, the accuracy was downgraded to 6 collocation points per spatial direction. (I.e. the blue linear marginal stability curve of Fig. 3.4 is relevant for the determination of linear stability thresholds for the considered spanwise periods.)

3.4.2 Method

We investigated the cases of spanwise periods $3.49d, 3.93d, 4.01d, 4.49d, 5.24d$ and $6.28d$. As explained above, these values correspond to fundamental azimuthal modes M (see Eqs. (2.40,2.41)) decreasing from $M = 450$ to 250 by a decrement of 50. In addition, the preferred wavenumber $M = 392$ was also considered. For each spanwise period, we started with a slightly supercritical Reynolds number (e.g. $Re = 190$ for $\lambda = 4.01d$) and let the saturated state be reached. In all cases we obtained the typical pure mode A (see Figs. 3.5, 3.6). Let us remark, that the saturated state in Fig. 3.5 a) is not exactly periodic and that a small chaotic modulation is present. Once the saturated mode obtained above the linear instability threshold, we decreased the Reynolds by one at each time and monitored the time evolution of the mode. The attractor being a (almost perfect) limit cycle, the monitoring of any quantity vanishing in the case of parallel vortex shedding provides the necessary information. In this case we monitored the mode 1 of the transverse velocity at a point lying at the flow (x-) axis 12.5 diameters downstream of the cylinder. Either, after the decay of transients, a slightly lower level of saturation was reached (actually it remained almost independent of the Reynolds number in the whole interval of bi-stability) as seen in Fig. 3.5 b) or the amplitude of the mode A decayed to zero (Fig. 3.7). To prove that the decay tends

to zero and not to some significantly smaller but still non zero value, we post-processed the time 'signal' (upper figure 3.7) to extract the amplitude as a function of time and represented the latter on a logarithmic scale (lower figure 3.7). It is clear that to obtain a saturation or to evidence an exponential decay runs over a very large number of vortex shedding periods are needed. About 30 such runs were needed for the presented study.

3.4.3 Results

Fig. 3.8 represents the amplitude of oscillation of the transverse velocity of the mode A at the point $x = 12.5d$, $y = 0$, $z = 0$, measured as that of the real part of the fundamental azimuthal mode of the spanwise velocity decomposition, obtained for six forced spanwise periods: $6.28, 5.24, 4.49, 4.01, 3.93$ and $3.49d$. Taking the case of spanwise period $4.01d$ as an example, we can see that below the linear instability threshold at $Re = 189.5$, the oscillations keep the same amplitude at Reynolds numbers down to 185 (albeit with some scatter due to the difficulty to reach a perfect saturation). When Re is decreased from 185 to 184, the oscillation at $Re = 184$ decays to zero exponentially as demonstrated in Fig. 3.7. We already mentioned that the oscillations are not perfectly periodic at $Re = 190$ (see Fig. 3.5). This is the case, actually, for all $Re > 186$. We observe a less than 5% quasiperiodic modulation at $Re = 187$. At $Re = 190$ the modulation is not much stronger but has no longer any visible periodicity. Strictly speaking the state is thus chaotic. The modulation of the fundamental mode of the spanwise Fourier expansion is however so weak that its (second order) effect on the 2D (zero) mode and by the same token on the whole 3D flow is negligible. To go back to the most important observation, let us sum up that between the Reynolds number values of 184 and 185 the non-linear branch of the solution lost its stability which shows the existence of a hysteresis interval of roughly [185,189.5]. Figure 3.8(a) represents also the case of spanwise periodicity $3.49d$. Its basic interest is that, in this case, the hysteresis is very close to disappear. For shorter spanwise periods the bifurcation is no longer subcritical. On the other hand the bi-stability interval becomes very large for larger spanwise period. The quantitative characteristics of the bi-stability evidenced for different spanwise periods are summed up in Table 3.2.

The standard method of investigation of the linear stability of configurations where a second parameter (wavelength or, equivalently, wavenumber) in addition to the Reynolds number is needed to determine the instability threshold consists in plotting a marginal stability curve. There is no reason why not to apply the same method for representing the lower limits of the bi-stability intervals. The curve joining these points in the $Re - \lambda$ plane represents the marginal stability curve of the non-linear state. In what follows, we shall call it non-linear marginal stability curve. The latter lies to the left of the linear curve in the Reynolds - wavelength plane. In the case of the circular cylinder wake the obtained curve is represented in Fig. 3.9 along with the linear marginal stability curve obtained with same spatial discretization accuracy. Both curves join roughly at $Re = 194$ and for the wavelength of 3.49 d. The surface between both curves corresponds to the bi-stability region. In a 3D representation representing the amplitude in a third direction, the non-linear marginal stability curve would represent the rim of the locus of stable non-linear states. If this new curve had a similar left hand pointing cusp as the linear marginal stability one there would

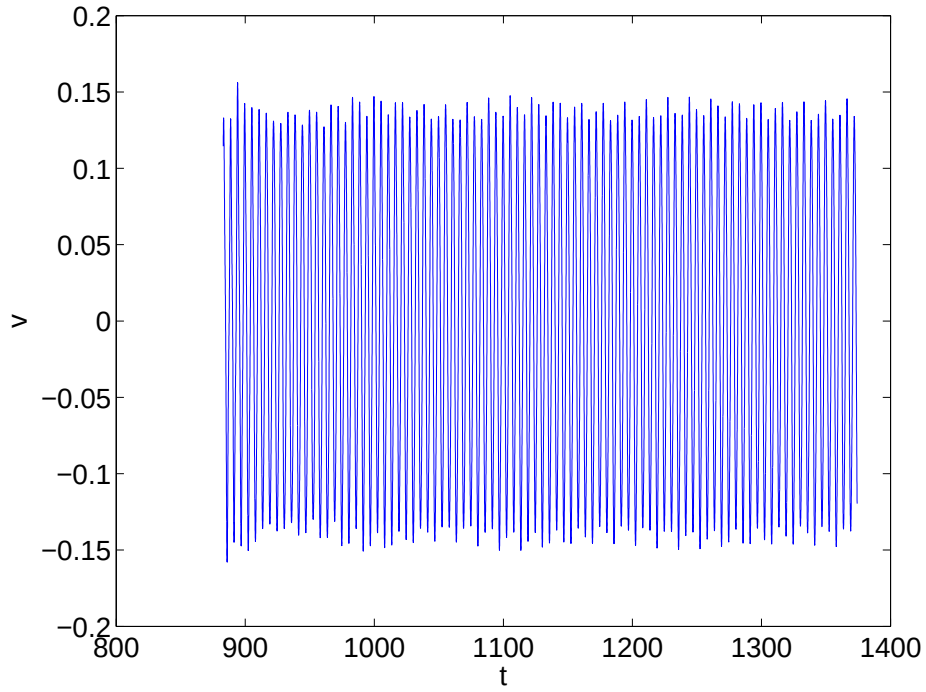

(a)

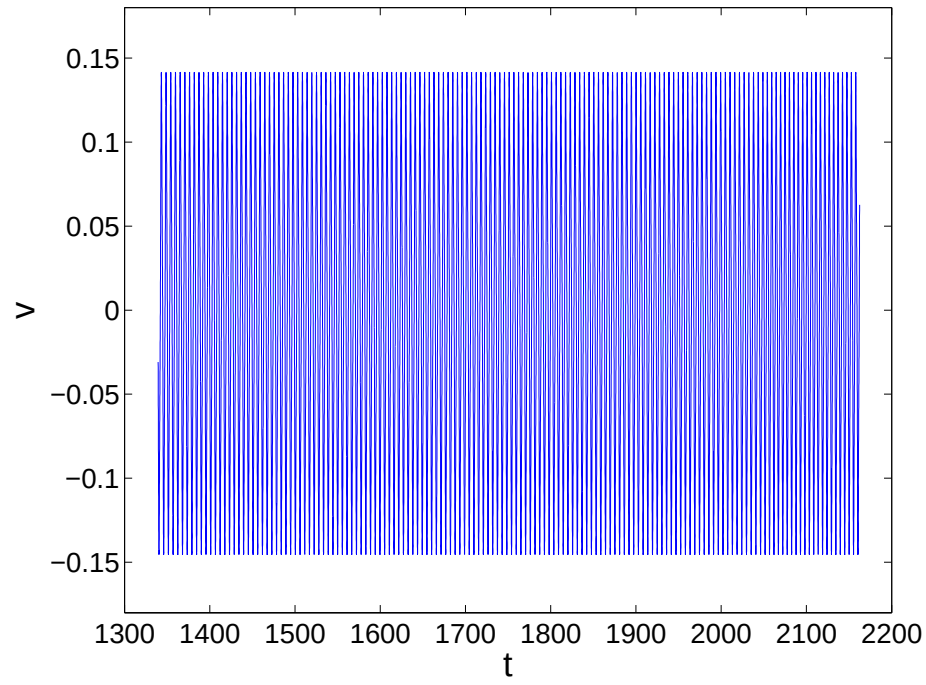

(b)

Figure 3.5: Saturation of the mode A at $Re = 190$ (a) and $Re = 185$ (b) in a simulation with spanwise period $4.01d$. The mode 1 of the transverse velocity at the point $x = 12.5d, y = 0, z = 0$ is represented as a function of time.

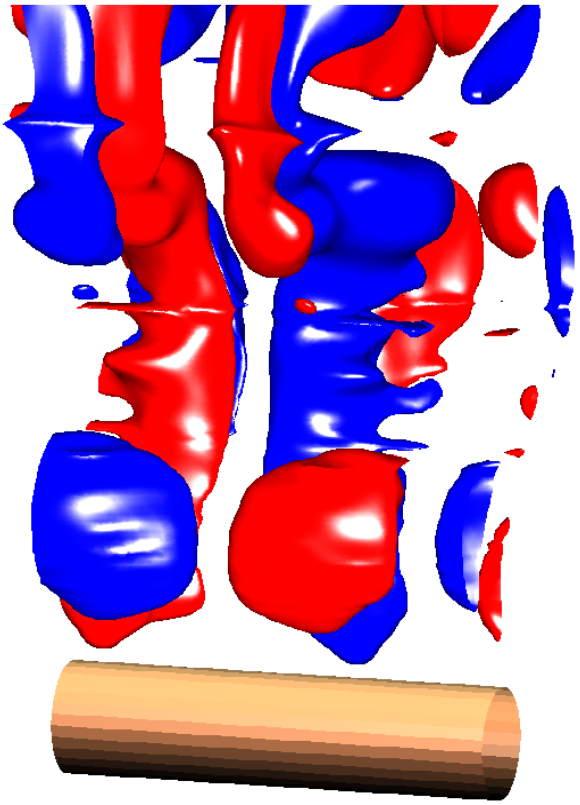

Figure 3.6: Pure A-mode at $Re = 190$ with forced spanwise periodicity of $4d$. The flow structures are represented in terms of iso-surfaces corresponding to the spanwise velocity equal to $\pm$ 0.08 ($\pm$ 8% of inflow velocity).

spanwise period	Re_{crit}	Re_{min}	A	St
3.49	194.1	194	0.080	0.203
3.93	189.6	186	0.141	0.189
4.49	191.6	180	0.134	0.187
5.24	199.7	173	0.132	0.184
6.28	235.2	161	0.112	0.181

Table 3.2: Physical characteristics of the hysteresis for variable spanwise periodicity. The results are obtained with 6 collocation points of the spectral element discretization. Re_{crit} - critical Reynolds number for the linear onset of three-dimensionality, Re_{min} - minimal Reynolds number of the three-dimensional branch of the solution. A: Amplitude of oscillations of the transverse component of the fundamental Fourier mode at the point $x = 12.5d$, $y = 0$ as a fraction of inflow velocity at Re_{min}. St: Strouhal number at Re_{min}.

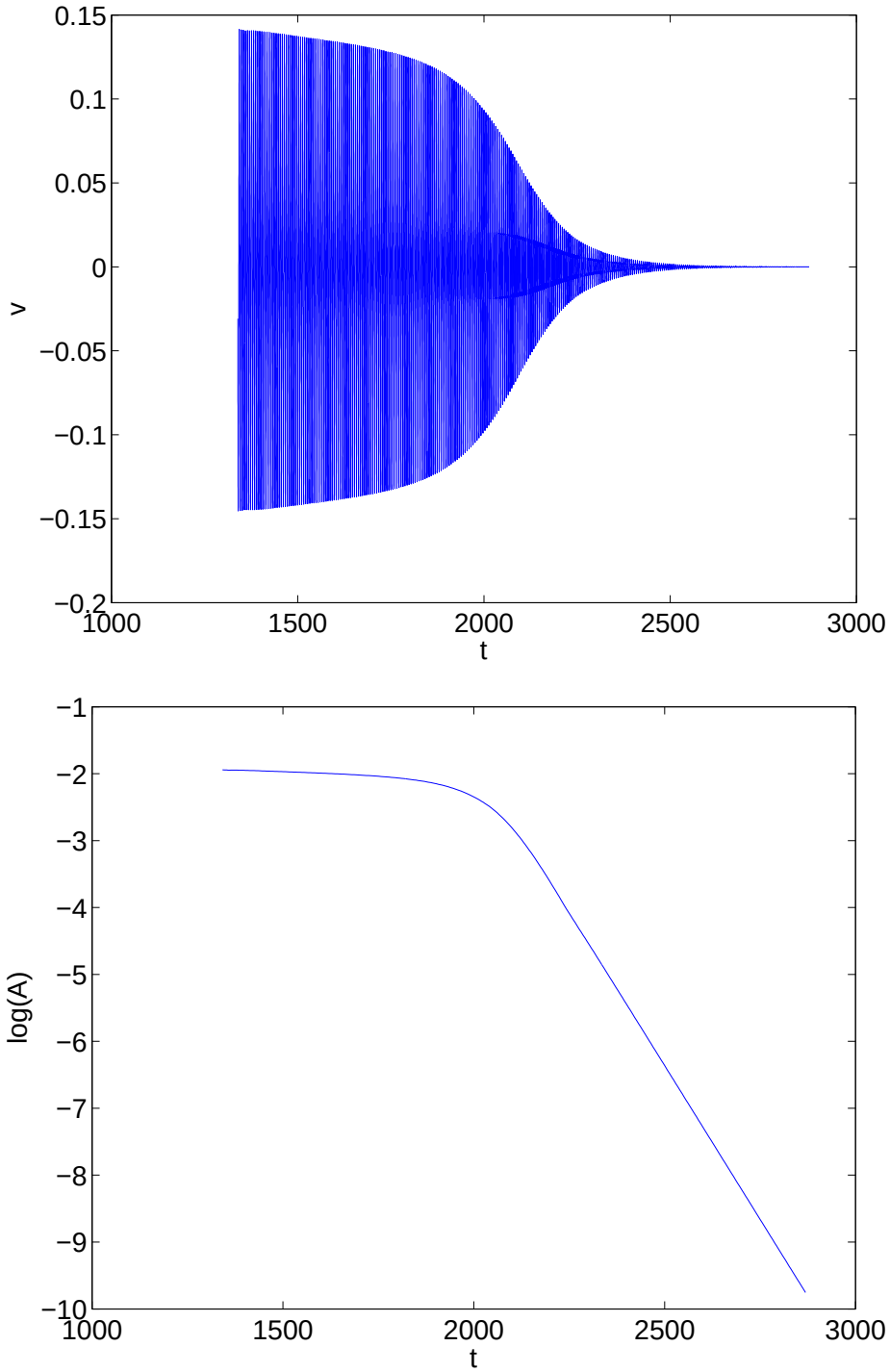

Figure 3.7: Decay of the mode A to zero at $Re = 184$ for a forced spanwise periodicity of $4d$. Upper figure: The mode 1 of the spanwise velocity at the point $x = 12.5, y = 0, z = 0$ represented as a function of time. Lower figure: Logarithm of the amplitude of oscillations in the right figure as a function of time.

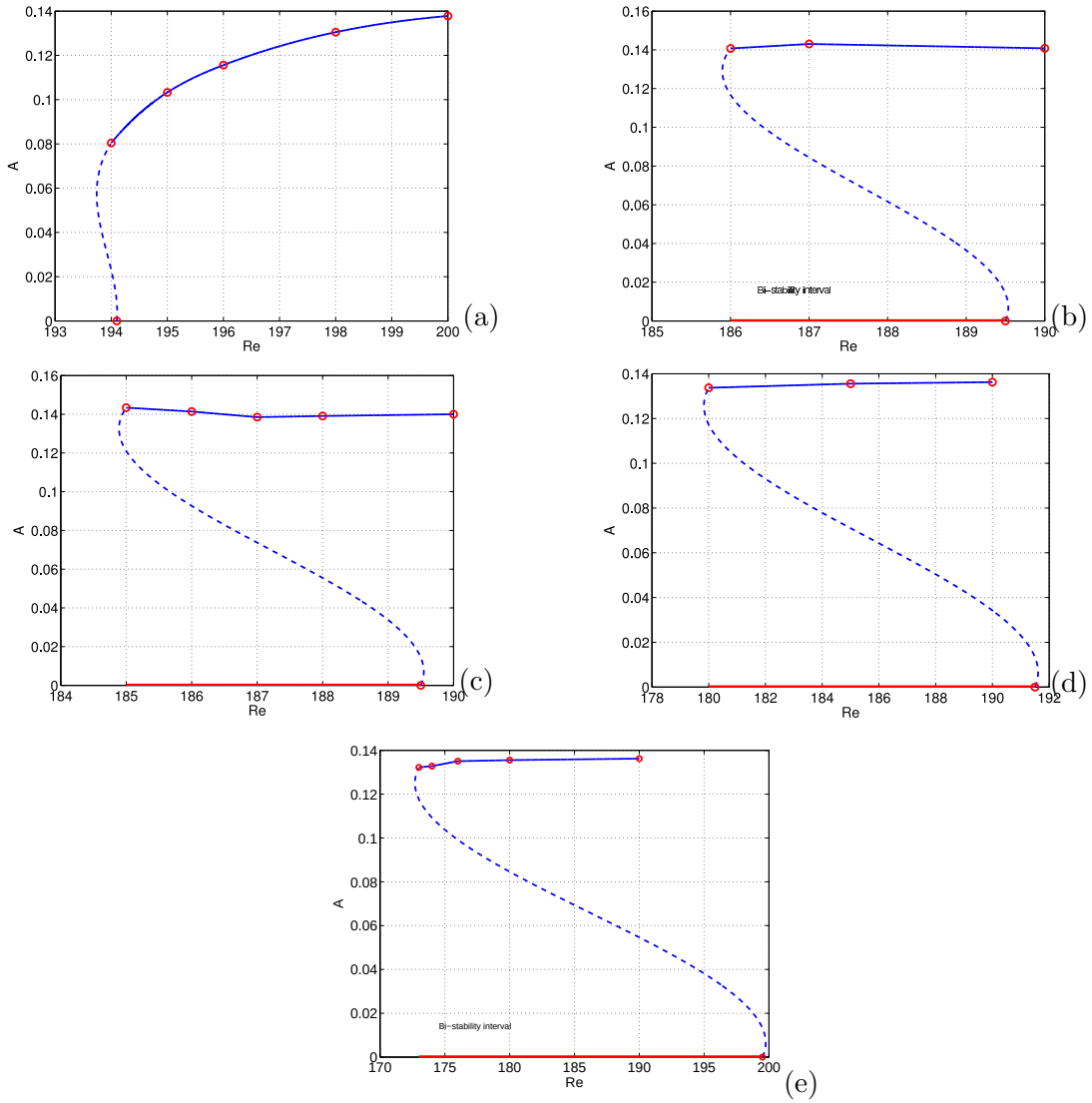

Figure 3.8: Subcritical bistability interval for the spanwise periodicity of Fig. (a) 3.49d, (b) 3.93d, (c) 4.01d, (d) 4.49d and (e) 5.24d. The vertical axis represents the amplitude of oscillations of the fundamental Fourier mode of the transverse velocity at a point x=12.5d downstream of the cylinder axis and in the flow symmetry plane ($y = 0$). The red circles represent computed values. Dashed lines are hypothetical unstable branches separating the attraction basins of the 2D solution (horizontal axis) and of the strongly non-linear one (solid line). The evidenced bi-stability interval is visualized as a thick red solid line along the horizontal axis (e.g. [185,189.5] in Fig. (c)).

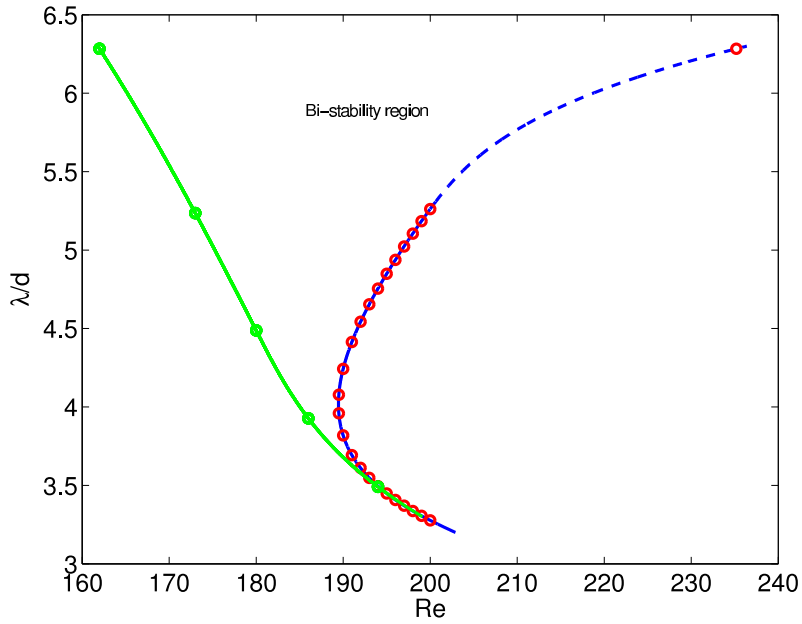

Figure 3.9: The linear and non-linear marginal stability curves (blue line - solid and dashed - with red circles and green solid line with green circles, respectively), both at low resolution.

also exist an absolute threshold in terms of the Reynolds number for the existence of the non-linear state and the usual considerations assuming that close to such a threshold a preferred wavelength can found would apply. In contrast, in the present case, we observe, that, on the large scale side, the gap between both curves widens and that the non-linear curve does not tend to present a vertical tangent. At half the critical wavelength it opens the way to subharmonic scales. There is thus no reason to consider that large scales will be cut off.

3.5 Non-linear drop of the Strouhal number

In spite of a short spanwise period (2.25 and 3.72d) Persillon & Braza (1998) report an almost 10% drop in wake frequency due to the onset of three-dimensionality at $Re = 200$. This positions the obtained numerical points in the Re–St plane close (a little below) to the problematic section of the many times reproduced Williamson's experimental curve (see e.g. Williamson, 1996b). This difference between the numerical value of Strouhal number obtained by two-dimensional numerical simulation of parallel vortex shedding and the experimental data of Williamson (1996b) is, in contrast, very small outside the interval in which the mode A was experimentally observed to dominate. The discontinuity of St vs. Re has thus been attributed to the presence of A-mode structures in the wake. We found the same qualitative trend whenever the A-mode is present in the simulation (see Table 3.2).

In figure 3.10 we reproduced the Williamson's Strouhal-Reynolds relationship zooming on the domain of the 'first discontinuity' (blue dots). The red circles represent our val-

ues corresponding to parallel vortex shedding. To represent the effect of three dimensional structures, we define the shift of the Strouhal number:

$$\xi = (St_{\parallel} - St)/St_{\parallel} \tag{3.3}$$

where $St_{\parallel}$ is the Strouhal number of the parallel vortex shedding taken on the dotted curve in figure 3.10 obtained by a second degree regression of the computed points. The corresponding shifts are represented in figure 3.11. In addition, the value of Persillon & Braza (1998) obtained at $Re = 190$ and for a spanwise periodicity of $2.25d$ is plotted as an upward pointing triangle. As explained in the previous section, while determining the non-linear marginal stability curve, we swept (downward) an interval of Reynolds numbers for an increasing spanwise period. In the process we obtained Strouhal numbers for spanwise periods of 3.93, 4.49, 5.24 and $6.28d$ reported in table 3.2. The Strouhal numbers were found to decrease as a function of the spanwise period for the shortest periods to become constant afterward. At $Re = 190$ we represented the shifts of simulations ran for spanwise periods 3.93, 4.49 and $5.24d$ as three black dots. The dots are arranged in the upward order. It is to be noted that in most cases the downward shift of the Strouhal number is overestimated . In addition to the question as to what the real physical hysteresis interval is, the question of the physically correct Strouhal number is thus raised. Both are related to the scale of the spanwise periodicity.

3.6 Large spanwise scales

Even if, eventually, at some very large scale the non-linear marginal stability curve presented a limited wavelength interval this would not exclude the existence of large scale structures. Henderson (1997) analyzed the behavior of the flow for spanwise wavelengths four times and sixteen times larger than the mode B wavelength ($4 \times 0.822d = 3.288d$ and $16 \times 0.822d = 13.152d$) at $Re = 265$. As argued by Henderson (1997), a sufficiently wide interval of scales can combine, due to the non-linearities, into any smaller scales. Our non-linear marginal stability curve provides an unlimited interval, for this reason it can be expected that large scale structures can be obtained even with a limited, albeit enlarged, spanwise periodicity. In this section we show that this is, indeed, the case by running simulations with a spanwise period of roughly 8 times the preferred linear spanwise wavelength of the mode A (31.4 d). The principal purpose is to investigate the lower limit of stability of the state dominated by the mode A and to see if enlarging the spanwise period allows us to get closer to experimental observations. In spite of all effort to optimize the computing efficiency, the simulations ran for many weeks. As a result, only three subcritical Reynolds numbers (185,170 and 160), could be investigated. It can be said that the simulations presented in this chapter are at the limit of feasibility with available computing resources.

As mentioned in Henderson (1997), the computing costs of simulations with large spanwise period are associated to the large number of spanwise Fourier modes to be accounted for. The largest relevant spanwise wavenumbers are determined by dissipation. Our previous tests showed that six times larger wavenumber than that corresponding to the A-mode wavelength was sufficient to be accounted for in order to obtain numerically converged results in

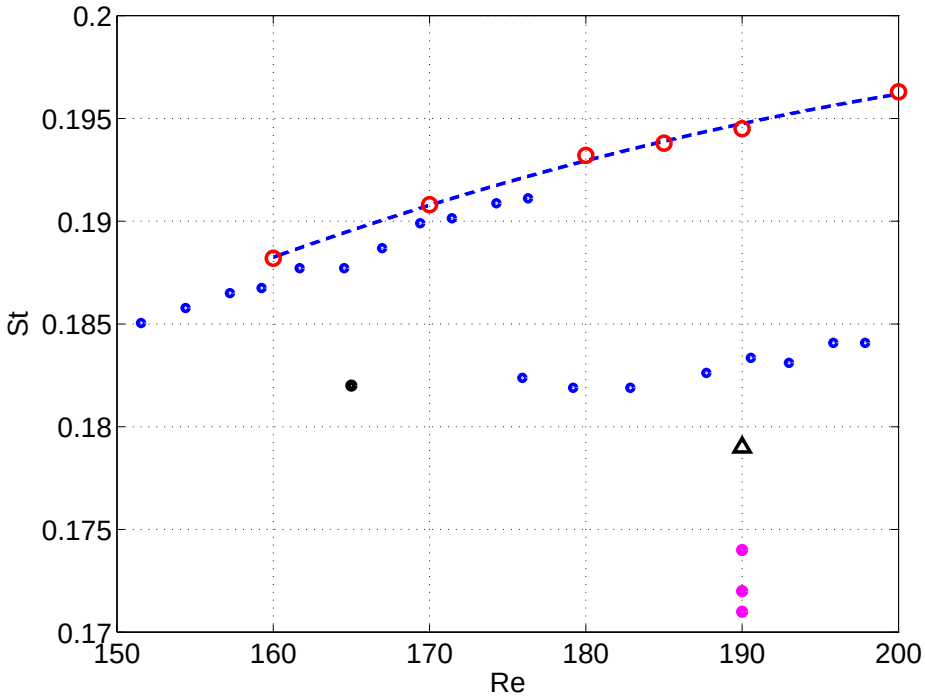

Figure 3.10: Zoom on the experimental values of Strouhal numbers of Williamson (1996*b*) (blue dots) due to the presence of spanwise structures. Red circles: Strouhal numbers of parallel vortex shedding computed by a 2D simulation with 8 collocation points. Triangle: value reported by Persillon & Braza (1998).

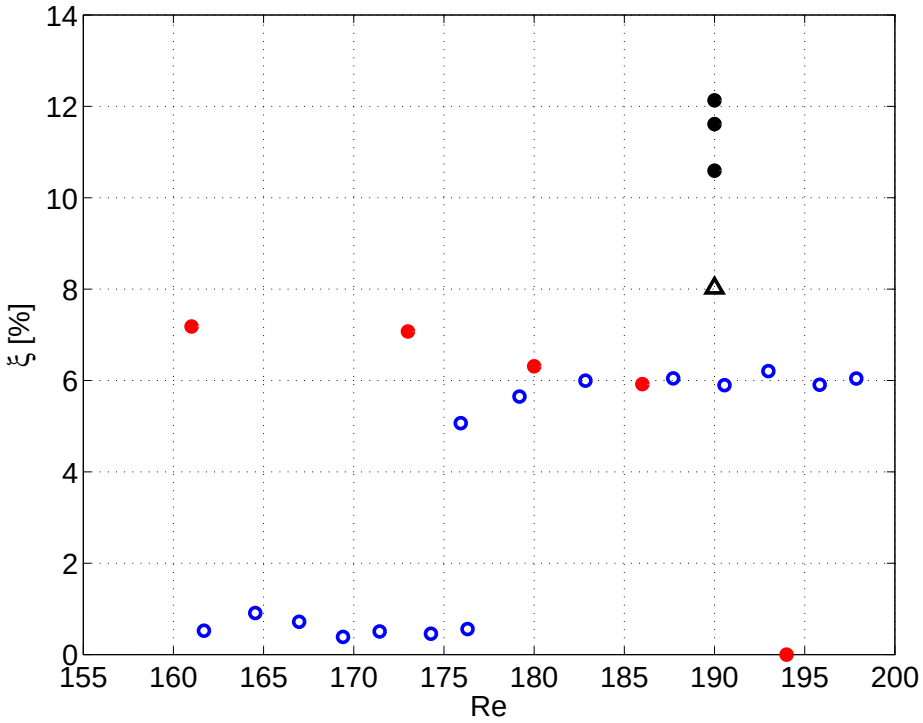

Figure 3.11: Strouhal number shift due to the presence of spanwise structures. Blue circles: reprocessed data of Williamson (1996*b*). (The seven points distributed along the horizontal axis correspond to a parallel vortex shedding and indicate the error of the definition of the shift.) Upward pointing triangle: numerical result of Persillon & Braza (1998) for a numerically imposed spanwise period of $2.25d$. Black dots at $Re = 190$: Strouhal numbers of the 3D, A-mode dominated, wake with spanwise periodicity, respectively from bottom to top, 3.93, 4.49 and $5.24d$. Red dots: shifts of Strouhal numbers at the lower limit of the bi-stability interval reported in table 3.2

computations with the spanwise periodicity close to $4d$. The smallest wavenumber is given by the spanwise periodicity. If we increase the spanwise period by 8, we get 49 terms for a real Fourier expansion and 98 for a complex one. For the fast Fourier expansion implemented in our code, it is necessary to have a power of two. For this purpose we downgraded a little the accuracy of the spanwise decomposition by cutting off a little more the small spanwise scales to limit it to 64 complex modes. This equivalent to cutting off the expansion (2.40, 2.41) at $m = 31$. As a result, it was possible to run simulations for very large physical time intervals: as much as 160 vortex shedding periods at $Re = 170$. To verify the trends of the computed spanwise spectra we ran two computations (at $Re = 185$ and $Re = 170$) with truncation at the 48-th spanwise harmonic over several vortex shedding periods. This provided spectra extended in a continuous way to shorter scales without affecting the already resolved ones. The shorter spanwise expansion contains, nevertheless, enough modes to capture length scales corresponding to the mode B. The latter has been observed to have a spanwise wavelength about four-times shorter as the mode A. This corresponds roughly to the highest mode of the truncated expansion. As will be shown below (Sec. 3.7), at low Reynolds numbers, at which the presence of mode B will be investigated, the latter appears to lie well within the interval of spanwise wavenumbers of the truncated expansion.

3.6.1 Re=185

The initial condition at $Re = 185$ was created using the (purely periodic) solution obtained at the same Reynolds number with a spanwise period of $4d$. The iso-surfaces of spanwise velocity at iso-value equal to $\pm$ 0.1 (10% of inflow velocity) for $Re = 185$ with a spanwise periodicity of $4d$ are shown in figure 3.12 (see also Fig. 3.6). These large scale structures represent a pure A-mode. To initialize a computation with 8-times larger spanwise period, the original Fourier modes m were copied to modes $8m$. E.g. the $4d$ period corresponds now to one eighth of the fundamental period, i.e. $m = 8$. The resulting spanwise spectrum presents thus a peak every 8-th mode characteristic of the original short-scale mode A periodicity. The newly opened subharmonic degrees of freedom remain exactly zero unless they are perturbed. To excite all spanwise scales available we excited the largest scale Fourier mode - the fundamental mode of the new expansion - by filling it with the original fundamental A-Fourier mode (now 8-th harmonic). The maximum amplitude of the w component of the A-mode at this Reynolds number is about 0.2 of inflow velocity (to be compared to more than 0.6 for the amplitude of the transverse velocity component oscillations). The perturbation then redistributed to other modes due to the non-linearities. The flow appeared to be significantly chaotic with many rapidly varying small scale structures. The latter ended up by triggering non-linear numerical instabilities. Nevertheless, as many as 40 vortex shedding periods could be obtained (as compared to the paper by Henderson (1997) where 25 periods are simulated.) The numerical instabilities of the spectral element method are relatively frequent. A filter making it possible to prevent them has been proposed by Fischer & Mullen (2001). It failed, however, in this case. To remove the numerical instabilities, an enhancement of the spatial resolution, namely in the wake, was attempted. For this purpose a 590 element spectral element mesh with 8 collocation points per spatial direction was used. The computing costs have thus been multiplied by 4 and only a few vortex shedding periods were simulated to

demonstrate the possibility to continue the simulation. Due to the limited physical time of the simulation and to the chaotic nature of the solution it is somewhat difficult to conclude if the simulated time is sufficient to obtain an established state. This can be seen particularly well in the next section 3.6.2 where a much longer simulation is presented and where it is made obvious that large spanwise scales are accompanied with extremely large time scales.

The case of $Re = 185$ is basically investigated to illustrate a transition between the known, periodic, A-mode with spanwise period $4d$ to a chaotic solution with an 8 times larger periodicity at the same Reynolds number. We focus thus rather on the trend.

As for the energy redistribution, the trend is represented by the spanwise energy spectra separated by a time interval of about 25 vortex shedding periods in Fig. 3.13. The energies of spanwise modes are defined, in agreement with Henderson (1997), as integrals over the flow domain of the squares of the velocity modes normalized so that the asymptotic flow has an energy of 0.5. The spanwise energy spectra represented in Fig. 3.13 are averaged over one vortex shedding period (5 time units). The modes are numbered from $m = 0$, representing the spanwise average, to m_{max} (= 31 or 48). $m = 1$ is the fundamental mode corresponding to the wavelength $31.4d$. Mode $m = 8$ has a spanwise period of $3.93d$, close to the linear preferred wavelength. The energy of mode 0 is close to 0.5 because the largest part of the computational domain contains an almost unperturbed flow. For this reason, it does not provide direct information on 3D effects and is not represented in the graphs of spanwise spectra. It can be seen that the spanwise periodicity of mode A is still clearly dominant in the upper spectrum but has largely vanished in the spectrum plotted in the lower figure 3.13. The secondary peak, corresponding to mode A, is situated between the 5-th and 8-th mode, i.e. is shifted to a longer wavelength than the initial condition. A fairly continuous decay of smaller wavelength modes is observed. It is to be noted that the large scale $m = 1$ mode (with spanwise periodicity $31.4d$) is dominant. This means that large scale modulation is significant.

This is easily explained by the large scale modulation of the instantaneous wake at $t = 177$ represented in figure 3.14. The A-mode determines the small scale structures in the near wake but, in the far wake, only a pair of structures is visible at the represented level of iso-surfaces. (The A-mode size structures are, of course, visible if the iso-level is lowered.) 'Empty' spots can be seen between 10 and 15 diameters downstream of the cylinder. They might be associated to 'vortex dislocations' (see Williamson, 1992). The original, relatively short, periodicity of $4d$, i.e. 8 periods in the present spanwise domain, is thus now strongly modulated at the largest available scale corresponding to the whole domain length, i.e. with a single period spanwise. It can be concluded that the arising disorder very likely prevents the flow from having, physically, any periodicity, i.e. that, very likely, a similar picture would be obtained if the spanwise period is further significantly increased.

The flow presents a spatio-temporal chaos. The onset of temporal chaos is illustrated by representing the transverse velocity component of the $m = 1$ and $m = 8$ Fourier modes at the point $x = 12.5d$ and $y = 0$ of the flow in Fig. 3.15. All Fourier modes behave similarly. They loose their initial periodicity and their oscillations become chaotic.

The Strouhal number of a chaotic flow is not so well defined as for a purely periodic case. However, the 2D ($m = 0$) Fourier mode averaging the effect of all spanwise scales keeps two convenient features of a 2D flow. It remains fairly periodic and the frequency of its

oscillations remains very close to uniform throughout the flow. Since it dominates the flow it is representative of the flow oscillations. It was used to determine the Strouhal number. Strouhal numbers obtained at points lying 1.4 and 12.5d downstream of the cylinder axis differed by 0.1% only. A real experimental configuration consists in placing a point-wise probe in the wake. This corresponds to specifying a spanwise position and to measuring the velocity fluctuations in the physical space. Numerically, this corresponds to re-composing the computed spanwise Fourier modes. We did this for the two points $x = 1.4, 12.5$, $y = 0, z = 0$. A representation of the difference between the local and spanwise averaged signal is provided in Fig. 3.21. The local value is subject to chaotic fluctuations affecting higher spanwise modes, however, if the Strouhal number is computed from zero crossings no systematic accumulation of delay of one signal with respect to the other is observed. At the start of the simulation the Strouhal number was found 11%, at the end only 9% , lower than that of the 2D wake at the same Reynolds number (see the filled squares plotted at $Re = 185$ in figure 3.16). The experimentally evidenced drop seems to be rather 6%. The trend of the simulation to converge toward the experimentally observed Strouhal number drop is, however, qualitatively correct. A Strouhal number corresponding to a 5% drop was found from analyzing the $m = 1$ Fourier mode. It can be concluded that the Strouhal number of the ordered A-mode dominated flow is lower than experimentally observed but that the development of chaos tends to uncouple the synchronization of the 2D vortex shedding with three-dimensional structures and to yield Strouhal numbers closer to experimental measurements.

3.6.2 Re=170

The longer spanwise periodicity integrates the effect of the widening interval of bi-stability evidenced by the non-linear marginal stability curve (figure 3.9). It can thus be expected that the stability interval will be extended significantly below $Re = 185$, the lower bi-stability evidenced by Henderson & Barkley (1996) and confirmed by us for a spanwise periodicity of 4d. We have already mentioned that Williamson (1988b) reports a bi-stable case as low as at $Re = 172.8$. Originally, we decided to run a simulation at $Re = 170$ to delimit the bi-stability interval roughly from below. We expected to obtain a 'relaminarization' to a parallel vortex shedding, i.e. a decay of all non zero modes of the spanwise expansion. The last obtained solution at $Re = 185$ was used as initial condition. The solution remained fully three-dimensional and chaotic with a similar spatial pattern as at $Re = 185$. The weaker fluctuations made it possible to run the simulation without the problem of numerical instabilities. We continued the run for 160 vortex shedding periods and reached a fairly established state (see Fig.3.17).

The time interval of the figure 3.17 corresponds to about 60 vortex shedding periods and starts 100 periods after the initial condition (end of the simulation at $Re = 185$) has been applied. The solution is well established, i.e. no qualitative trend is visible in the plot. All represented modes fluctuate randomly within the same decade. The mode 1 (corresponding to the largest captured wavelength of 31.4d) does not dominate all the time, which indicates the intermittent nature of large 'vortex dislocations'. It is to be noted that the time scales of the variations of the mode 1 are on the order of 20 vortex shedding periods. This explains why a very long simulation run is necessary to reach and to verify an established chaotic

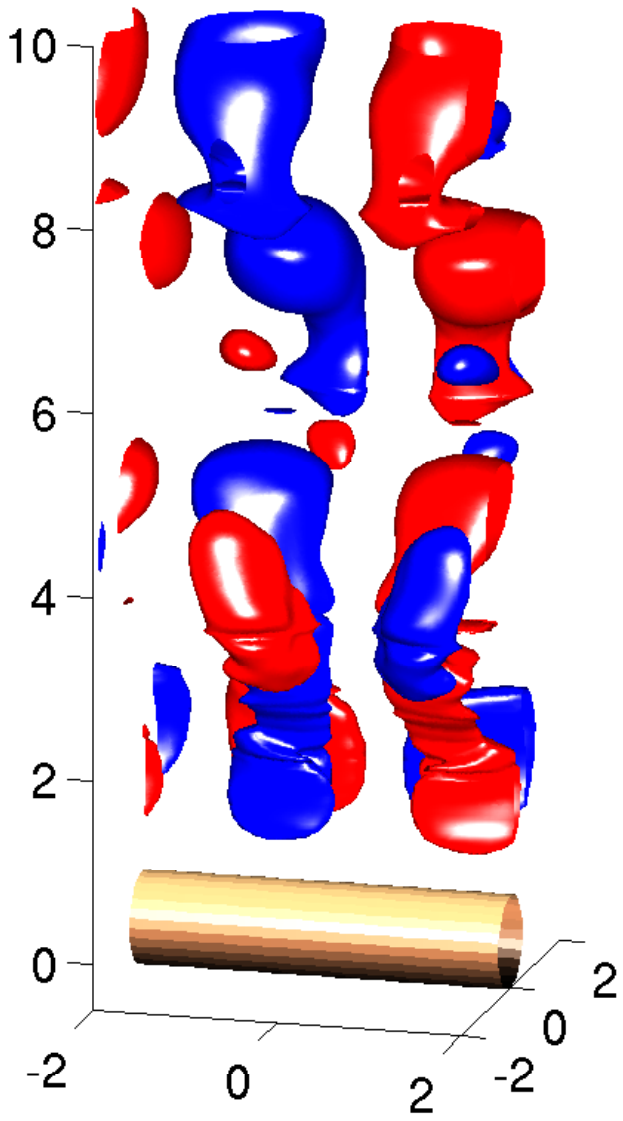

Figure 3.12: Pure A-mode at $Re = 185$ with forced spanwise periodicity of $4d$. The flow structures are represented in terms of iso-surfaces corresponding to the spanwise velocity equal to $\pm$ 0.1 ($\pm$10% of inflow velocity).

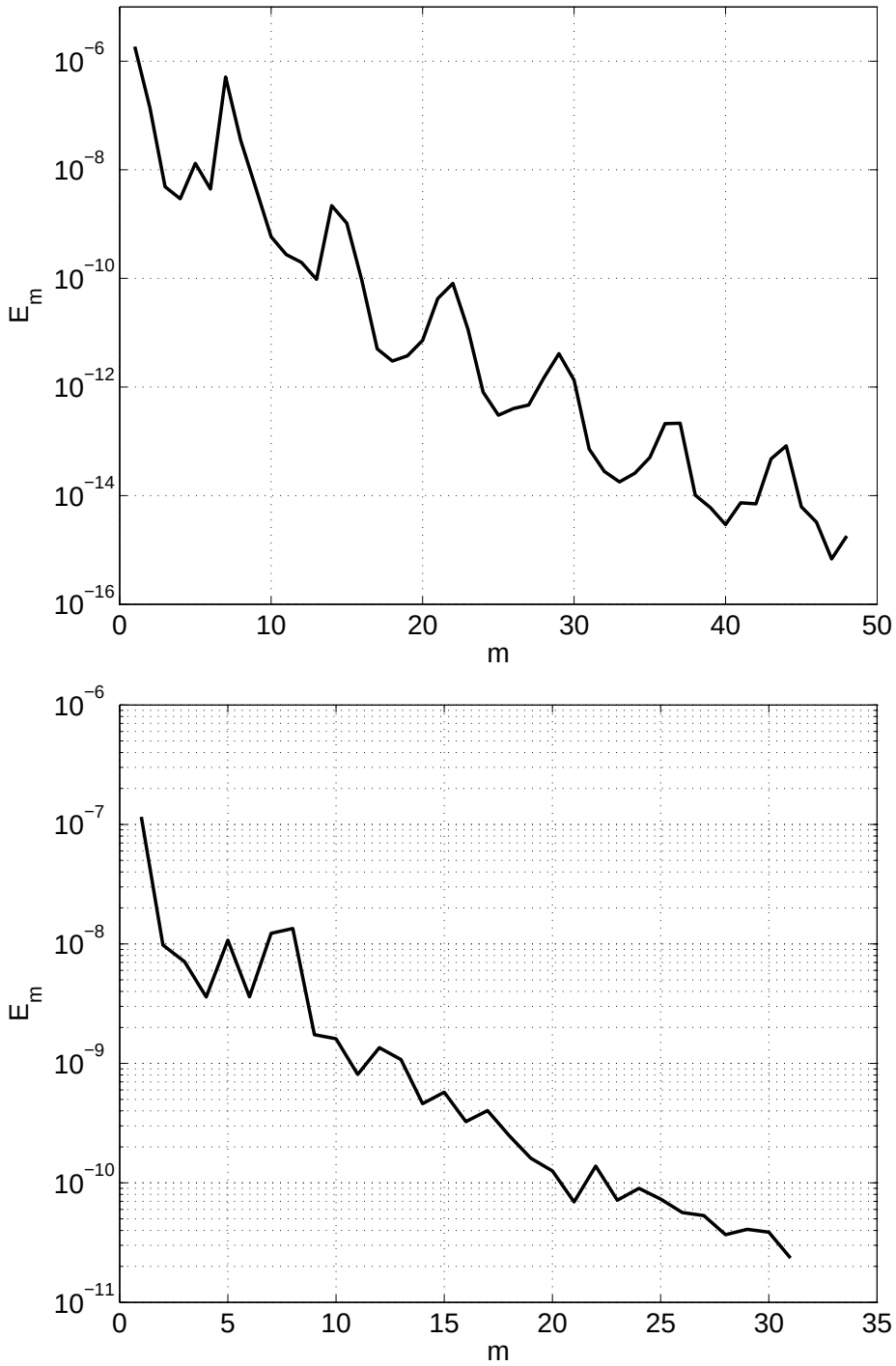

Figure 3.13: Spanwise energy spectrum at $t = 57$ (upper figure) and at $t = 177$ (lower figure) of the simulation at $Re = 185$ with spanwise periodicity $31.4d$. The energy of the m-th mode is defined as: $(\int_D \|\mathbf{v}_m\|^2 \, r dr \, dz)/2D$ where D is the surface of the streamwise - transverse computational domain.

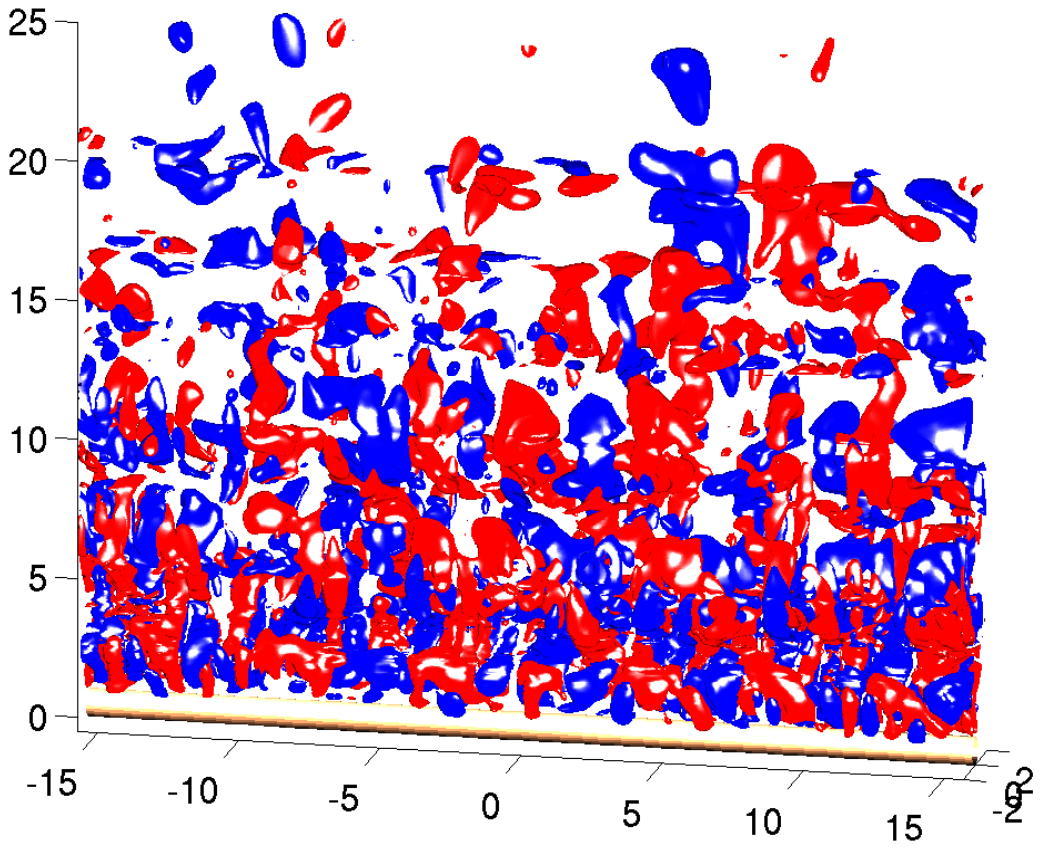

Figure 3.14: Spanwise velocity iso-surfaces at the levels of ±9% of inflow velocity of the solution with spanwise period $31.4d$ at $Re = 185$ at $t = 177$.

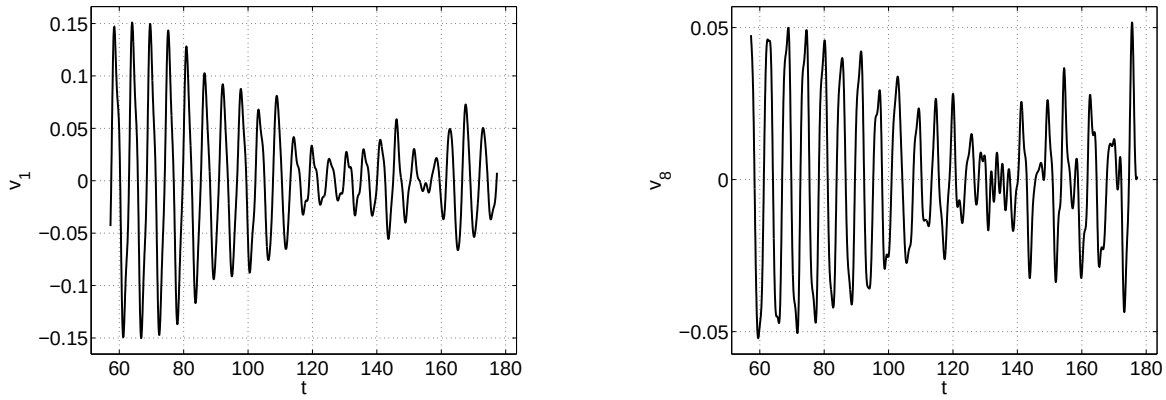

Figure 3.15: Time evolution of the mode 1 ($\lambda = 31.4d$) - left figure - and of the mode 8 ($\lambda = 3.9d$) of the transverse velocity at the history point $x = 12.5, y = 0, z = 0 (Re = 185)$.

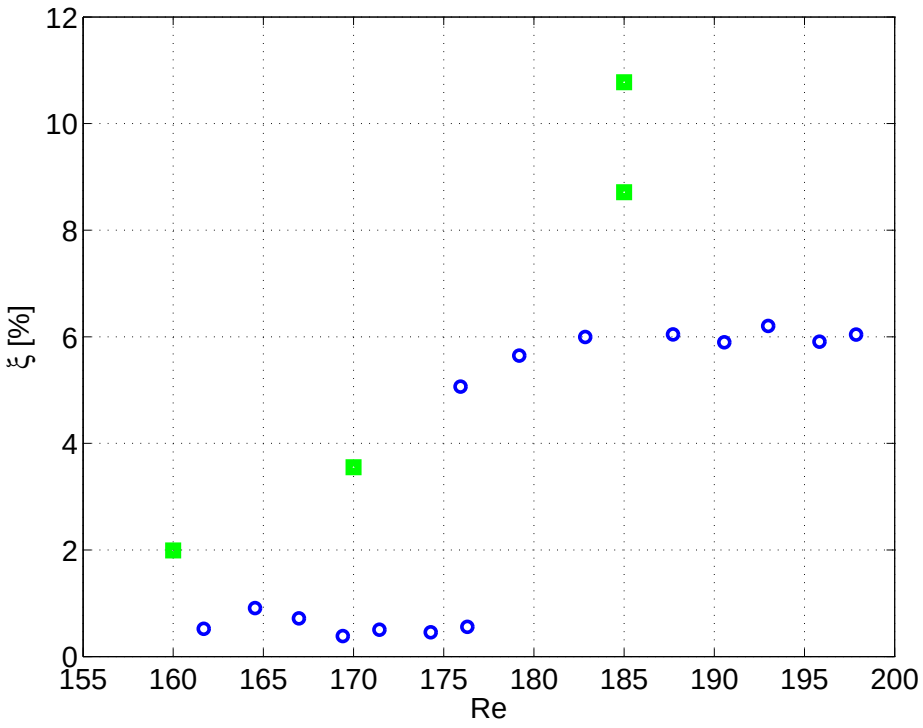

Figure 3.16: The same plot of shifts of the Strouhal number as in Fig. 3.11 but with, this time, Strouhal numbers obtained in simulations with the spanwise period $31d$ (green squares). (Two values at $Re = 185$: upper square $t \sim 60$, lower square $t \sim 170$ in the simulation at $Re = 185$ with spanwise periodicity $31.4d$.)

state.

The instantaneous 3D plot of the flow-field represented in terms of iso-surfaces of the spanwise velocity component in figure 3.18 is taken at the end of the interval in figure 3.17. The figure looks fairly chaotic but it must be recalled that the spanwise velocity component does not reflect the ordered parallel vortex shedding. If the transverse velocity is plotted the dominant vortex street clearly appears (see figure 3.19). The vortex shedding is essentially parallel with significant chaotic spanwise perturbations.

To the difference of the previous section, the spanwise spectrum in figure 3.20 has been obtained by averaging over the whole time interval represented in Fig. 3.17 because we believe that the regime is established and that the average has a physical relevance. The spectrum still contains a visible peak at $m = 7$, i.e. at a wavelength of $4.5d$ characteristic of the mode A, but is very smooth otherwise. The Strouhal number has been obtained both by inspecting the time behavior of the $m = 0$ mode and of local 3D velocity fluctuations at two points lying in the spanwise-streamwise symmetry plane ($y = 0$) at $x = 1.4$ and 12.5 d downstream of the cylinder axis (see Fig. 3.21). The found Strouhal number value is $St = 0.184$. This corresponds to a 4% drop as compared to the 2D case (filled square in figure 3.16 at $Re = 170$). This result is fairly well aligned with experimental data. As seen from Fig. 3.21, during a single vortex shedding period there may be a significant difference between the local and averaged spanwise velocity period. However, if all the nine periods represented are taken, the difference is of only 0.15%. Experimental spectra are obtained by fast Fourier transform of signals representing a large number of vortex shedding periods, over which the difference between a local and a spanwise averaged value is negligible.

3.6.3 Re=160

To find the lower bound for the hysteresis interval we ran a third simulation at $Re = 160$ taking the flow at $Re = 170$ as an initial condition. This time, the non zero Fourier modes decayed indicating the vanishing of all small scale three-dimensional structures. This decay of short scale 3D structures is accompanied by a renewal of a perfect periodicity of oscillations. However, unlike all modes $m \geq 2$, the largest scale $m = 1$ mode did not decay to zero. Instead, during the transient stage of the simulation, it 'absorbed' the energy of shorter scales. (See figure 3.22.) What happens is clearly seen in Fig. 3.23 where the transverse velocity 3D plot displays the shed vortices. The latter have become quite regular but are oblique. The flow does not revert spontaneously to parallel but rather to oblique vortex shedding. The obliqueness is limited by the largest available spanwise scale. It is to be expected that if the spanwise period is further increased the angle of the vortices will decrease.

The fact that oblique vortex shedding is also observed as stable, along with the parallel one (our method of linear stability analysis proves that the parallel vortex shedding is also linearly stable in this domain of Reynolds numbers), is not only in agreement with experiments with tori (where the unstable mode is a helocidal one - see Leweke & Provansal (1995)) but also with straight cylinders. E.g., the visualizations by Williamson (1989) show that the oblique vortex shedding respects the entire length of experimental cylinders. Moreover, the parallel vortex shedding spontaneously switches to the oblique mode as low as at $Re = 60$ unless cylinder ends are manipulated. The Strouhal number was found 2% below the 2D St

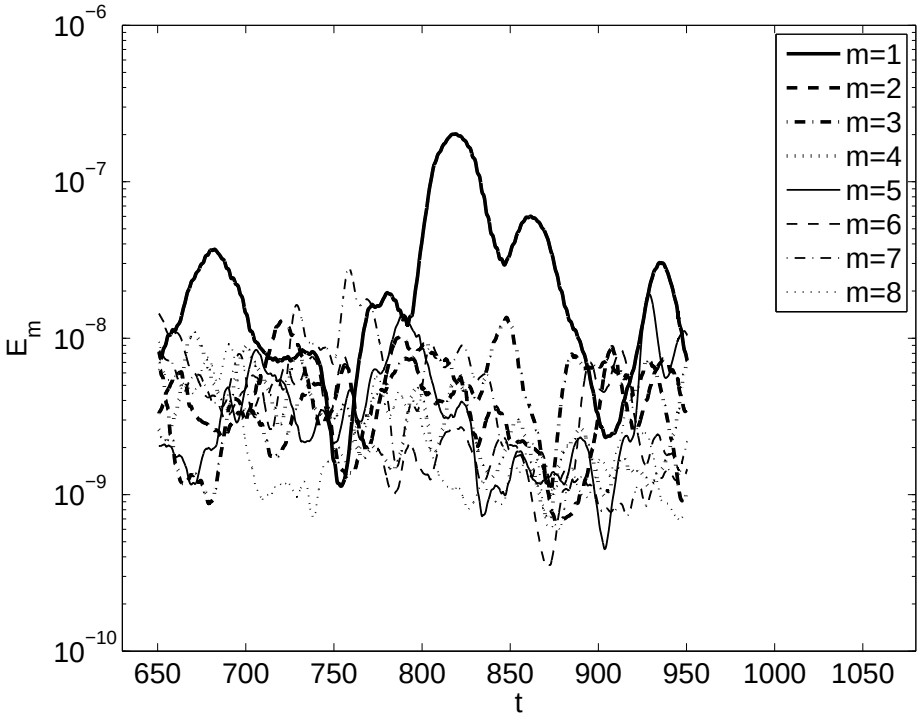

Figure 3.17: Time evolution of energy of modes ($(\int_D \|\mathbf{v}_m\|^2 \, r dr \, dz)/2A$ - A area of the radial-axial domain) of the established solution at $Re = 170$.

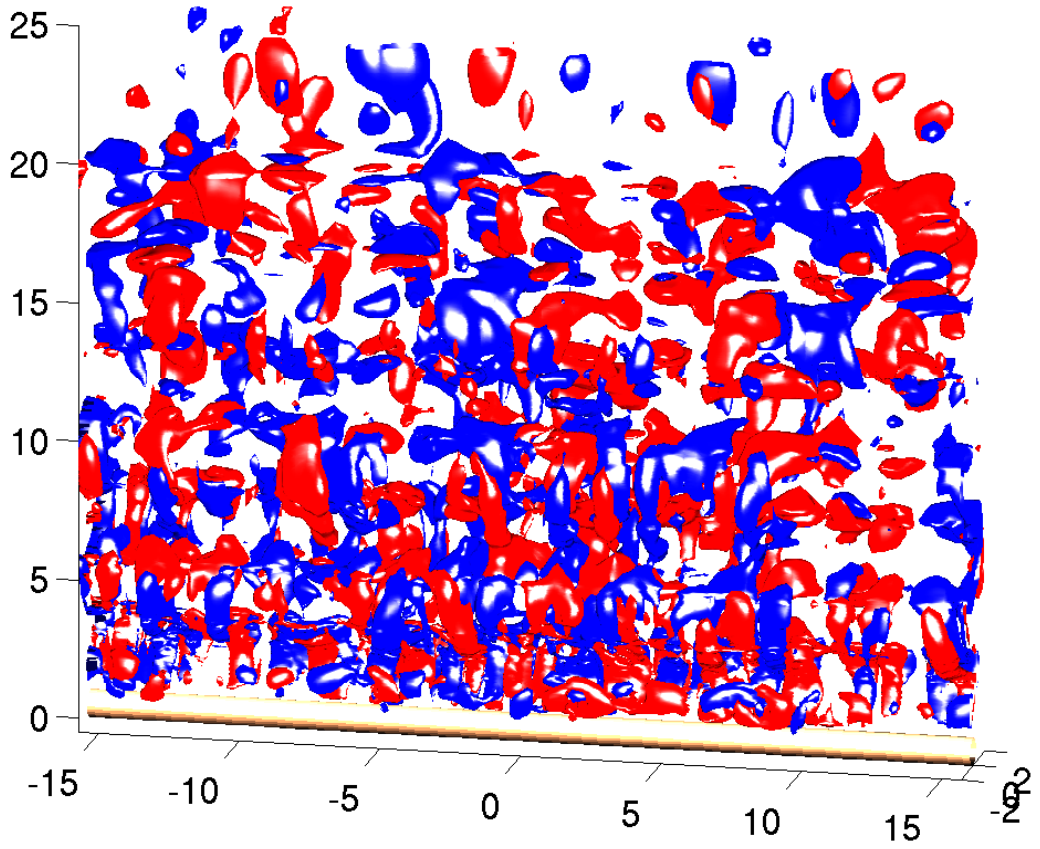

Figure 3.18: Iso-surfaces of spanwise velocity at ± 7 % of inflow velocity at $Re = 170$ at the end of the simulation interval in figure 3.17.

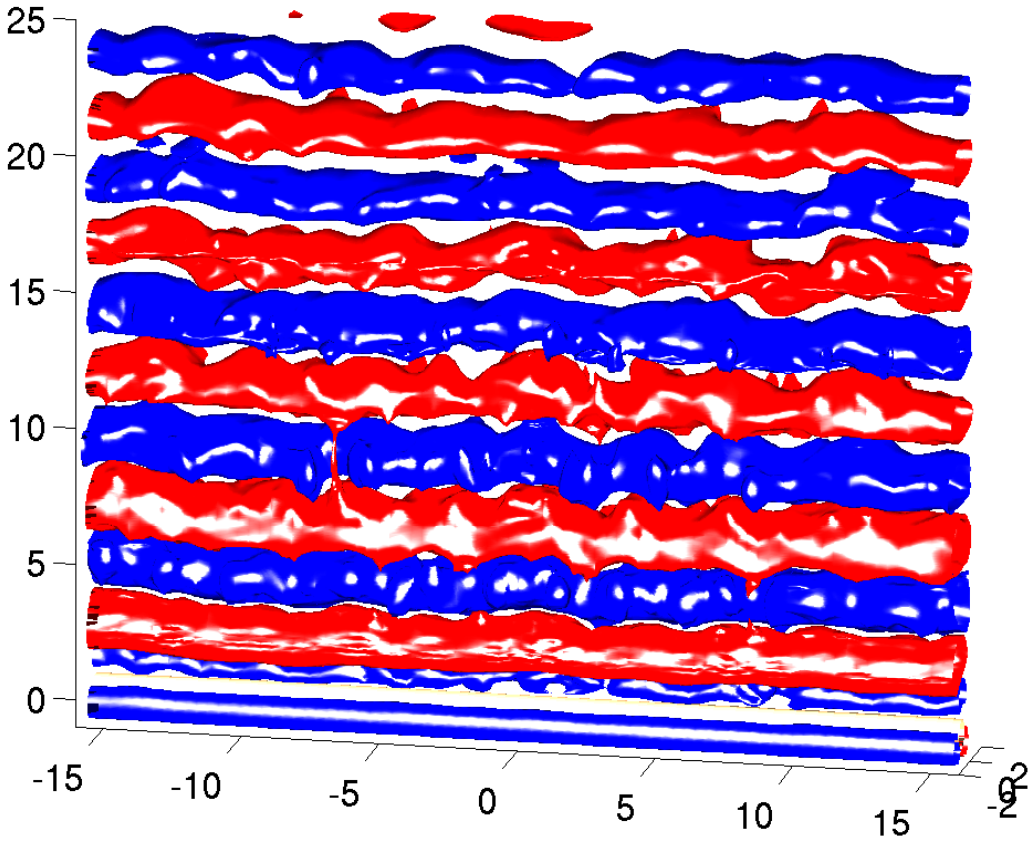

Figure 3.19: Iso-surfaces of transverse velocity at level corresponding to ±0.2 of inflow velocity at the end of the simulation interval in figure 3.17.

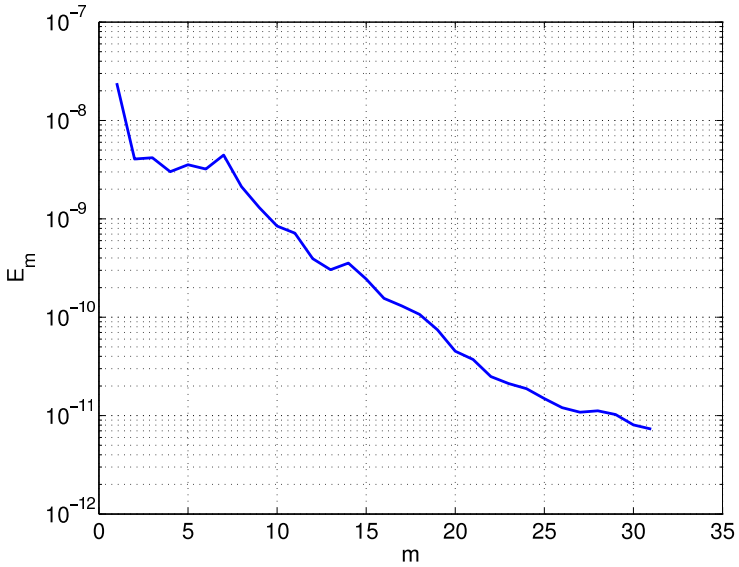

Figure 3.20: Spanwise energy spectrum obtained by averaging over the simulation interval of figure 3.17.

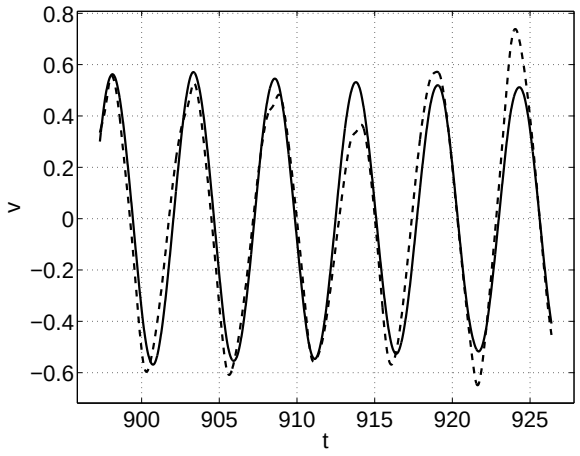

Figure 3.21: Time evolution of the transverse component of the $m = 0$ Fourier mode of the simulation with spanwise periodicity $31.4d$ at $Re = 170$ and at the point ($x = 1.4d$, $y = 0$) (full line) and time evolution of the local value of the same component at $x = 1.4d$, $y = 0, z = 0$.

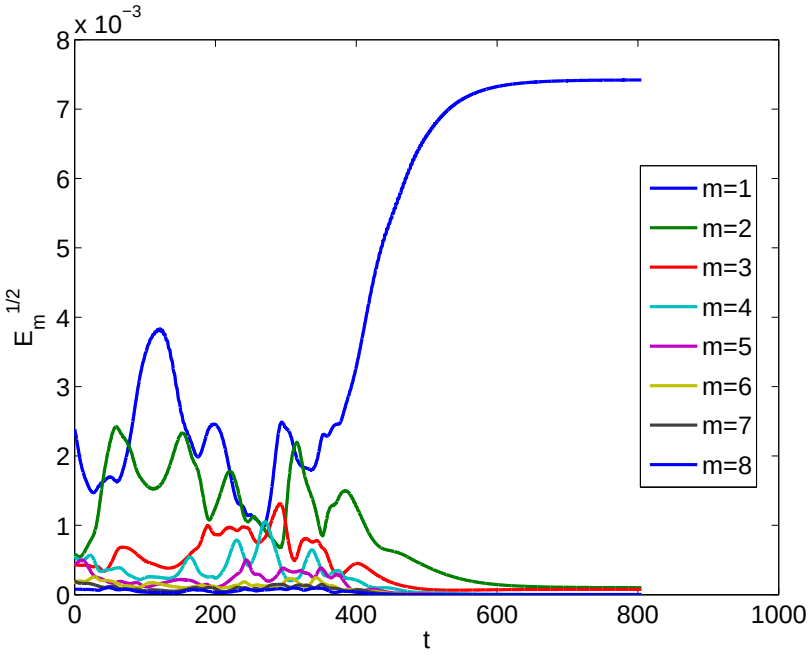

Figure 3.22: Decay of square roots of energies of modes $m > 1$ and increase of energy of mode $m = 1$ at $Re = 160$ starting from the state at $Re = 170$.

vs. Re curve. Taking account of the vortex shedding wavelength visible in figure 3.23 ($5d$) we can estimate the angle of obliqueness by 5/31.4 which yields a cosine of 0.987 predicting, according to Williamson (1989), rather just a 1.3% lower Strouhal number than in 2D. The difference is outside the error interval of the computation (the flow is now perfectly periodic and devoid of small structures) and is likely to correspond to a real fact.

3.7 Coexistence of mode A and mode B

As mentioned in chapter 1, there remains a controversy as far as the onset of the mode B is concerned in the bibliography. In spite of the speculative paper by Barkley *et al.* (2000) nobody evidenced a separate bifurcation giving rise to this mode. In view of the strong non-linear effects at the onset of mode A evidenced in this chapter it is plausible that the mode A is so strong at its very onset that it immediately excites the mode B. As a consequence, no extra bifurcation would be needed to explain its existence. The threshold for its experimental observation is then rather determined by the level of experimental noise and the relative ratio of amplitudes of both modes necessary to make the mode B observable. A definite answer to this question would be provided if we evidence the mode B in the three-dimensional flow simulated at the lowest Reynolds number of its existence, i.e. at $Re = 170$. This is what is attempted in the present section.

The qualitative discrimination of the modes A and B is usually based on their different spanwise wavelengths (see the paper of Williamson (1988*b*)). If one mode dominates the other this is a fairly sufficient criterion, however, assuming both modes might co-exist with comparable amplitude it is necessary to make the difference between the fourth spanwise harmonic of mode A and the mode B itself. It is to be recalled at this place that the observed (see Williamson, 1996*b*) ratio of wavelengths of the modes is very close to 4. The morphology of modes A and B was discussed by Leweke & Williamson (1998). The modes appear to have an opposite symmetry. Viewed as they appear in experimental visualizations, the streamwise vortices represent braids between the principal vortices parallel to the cylinder axis. The mode A braids have opposite signs at two subsequent half-periods of vortex shedding while those of mode B have the same sign. The unsteady periodic flow has, as such, no symmetry because of the anti-symmetric (with respect to the streamwise – spanwise plane) vortex shedding superimposed to the symmetric mean flow. The symmetries can, however, be investigated with accuracy using a time Fourier decomposition of the unsteady flow as suggested by Dušek (1996).

In this section, we analyze simulations of the cylinder wake for the spanwise periodicity $4d$ at $Re = 185$, to investigate the morphology of the pure mode A. To see how mode B progressively prevails in the presence of mode A we considered higher Reynolds numbers $Re = 190$, $Re = 215$ and $Re = 250$. At $Re = 270$ we study the morphology of the pure mode B while eliminating fully the mode A by imposing a very short spanwise period of $0.8d$. Finally we analyze the simulation at the subcritical Reynolds number value of 170 described already in Sec. 3.6.

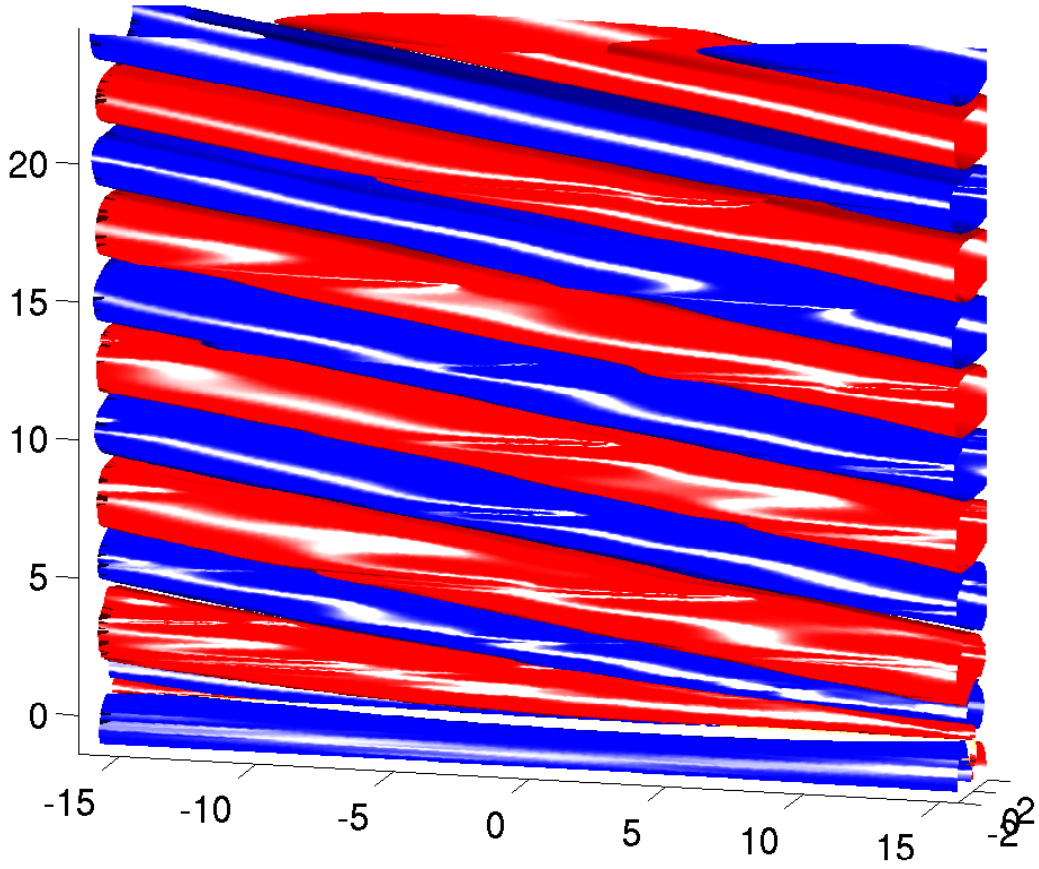

Figure 3.23: Transverse velocity iso-surfaces at levels of $\pm 10\%$ of inflow velocity of the solution with spanwise period $31.4d$ at $Re = 160$.

3.7.1 Pure modes A and B

The modes A and B were first investigated by Barkley & Henderson (1996) as linear unstable modes of the 2D flow by Floquet analysis. Linear analysis of the $2D$ base flow shows that the thresholds of modes A and B are very far from each other. In a fully non-linear simulation, even with a spanwise periodicity restricted to that of the mode A, the simultaneous excitation of the mode B cannot be excluded even at Reynolds numbers below the threshold determined by the linear analysis of a 2D flow. Indeed, the critical Reynolds number of the mode B is much higher (259) than that at which it is observed experimentally. It is easy to isolate the pure B-mode by restricting the spanwise periodicity to that of the preferred B-mode spanwise wavelength (0.82 d) along the lines presented by Henderson (1997). The short spanwise wavelength inhibits the mode A. In a non-linear simulation of the mode A, the mode B can appear, due to its about four times shorter wavelength, as part of the fourth spanwise harmonic. However, close to the onset of the three-dimensionality (at Reynolds numbers below 190) the B mode has never been observed in simulations with spanwise periodicity of the mode A. As a consequence a non-linear simulation with a spanwise period λ_{lin} (that of the linear preferred mode A) at a low Reynolds number can be expected to provide a practically pure A mode.

The transition from a mode A dominated flow to a mode B dominated flow can be simulated even with the short spanwise period corresponding to the most amplified spanwise wavelengths as seen in figure 3.24. At $Re = 190$, the iso-surfaces of spanwise velocity represented in the left figure 3.24 show a practically pure mode A. No small scale spanwise structures are present. At $Re = 250$ the flow is already highly chaotic. As can be seen, it is dominated by structures of much shorter spanwise length (with 4 spanwise periods on a single period of the mode A at the same regime). The A-mode just slightly modulates the B-mode in the close wake. However, it still dominates in the far wake. At a Reynolds number as close to the threshold of A-mode as $Re = 215$ the mode B is already visible (small blobs close to the middle of the cylindrical section and fine filaments in the right of the plot). Because the mode B appears as an exact $4th$ spanwise harmonic of the A-mode it can be assumed that it is excited by non-linearities since the very threshold of the onset of the A-mode but, that at low Reynolds number, it is only weak and difficult to detect.

We have seen that (even with a spanwise period λ_{lin}) the non-linear A-mode presents a subcritical bifurcation. A non-linear subcritical three-dimensional state was reported already by Henderson & Barkley (1996) at $Re = 185$ with this spanwise periodicity. The instantaneous flow obtained by the simulation at this Reynolds number is presented in figure. 3.25. The two plots represent the streamwise vorticity ω_x (which is zero in a 2D wake) of mode A. The mode B is represented in Fig. 3.26. The view of these, as well as that of following figures of this section, is taken along the cylinder axis. Figs. 3.25 and 3.26 are to be compared to the scheme of vortical structures by Leweke & Williamson (1998). The alternate orientation of braids of mode A means that vortical structures emitted to the left of the spanwise-streamwise symmetry plane have a sign opposite to that of structures emitted to right. The converse is true for the mode B. This is what is observed in Figs. 3.25 and 3.26.

Because of the alternate vortex shedding the instantaneous flow is no longer symmetric which complicates somewhat its spatial characterization. In a paper dealing with the periodic

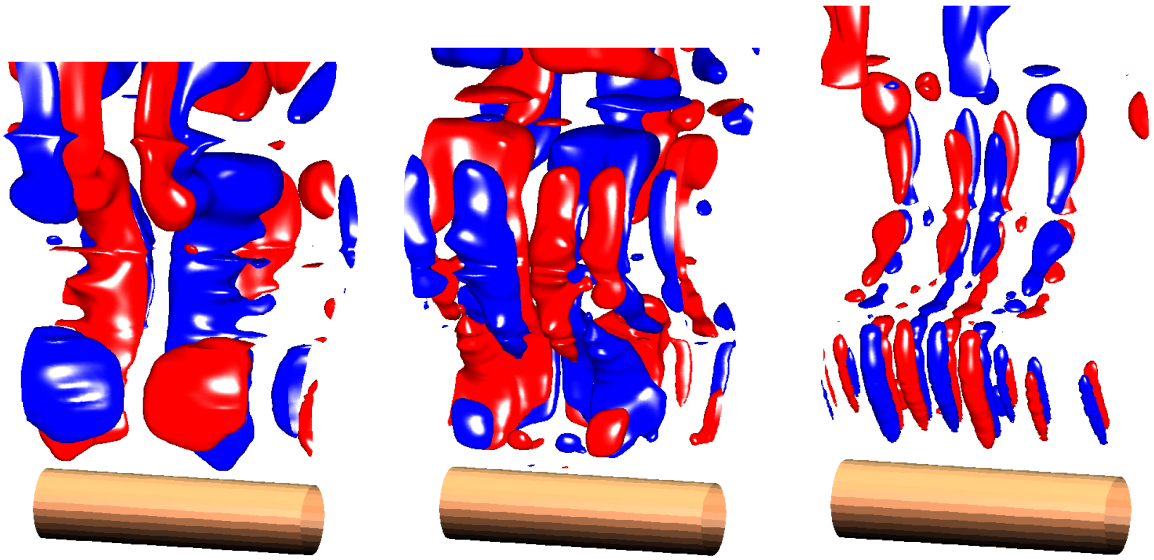

Figure 3.24: Wake structure represented by iso-surfaces of spanwise velocity at ±8% of inflow velocity at (from left to right) $Re = 190$, 215 and 250. The spanwise periods are $4.01, 3.93$ and $3.68d$, respectively.

2D cylinder wake (see Dušek, 1996)), it has been shown that the symmetries reappear if the time Fourier modes of the flow are computed. The simulations with spanwise periodicity $4d$ at Re=185 and $0.82d$ at $Re = 270$ yield both a saturated periodic state with a well defined period T ($T = 5.16$ and $4.8\ d/U_\infty$, respectively). If the time and spanwise Fourier decompositions are combined an oscillating quantity f is expressed as

$$\begin{aligned} f(x,y,z,t) &= \sum_{n=-\infty}^{\infty} f_n(x,y,z)\, e^{2i\pi nt/T} \\ f_n(x,y,z) &= \sum_{m=-\infty}^{\infty} f_{m,n}(x,y)\, e^{-2i\pi mz/\lambda} \end{aligned} \tag{3.4}$$

where λ stands for the spanwise and T for the time period. The time Fourier modes $f_{m,n}$ are computed over a period by integrating the spanwise Fourier-modes of the spatial discretization:

$$f_{m,n}(x,y) = \frac{1}{T}\int_0^T f_m(x,y,t)\, e^{-2i\pi nt/T}\, dt. \tag{3.5}$$

The essential part of the fluctuations is represented by the fundamental $n = 1$ mode $f_1(x,y,z)$. The real part of the fundamental time Fourier mode of the streamwise vorticity $\omega_{x,1}$ is represented in Fig. 3.27. The $n = 1$ Fourier mode is symmetric for the mode A and

antisymmetric for the mode B. This is in agreement with Figs. 3.25 taken with an exactly half a period delay, during which the structures advanced by half a wavelength upward. The figures are perfectly antisymmetric. I.e., at the same streamwise station, there appears an antisymmetric structure (with opposite sign) half a period later on the opposite side of the symmetry plane. Because, in time Fourier integration, half a period corresponds to a change of sign of the oscillations, the corresponding Fourier coefficient must have the same sign across the flow axis. The opposite holds again for the mode B: its fundamental Fourier harmonic is antisymmetric. The vorticity has a more complex spatial structure than the velocity field. Moreover, as a primitive variable, the velocity is better resolved. It is easy to see that the streamwise vorticity ω_x has the opposite symmetry to that of the streamwise (u) and spanwise (w) velocity components and has the same symmetry as the transverse (v) velocity component. The spanwise velocity component being zero in a 2D flow, in the same way as ω_x, it shares the advantage of providing a visualization of structures arising at the onset of three-dimensionality. The $n = 1$ time-Fourier mode of spanwise velocity is represented in Fig. 3.28. It is antisymmetric with respect to the streamwise-spanwise symmetry plane for the mode A and symmetric for the mode B. The spanwise Fourier modes ($n = 1, m$) introduced in Eqs. (3.4, 3.5) share the symmetry of the non decomposed mode.

The distinctive feature of modes A and B can thus be further simplified by investigating just the largely dominant fundamental azimuthal mode corresponding to the linear unstable mode in a linear analysis. Because it is a complex function of just two variables a 2D (complex) plot is sufficient. Finally, the issue being to distinguish between the transverse antisymmetry and symmetry, a transverse profile of either the real or imaginary part of the $n = 1, m = 1$ mode at any downstream station $x = const.$ is sufficient for this purpose. The transverse profile of the real part of the component $w_{1,1}$ of mode A (see Eqs. (3.4)) three diameters downstream of the cylinder axis is represented in figure. 3.29. Because, at equal Reynolds number, the spanwise wavelength of the mode B is four times smaller than that of the mode A it has to expected to appear roughly in spanwise scales corresponding to the fourth spanwise harmonic of the A-mode in a non-linear simulation. For this reason, the fourth spanwise harmonic of the mode A has been compared to the mode B in figure. 3.30. Both harmonics of the mode A are very accurately antisymmetric, which confirms that the mode B is absent in this simulation (at $Re = 185$ with spanwise periodicity $4d$).

3.7.2 Evidence of the presence of both A and B modes at $Re = 170$

In this section we present the results of the time Fourier analysis of the chaotic flow obtained at $Re = 170$ with a spanwise periodicity of about $32d$. The resulting instantaneous flow was represented in Figs. 3.18 and 3.19 in terms of spanwise and transverse velocity. The transverse velocity plot shows that the vortex shedding remains essentially parallel but the spanwise velocity plot reveals the highly chaotic character of the three-dimensional flow structures. Practically all spanwise scales are present and no obvious fingerprint of either the mode A or the mode B is clearly visible.

To evidence coherent structures in a chaotic flow some averaging is usually necessary. As explained in Sec. 3.7.1, we expect to detect the modes A and B by examining the aspect of the time Fourier mode obtained by integrating over one vortex shedding period. The latter

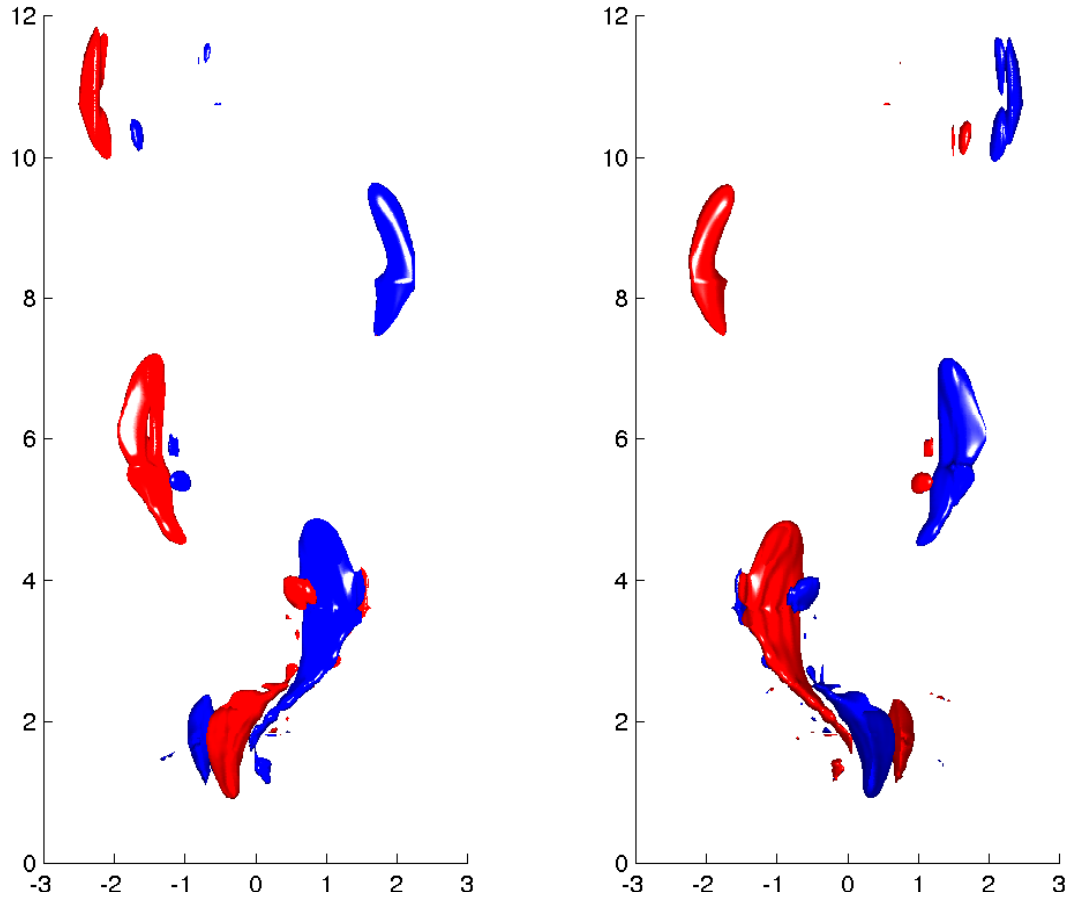

(a) (b)

Figure 3.25: Instantaneous visualization of mode A represented in terms of iso-surfaces of streamwise vorticity at $\pm$ 20% of its maximum obtained at $Re = 185$ with a streamwise periodicity of $4d$. Fig. b) is taken half a period later that Fig. a).

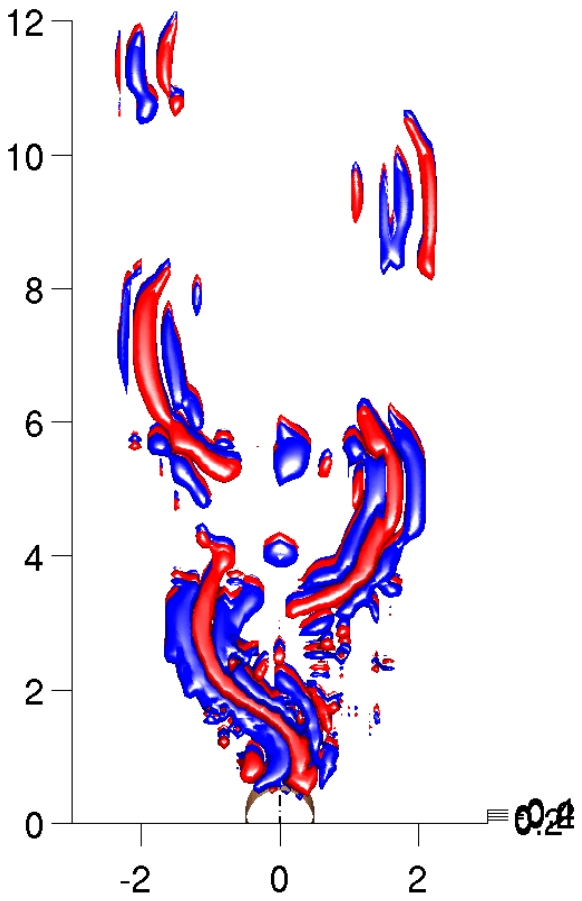

Figure 3.26: Instantaneous visualization of mode B represented in terms of iso-surfaces of streamwise vorticity at $\pm$ 2% of its maximum obtained at $Re = 270$ with a spanwise periodicity of $0.82d$.

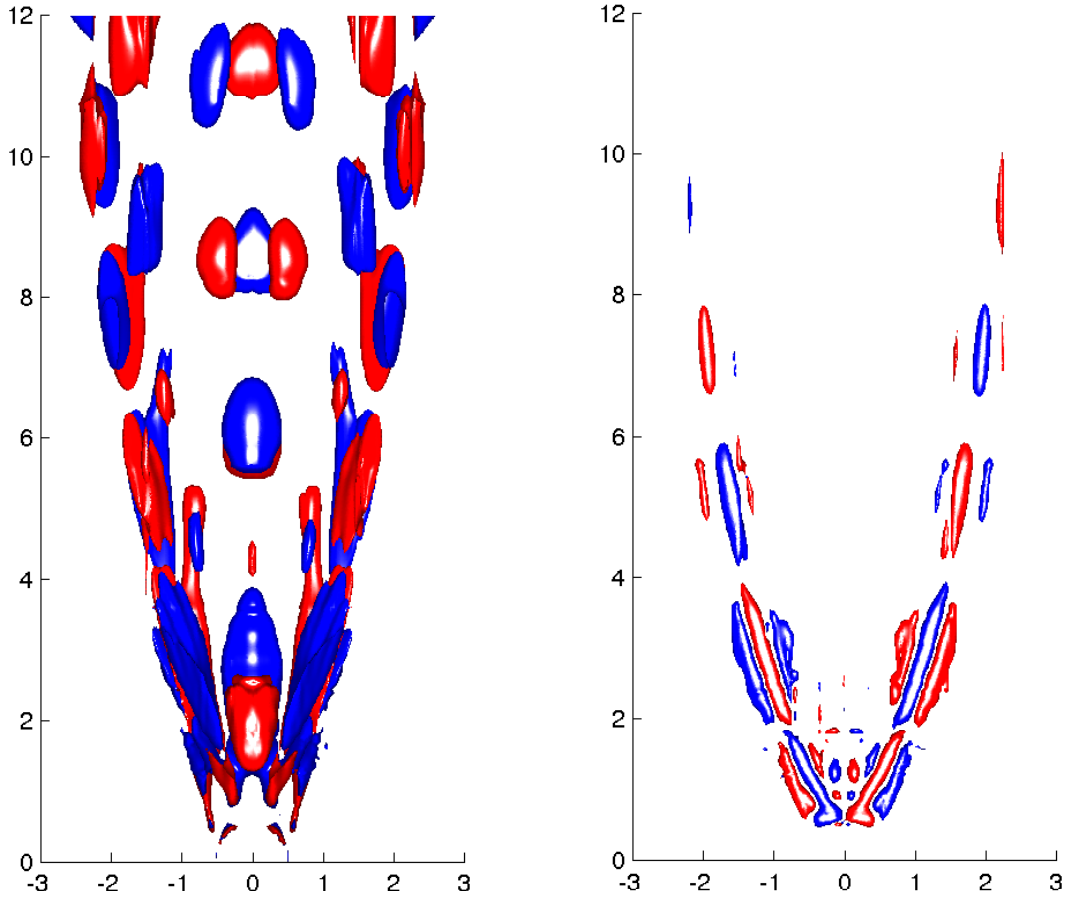

(a) (b)

Figure 3.27: The real part of the fundamental time mode Fourier of the streamwise vorticity obtained over one period of oscillation of mode A at $Re = 185$ (a) and of mode B at $Re = 270$ (b). The levels of iso-surfaces in (a) are taken at $\pm$ 13% and, in (b), at $\pm$ 5% of the maximum. The period of integration of the modes A and B is 5.16 and 4.8 d/U_∞, respectively.

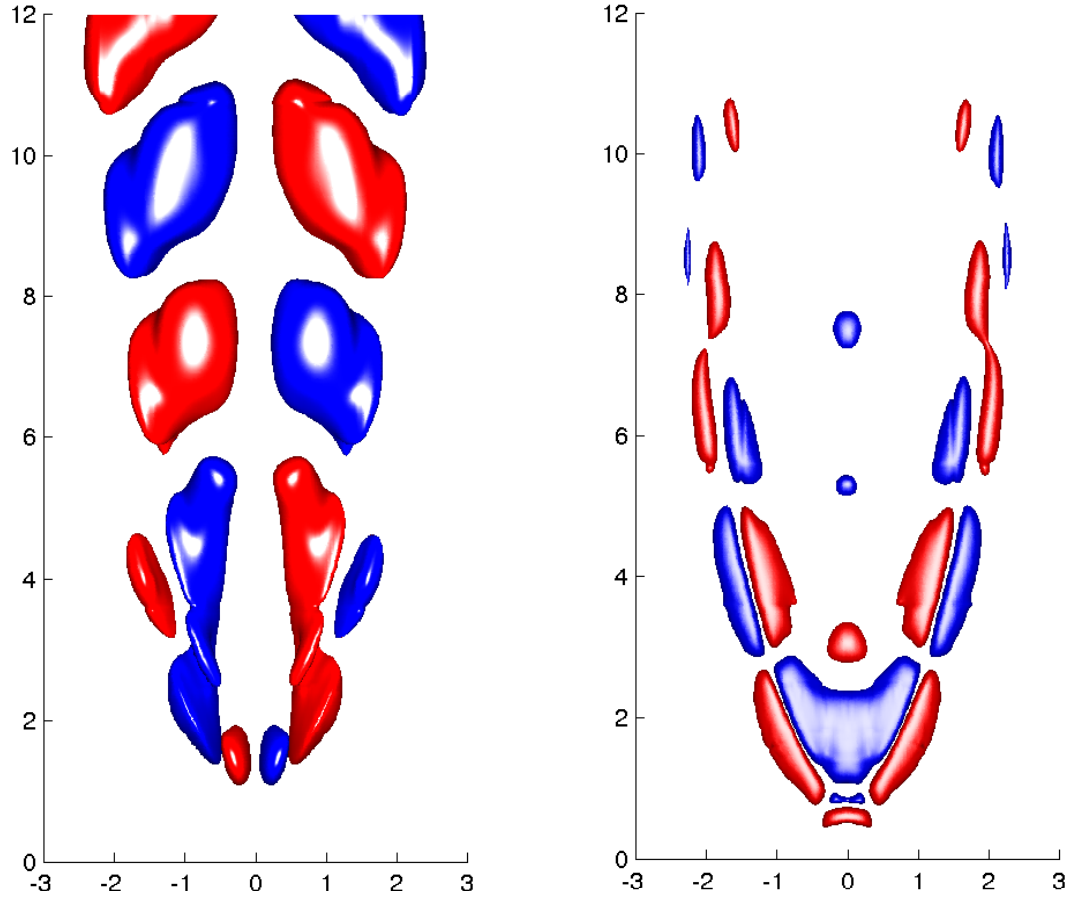

(a) (b)

Figure 3.28: The real part of the fundamental time Fourier mode of spanwise velocity obtained over one period of oscillation of mode A (at $Re = 185$, $\lambda = 4d$) (a) and of mode B (at $Re = 270$, $\lambda = 0.82d$) (b). The levels of iso-surfaces in (a) are taken at $\pm$ 30% and, in (b), at $\pm$ 10% of the maximum.

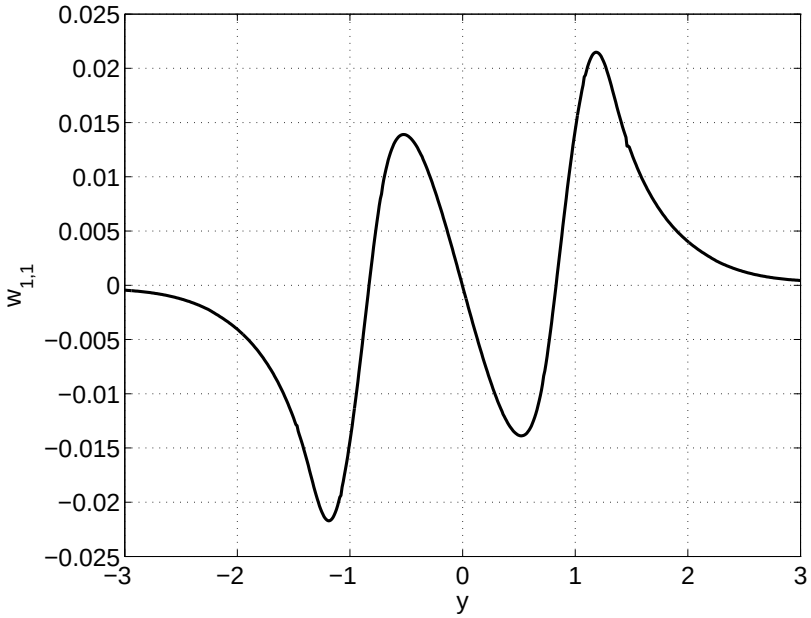

Figure 3.29: Transverse profile at $x = 3d$ of the real part of mode $w_{1,1}$ (fundamental time and spanwise mode of mode A) computed for the Reynolds number 185.

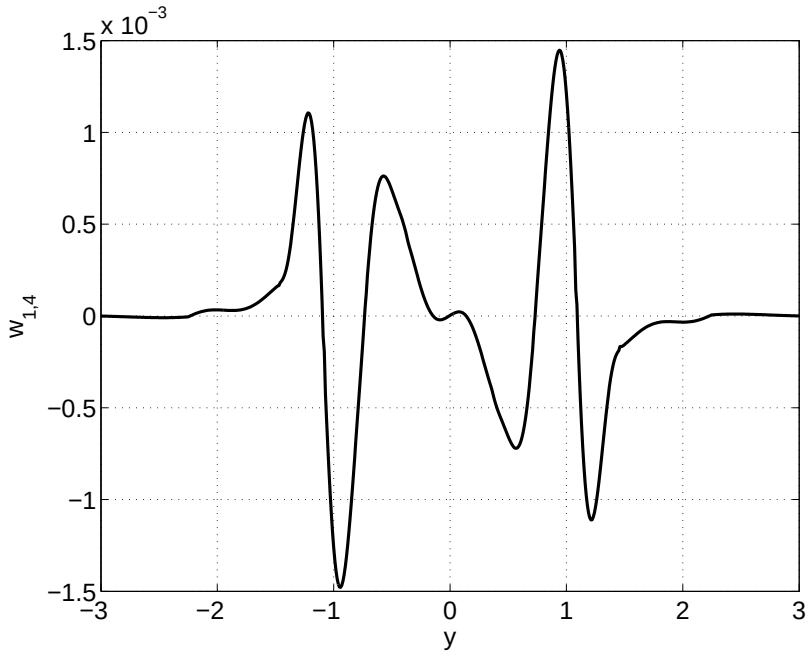

(a)

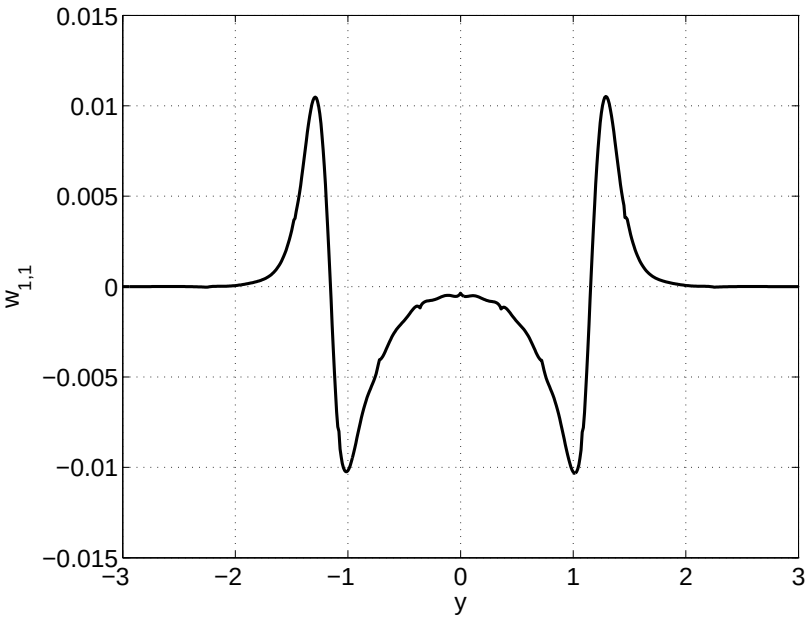

(c)

Figure 3.30: (a) Transverse profile at $x = 3d$ of the real parts of $w_{1,4}$ of mode A computed with spanwise period $4d$ (4-th spanwise harmonic) at $Re = 185$. (b) Transverse profile of $w_{1,1}$ of mode B of a computation at $Re = 270$ with spanwise period $0.82d$ (i.e. at a period corresponding to the fourth harmonic of mode A at the same Reynolds number).

remains still very well defined because of the dominant parallel vortex shedding which is very close to periodic even in a chaotic flow. The period was found to correspond to a Strouhal number of 0.184 (period of 5.43 d/U_∞) which is in a good agreement with the subcritical branch of the Williamson's curve (Williamson (1996a)) . To smooth the chaotic fluctuations, the time Fourier mode corresponding to one vortex shedding period was averaged over 25 periods. In Sec. 3.7.1 we have shown that the symmetry of transverse profiles of the spanwise Fourier component at the length scale corresponding to the spanwise period of the B-mode can be expected to carry the fingerprint of the symmetry of this mode. If both modes are present the corresponding time-spanwise Fourier component of the spanwise velocity will be neither antisymmetric nor symmetric. Figure 3.31 shows the transverse profile of the fundamental time-Fourier mode and of the 28-th spanwise Fourier mode ($n = 1, m = 28$ in the sense of expansion (3.4)) of the spanwise velocity component. The period of the spanwise expansion being 10 π, the wavelength of this mode is thus 1.1d. The longer wavelength (1.1d instead of 0.8d) can be explained by the significantly lower Reynolds number ($Re = 170$ as compared to $Re = 260$ for which the linear analysis is available). It is clearly seen that the profile has neither of the symmetries. I.e. both modes A and B are present, the mode B being predominant at this station and for this mode (see also the figure 3.30). If all spanwise modes are inspected, their common feature is the absence of exact symmetry. Modes close to the A-mode wavelength (m=6, 7 and 8) are very close to being antisymmetric (the mode A is dominant at this scale). The neighboring modes ($m = 26, 27, 29, 30$) to that represented in Fig. 3.31 are quite far from either the symmetry or antisymmetry. The mode $m = 28$ is very clearly closest to be symmetric.

The simultaneous presence of both modes A and B in the chaotic flow at $Re = 170$ can thus be demonstrated in a still more convincing manner by extracting the antisymmetric and the symmetric part of the fully re-composed first Fourier harmonic of the spanwise velocity w_1 the oblique view of which is represented in Fig. 3.32:

$$\begin{aligned} w_{1,A}(x,y,z) &= (w_1(x,y,z) - w_1(x,-y,z))/2; \\ w_{1,S}(x,y,z) &= (w_1(x,y,z) + w_1(x,-y,z))/2. \end{aligned} \tag{3.6}$$

To evidence the spanwise scales we take views perpendicular to the cylinder axis (Fig. 3.33). As such, the mode w_1 contains both small and large scales. No symmetry is obvious in the plane perpendicular to the cylinder axis. However, if the axisymmetric and symmetric parts defined by Eq. (3.6) are represented separately, only large spanwise scales are filtered in figure 3.34 and small scales are obtained in figure 3.35. In figure 3.34 it's rather a period of 10d that appears to dominate but it is not surprising because the mode A peak in the spanwise spectrum in figure 3.20 is dominated by larger wavelengths. It can be said, that the structures of the mode A are considerably affected by large scales. On the contrary, the symmetric part represented in figure 3.35 has a fairly well defined spanwise wavelength of about 1d corresponding to the mode B. Finally, the view of the symmetric part taken along the cylinder axis (Fig. 3.36) presents a similarity with figure 3.28 b). All the presented figures clearly demonstrate the presence of the mode B as low as at $Re = 170$.

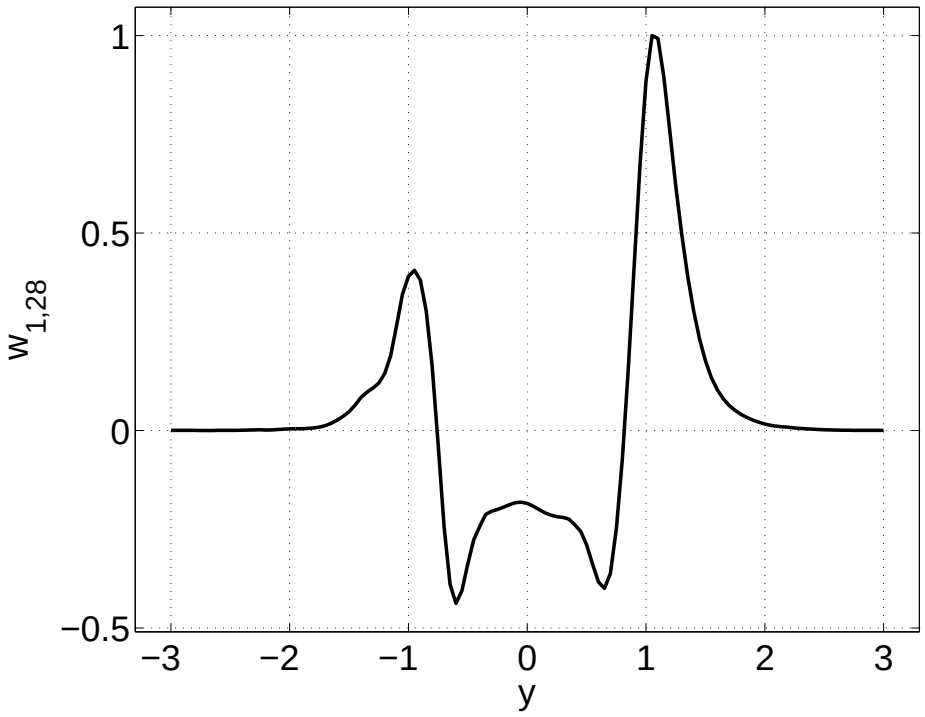

Figure 3.31: Transverse profile of the real part of the time-spanwise Fourier mode $n = 1, m = 28$ of the spanwise velocity 3 diameters downstream of the cylinder.

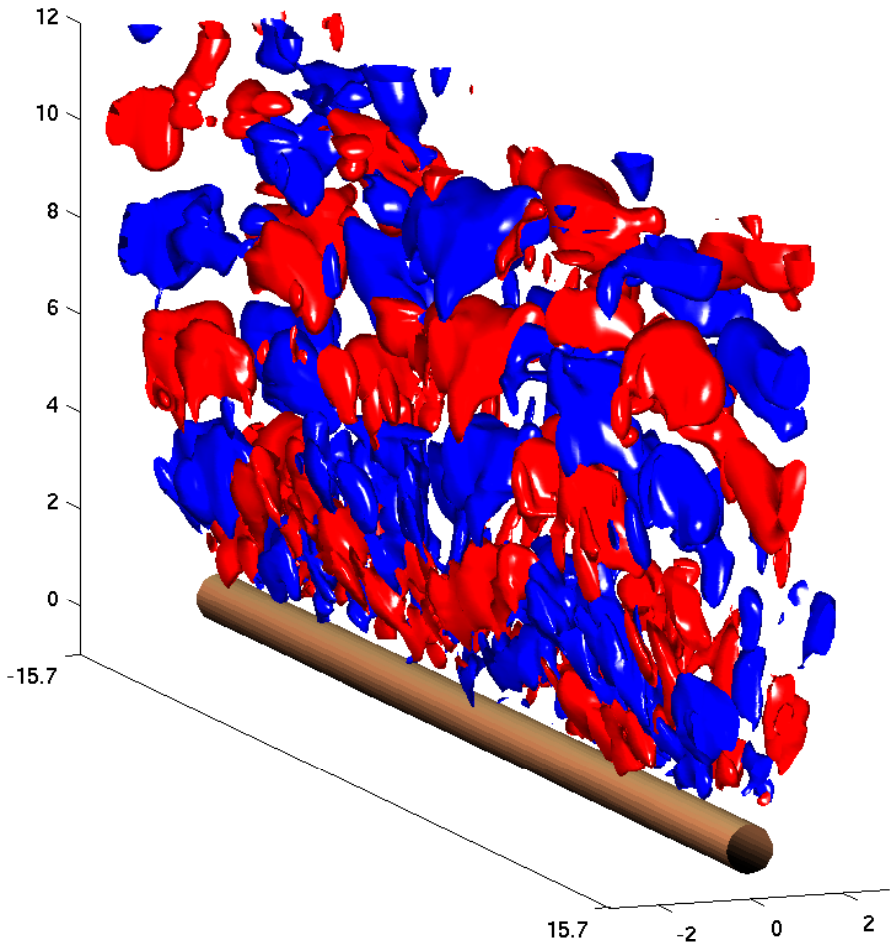

Figure 3.32: Iso-velocity surfaces of the real part of the first time-Fourier harmonic of spanwise velocity at levels ± 0.15 of the inflow velocity.

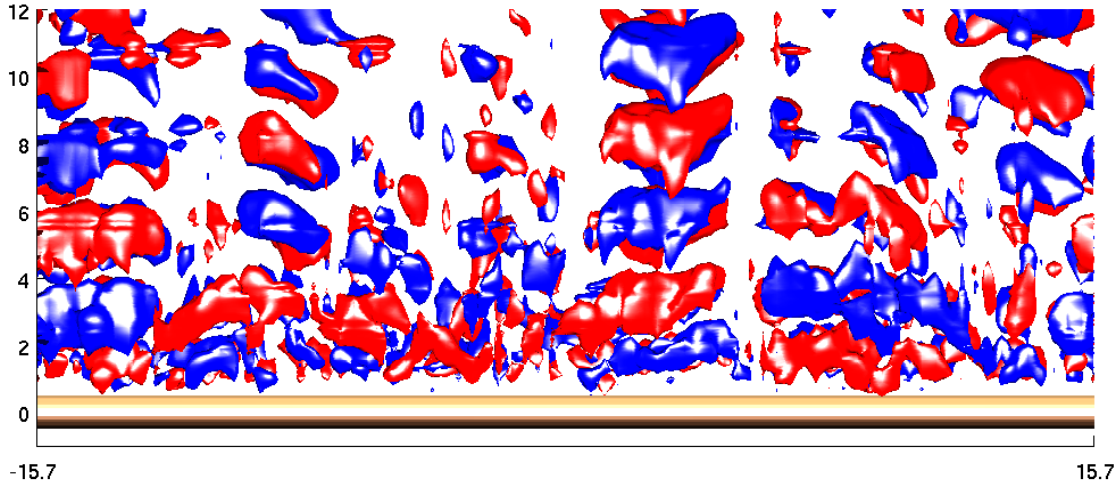

Figure 3.33: Same as Fig. 3.33 but view perpendicular to the cylinder axis.

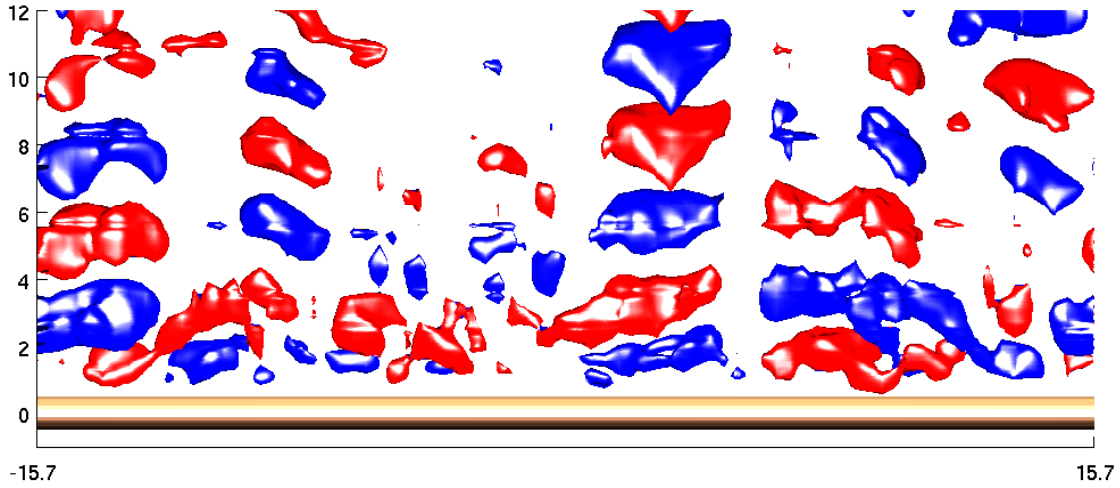

Figure 3.34: The axisymmetric part $w_{1,A}$ of the fundamental time Fourier mode of the spanwise velocity represented in the same way as in Fig. 3.33.

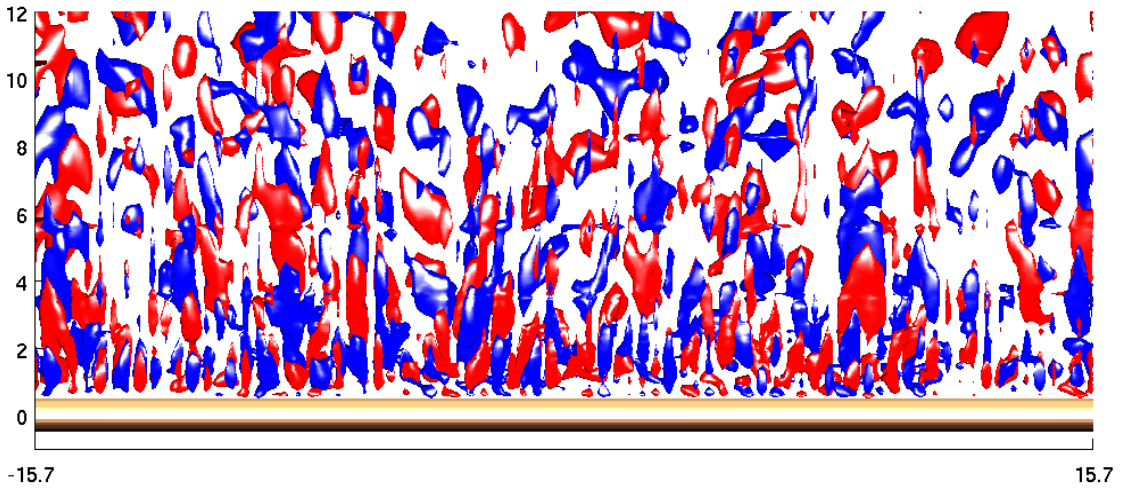

Figure 3.35: The symmetric part $w_{1,A}$ of the fundamental time Fourier mode of the spanwise velocity represented in terms of iso-surfaces of its real part at level corresponding to ± 0.05 of inflow velocity.

3.8 Conclusion of the chapter

The purpose of the chapter was to show that, in spite of the fact that the onset of three-dimensionality in the infinite circular cylinder wake disappeared from the spot-light of research for many years, the subject was still far from being totally explored. The subcritical nature of the bifurcation giving rise to the three-dimensionality strongly limits the predictivity of linear results that have been mostly presented so far in literature and that have strongly biased the fully non-linear simulation effort. As a result, an objective assessment of available experimental results and of existing numerical and theoretical bibliography lead to the conclusion that there was no quantitative agreement between numerical simulations and experiments. The presented chapter allowed us to elucidate the following major points:

1. The linear preferred spanwise wavelength is not indicative of the physically relevant spanwise periodicity to be chosen for a fully non-linear simulation neither AT nor BELOW the bifurcation threshold.

2. There is no physical cut off of large spanwise scale and the latter absorb the major part of the fluctuation energy.

3. The presence of large spanwise scales accounts not only for a chaotic nature of the flow but determines also the subcritical bi-stability interval between the three-dimensional flow and parallel vortex shedding.

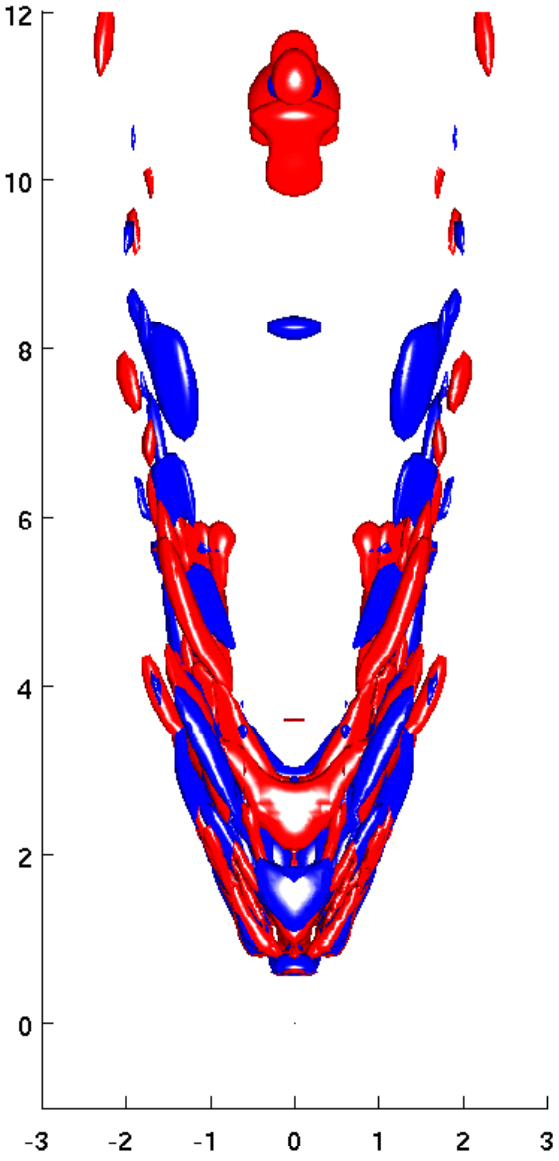

Figure 3.36: Same as Fig. 3.35 but view parallel to the cylinder axis and the iso-surface levels are taken at ± 0.1 of inflow velocity.

4. If sufficiently large spanwise scales are accounted for in a numerical simulation the lower limit of the bi-stability interval can be brought close to that observed in experiments i.e. at about $Re = 170$.

5. The presence of the pure mode A in the flow tends to overestimate the Strouhal number drop of the three-dimensional wake as compared to the parallel vortex shedding. The spatial and temporal chaos caused by large spanwise flow structures partially un-couples the 3D structures from the parallel vortices and brings the mean Strouhal number drop close to experimental observations.

6. There is no separate bifurcation giving rise to the mode B. The latter is excited by strong non-linearities present even under the bifurcation threshold yielding the mode A and was evidenced at the smallest Reynolds number at which the chaotic three-dimensional wake was stable. This explains why no clear cut threshold of mode B could be evidenced. The fact that the observation of mode B in experiments has not been reported below $Re = 230$ is to be attributed to experimental noise.

The enumerated results show that it is still possible to obtain a very realistic numerical simulation of the flow past a very long straight cylinder. They relativize, however, the physical relevance of the 'infinite geometry'. The latter does not significantly simplify simulations while many practical applications are characterized with aspect ratios smaller than or comparable to the ratio of the spanwise period and of the cylinder diameter required for capturing sufficiently large spanwise structures.

Chapter 4

Transition to three-dimensionality in the wake of a NACA 0012 airfoil

4.1 Scope of the investigation

The choice of the NACA 0012 airfoil was given by the available bibliography summed up in chapter 1. It shows, that NACA 0012 is by far the best investigated wing profile. The NACA 0012 airfoil represented in figure 4.1 is a symmetrically shaped airfoil, where 00 means no camber, having a maximum thickness 12 % of the chord length.

The bibliographic overview shows also that, in spite of the large quantity of experimental and numerical data a systematic investigation of the flow past this profile at low Reynolds numbers is missing. This can easily be understood because practically relevant regimes are characterized by several orders of magnitude higher Reynolds numbers. However, turbulence modeling of detached flows past airfoils appears to be unreliable and numerical investigations exploit more and more frequently large computing resources for large eddy and even direct numerical simulations. In this case, it is of interest to investigate first the lowest stages of the onset to turbulence because the latter may provide a relatively cheap information on relevant spatial and temporal scales governing the turbulent flow dynamics. As shown in the previous chapter such an information may be valuable for designing physically relevant numerical configurations.

In the same way as an infinite circular cylinder, the airfoils are considered as infinite cylindrical bodies with an optimized aerodynamic cross-section. In this chapter we apply to them the same approach of investigation as to circular cylinders. This approach consists in determining the thresholds of flow separation, of the onset of unsteadiness and of the onset of three-dimensionality. In view of the new results of chapter 3, an investigation of non-linear effects will also be attempted.

In comparison with the circular cylinder, the investigation of the flow past airfoils presents enhanced difficulties of simulation of boundary layers requiring globally heavier meshing, necessitates higher Reynolds numbers (even if the latter is based on the effective cross section rather than on the chord of the airfoil) to simulate the transition to turbulence and involves two parameters: the angle of incidence and the Reynolds number. As a consequence, the

required computing resources are much larger and the number of individual runs is much higher. To keep the latter within reasonable limits, we decided to limit the Reynolds number range to less or equal to 10^4. The Reynolds number is defined in agreement with prevailing bibliography as

$$Re = \frac{U_\infty c}{\nu} \tag{4.1}$$

where U_∞ and ν are, as before, the asymptotic flow velocity and kinematic viscosity, respectively and where, independently of the angle of incidence, c, the chord length, is taken as a relevant length scale. As for the angle of incidences, the investigation is limited to angles increasing from 0 to 12 degrees because beyond 12 degrees the flow is fully detached even at relatively moderate Reynolds numbers and the airfoil looses all of its aerodynamic specificity.

4.2 Geometry and numerical implementation

4.2.1 Three-dimensional computational domain

The numerical method and the method of its optimization is essentially the same as described in chapter 2. The major difference consists in the more important role of boundary layers and the specific geometry of the NACA profile. The resulting streamwise - transverse spectral element mesh thus contains more elements: we settled to a 572 element mesh represented in figure 4.4. The non-dimensionalization of the simulation being based on the chord length, the latter is of length equal to one. In the case of zero incidence, the tip of the leading edge is placed at the origin of the coordinate system. As will be explained later, to simulate a non zero incidence we rotate the profile with respect to the point situated half way between the leading and the trailing edge. The inflow boundary is placed at one chord length upstream of the leading edge, the streamwise length of the domain is $3.5c$ and the width is $2c$. The boundary conditions are those described in chapter 2.

The number of collocation points per spatial direction of spectral elements varied from 6 to 10 depending rather on the complexity of the simulation than on the Reynolds number. Taking account of the testing in the configuration of the circular cylinder we chose to work at the limit of available computing resources. In 2D simulations we took the maximal accuracy with 10 collocation points per spatial direction which guarantees a very good accuracy in the whole considered Reynolds number domain even if for lower Reynolds numbers this accuracy was unnecessary. The linear stability analysis, requiring considerably higher computing resources, was carried out with 8 collocation points. Considering that the obtained linear stability thresholds were found between $Re = 2000$ and $Re = 5000$ a numerical error may be expected for the found critical Reynolds numbers but this error is very likely less than 1%. The simulations with a large spanwise period were performed with 6 collocation points. In spite of that (due to a significantly larger number of spectral elements) they required more computing resources than analogical simulations of the flow past a circular cylinder. In view of the interest even of qualitatively correct data, the expected error, on the order of a few percent, is not detrimental to the relevance of the presented results. To simulate a 3D flow past an infinite body in spanwise direction the toroidal geometry represented in figure 2.3

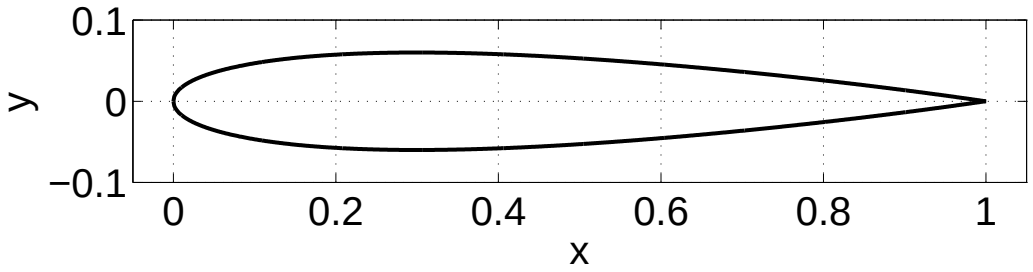

Figure 4.1: NACA 0012 profile generated by Eq. (4.3) for $c = 1$ and $t = 0.12$.

has again been retained. We already argued that for aspect ratios on the order of several hundreds the results are indistinguishable from those obtained for perfectly straight spanwise geometry. In the case of an airfoil the aspect ratio, defined as

$$Ar_{airfoil} = D/c \tag{4.2}$$

where D is the large diameter of the torus and c is the chord length actually corresponds to a much larger effective aspect ratio if the effective profile thickness is taken into account. However, the practical investigation of the transition to three-dimensionality described below set a still more strict limit to this aspect ratio. The length scales of the spanwise structures appeared to be considerably smaller than in the case of a cylinder. To keep a possibility of a sufficiently fine variation of the spanwise period we were obliged to consider very large spanwise ratios. Most results were obtained with a radial shift of $500c$, i.e. and aspect ration of 1000. Based on the effective thickness of an airfoil with zero angle of incidence, this corresponds to an effective aspect ratio $D/$ thickness equal to 8 333. The implementation of the toroidal geometry consists in adding a radial shift equal to the large radius of the torus to the radial component of the discretization. For the considered large aspect ratio a double precision representation was needed in order not to loose sensitivity to the radial (i.e. transverse) spatial position.

4.2.2 Numerical implementation

Some, slight modifications of the numerical tool were required to account comfortably for the profile form defined, in a standard way, analytically by the equation (written with four digits precision and for an arbitrary thickness t):

$$y = \frac{t}{0.2}\left[0.2969\sqrt{\frac{x}{c}} - 0.1260\frac{x}{c} - 0.3516\left(\frac{x}{c}\right)^2 + 0.2843\left(\frac{x}{c}\right)^3 - 0.1015\left(\frac{x}{c}\right)^4\right] \tag{4.3}$$

(and represented for $c = 1$ and $t = 0.12$ in Fig. 4.1), and to vary easily the angle of incidence.

The used pre-processor was not originally designed to account for arbitrarily curved sides. (Arcs of circles and splines were only implemented.) The direct implementation of

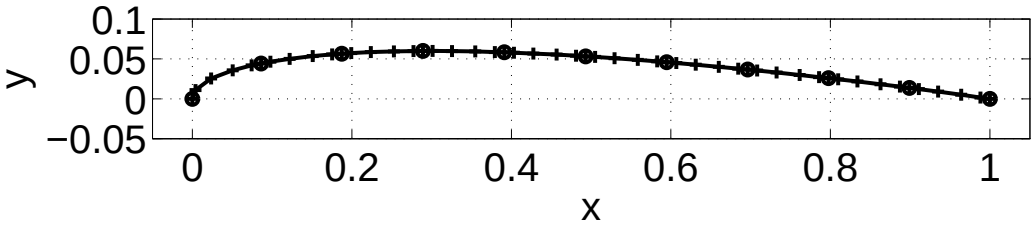

Figure 4.2: Example of a split up of the upper boundary of the NACA 0012 profile into 10 spectral elements (circles) subdivided by 6 internal collocation points (ticks).

the formula (4.3) was not a practical solution because the spectral element decomposition requires not only the splitting of the boundary of the airfoil arbitrarily into spectral elements but also an optimal distribution of the internal collocation points. We retained the following practical solution. We used first the pre-processor to define the profile boundary as a broken line or equivalently as a set of arcs of circles. The coordinates of the so defined segments are processed separately in Matlab. A Matlab routine parameterizes the NACA profile by the curvilinear abscissa s rather than by the streamwise projection x to avoid the singular representation close to the leading edge. The interval of abscissa s representing the profile is then broken up into subsegments corresponding to spectral elements which are further subdivided by collocation points (see Fig. 4.2). The coordinates of all generated collocation points are written in a file. The pre-processor has been adapted to import the data and to transfer them to the main code.

The next development concerned a comfortable generation of the geometry representing a profile with a non zero incidence. Originally, our intention was to simulate a non zero angle of incidence by boundary conditions. However, at higher incidence angles the wake tended to leave through the lateral boundary. (See Fig. 4.3 where the extreme case of angle of incidence of 20 degrees is represented). To simulate the wake correctly would have required an enlargement of the domain. For this reason we opted, instead, for deforming the inner part of the mesh by rotating the profile by the angle of incidence. The procedure was programmed in the pre-processor and allows the user to deform the mesh for a zero incidence so as to account for an arbitrary (albeit reasonable) incidence. The meshes used in this study for angle of incidences 0, 4, 8 and 12 degrees are represented in figure 4.4.

4.3 Two-dimensional flow

The performance of airfoils depends on the boundary layer separation. In regimes of practical applications (i.e. at high Reynolds numbers) the boundary layer separation results in a drastic decrease of the lift (stall). In our case, that of direct numerical simulations at low Reynolds numbers, the stall is not so spectacular because, as will be shown below, we are very far from approaching lifts predicted by the potential flow theory. Nevertheless, the boundary separation has been recognized as a precursor sign of the transition (see e.g. Bouchet *et al.*,

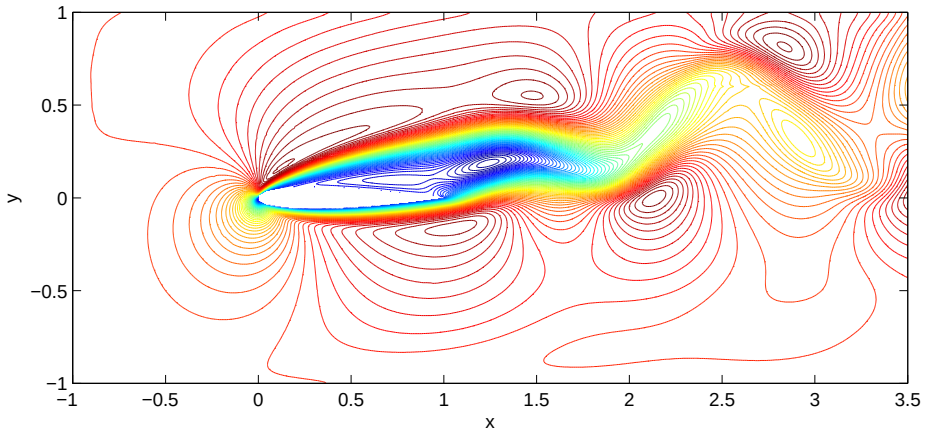

Figure 4.3: $2D$ wake flow at $Re = 500$ and with an angle of incidence 20° simulated by the inflow boundary condition.

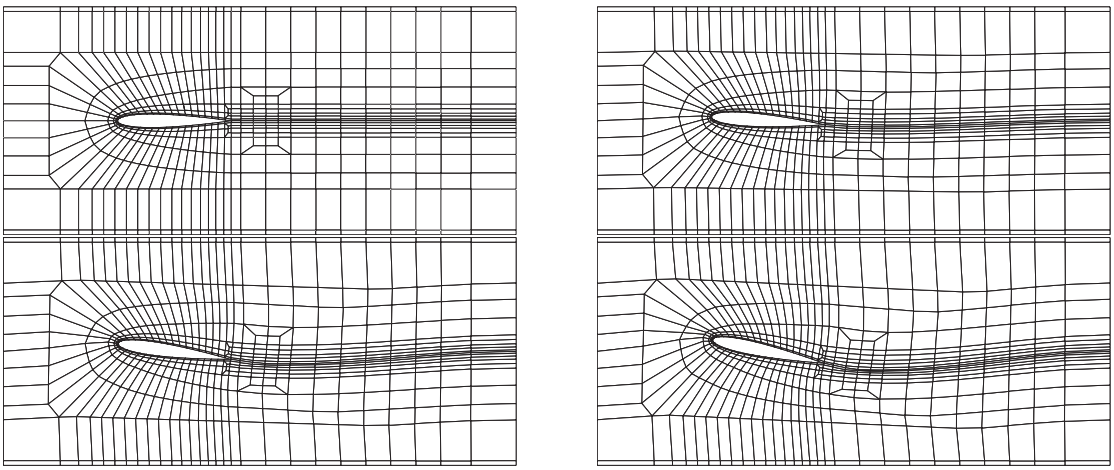

Figure 4.4: Spectral element mesh for angle of incidences (row-wise) 0, 4, 8 and 12 degrees.

angle of incidence	Re_{sep}
0°	8500
2°	2500
4°	1400
6°	900
8°	500
10°	350
12°	300

Table 4.1: Thresholds Re_{sep} of the boundary layer separation at angles of attack $0°, 2°, 4°, 6°, 8°, 10°$ and 12°. (Spatial discretization with 10 collocation points)

2006) we want to explore. As a consequence, we first investigate the thresholds of the flow separation. It is well-known that for infinite cylinders (practically of any cross section) a parallel vortex shedding sets in as a primary stage of the transition. Its thresholds can still be investigated by two-dimensional simulations. The corresponding results are thus also included in this section.

4.3.1 Steady attached flow and boundary layer separation

Two-dimensional direct numerical simulations have been performed to simulate the flow past a NACA 0012 airfoil NACA 0012 for angles of attack $0°, 2°, 4°, 6°, 8°, 10°$ and 12°. The maximum considered Reynolds number was 10 000. For each angle of attack the threshold of detachment (expressed in terms of the critical Reynolds number) has been determined. The results are summed up in the table 4.1. The flow separation starts from the trailing edge and its location shifts upstream both with increasing angle of incidence (see figure 4.5) and with increasing Reynolds number (see figure 4.6). 12° at the same $Re = 700$. The reason is that the adverse pressure gradient increases with increasing angle of attack resulting a shifting of flow separation from the upper surface of airfoil in the upstream direction. The lift coefficients at 8 and 12 degrees are 0.2866 and 0.3682 respectively.

4.3.2 Onset of vortex shedding

In agreement with expectations, we found that the vortex shedding is always preceded by a flow separation. The found thresholds of vortex shedding are summed up in table 4.2. They have been obtained by a relatively rough incrementation of the Reynolds number by 100. We considered a better precision irrelevant in this context. The reported values correspond to the lowest Reynolds number at which a developed vortex shedding was evidenced. I.e. the exact thresholds lie below by less than one hundred. For the onset of the vortex shedding at high angle of incidence an effective Reynolds number based on the effective profile thickness is relevant rather than that based on the chord length. The effective Reynolds numbers are also reported in table 4.2. The effective thickness is calculated by taking the projection of the tilted profile on the direction perpendicular to the inflow velocity (as the projection on

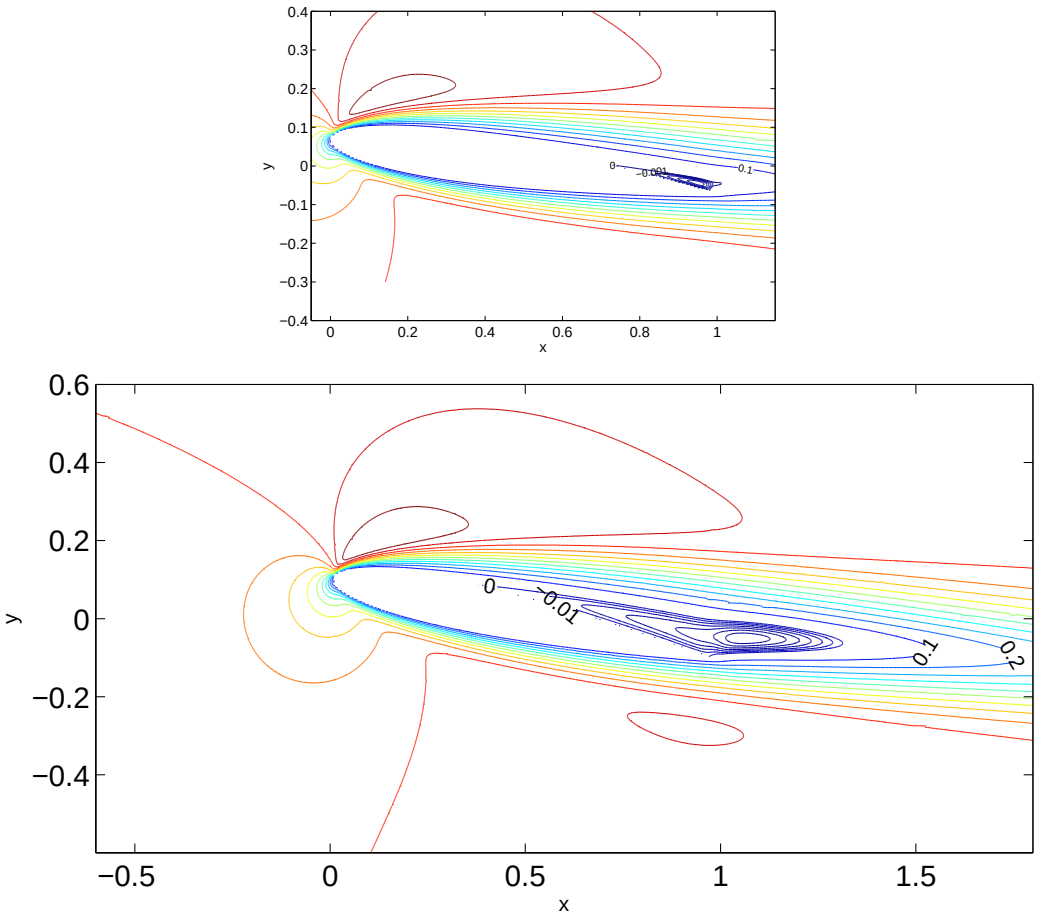

Figure 4.5: Separation bubble at $Re = 700$ for angles of attack (above) 8 and (below) 12 degrees. Iso-velocity contours of the streamwise velocity component are represented. The spacing of the levels of the contours in the recirculation bubble (delimited by the level 0) is ten times smaller than elsewhere.

the y-axis). It can be seen that even at the highest considered incidence of 12 degrees the airfoil is still far from acting as a bluff body.

4.3.3 Drag and lift

Drag and lift are the essential characteristics of airfoils, the prediction of which has always been the main purpose of theoretical developments and of numerical simulations. The potential flow theory (e.g. Chassaing, 1997) is inappropriate as a method of validation because of the small Reynolds numbers considered in our simulations. We obtained, however, a quite good agreement with numerical results coupling the potential flow with parabolic boundary layer equations. Such a numerical approach is very cheap and several implementations are

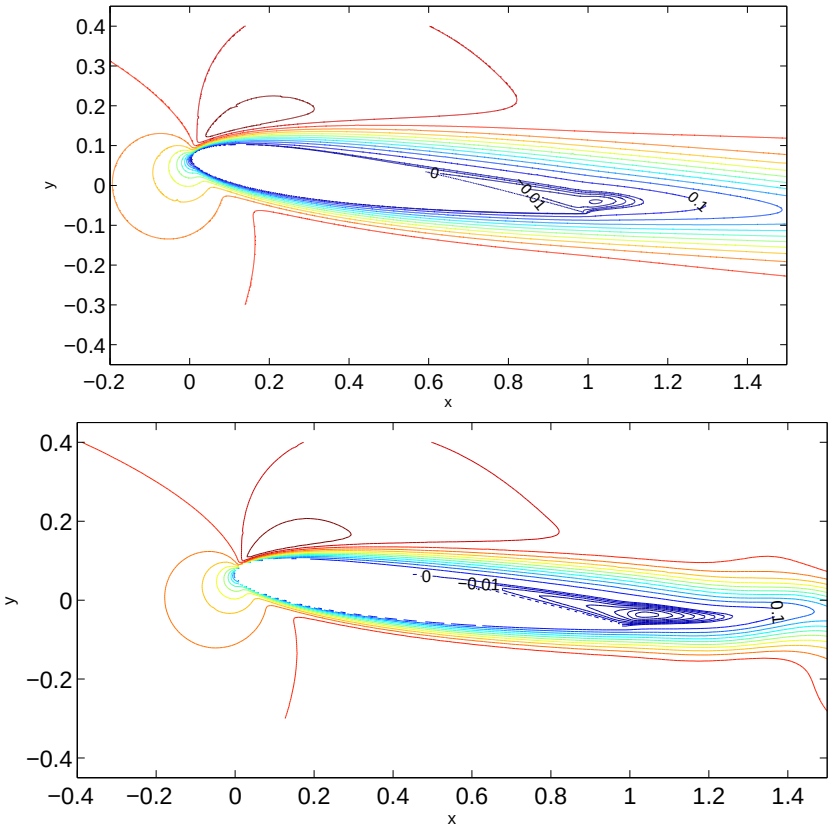

Figure 4.6: Separation bubble for incidence of 8 degrees at $Re = 1000$ (above) and $Re = 2000$ (below). The representation is the same as in figure 4.5.

available on-line. We chose Xfoil (see sec. 1.1) for this purpose. In the inviscid region, Xfoil describes the flow by a stream function obtained using a panel method. The potential flow solution is coupled with boundary layer equations used to describe the boundary layers and the wake. Xfoil accounts also, to some extent, for a boundary layer separation and for a laminar to turbulent boundary layer transition.

In what follows we present drag and lift coefficients defined as:

$$C_D = \frac{2F_D}{\rho U_\infty^2 c} \tag{4.4}$$

$$C_L = \frac{2F_L}{\rho U_\infty^2 c} \tag{4.5}$$

where F_D and F_L are the drag and the lift forces, respectively. Figures 4.7 and 4.8 represent the drag and lift coefficients in the two-dimensional flow compared to results predicted by Xfoil. For unsteady flows the mean lift coefficients are represented. The same data are re-plotted as functions of the angle of incidence at several Reynolds numbers in figure 4.9.

angle of incidence	Re_{crit}	$Re_{crit,eff}$	St_{crit}
0°	9400	1128	4.9628
2°	7000	859	2.1763
4°	4200	550	1.7419
6°	2600	382	1.4124
8°	1700	293	1.1696
10°	1100	223	0.9474
12°	800	187	0.8084

Table 4.2: Critical Reynolds numbers of the onset of vortex shedding. $Re_{crit,eff}$ $=Re_{crit}\, t_{eff}/c$ where t_{eff} is transverse projection of profile. St_{crit} stands for Strouhal numbers of the flow at the Reynolds number indicated in the second column.

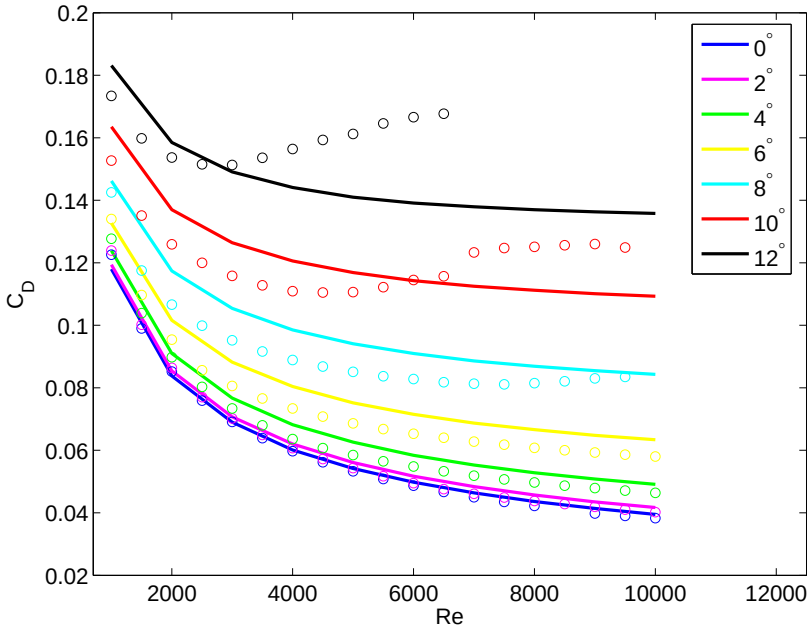

Figure 4.7: (Mean) drag coefficient as a function of the Reynolds number for angle of incidences 0 through 12 degrees. Empty circles: results of our simulations, full lines: data obtained by Xfoil.

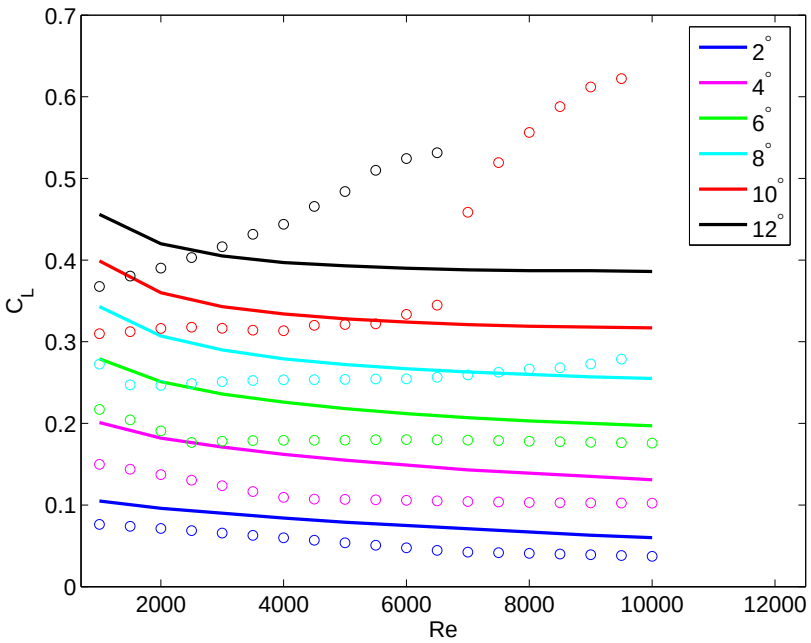

Figure 4.8: Mean (lift) coefficient as a function of the Reynolds number for angle of incidences 0 through 12 degrees. Empty circles: results of our simulations, full lines: data obtained by Xfoil.

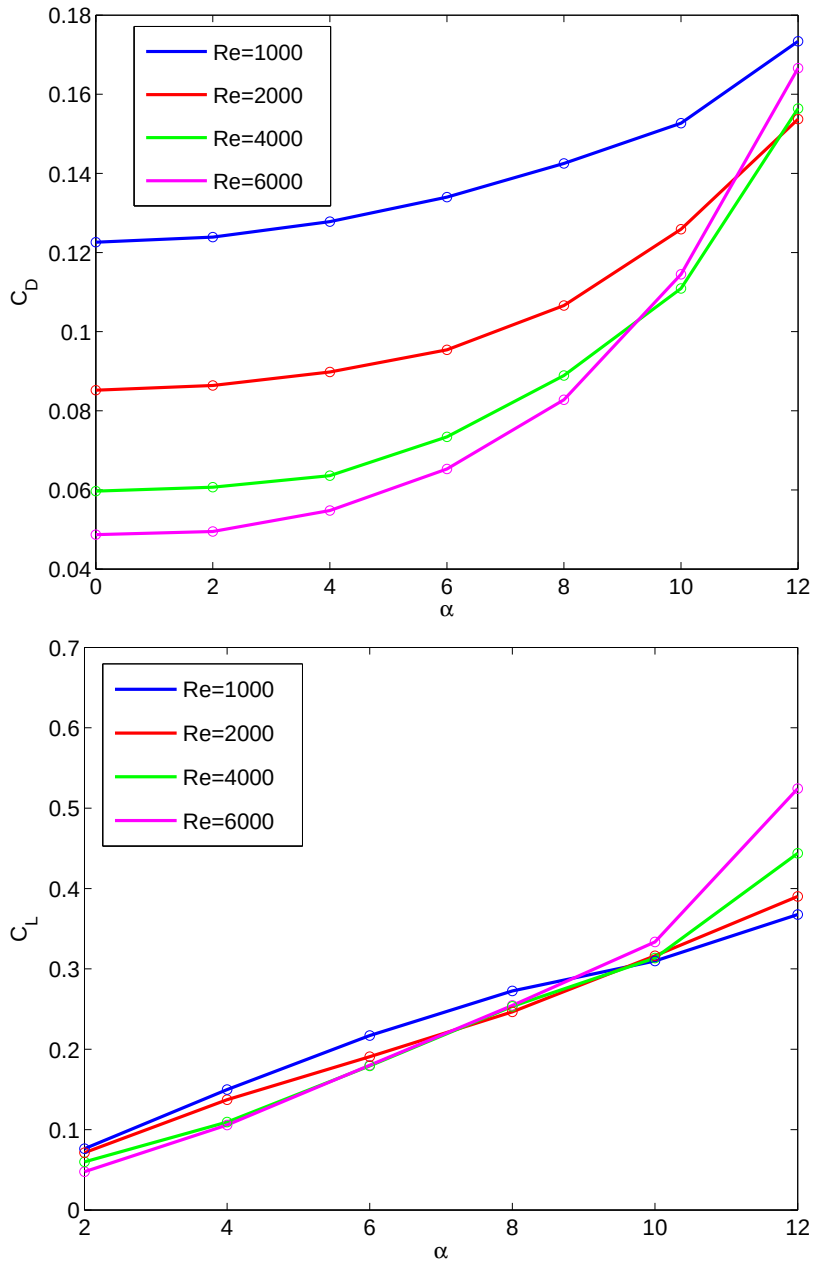

Figure 4.9: Above: Drag coefficient obtained by a 2D simulation against angles of attack at several Reynolds numbers. Below: lift coefficient.

At low angle of incidences there is a relatively good agreement between the results obtained by a (2D) direct numerical simulation and the Xfoil data. The agreement gets lost as soon as the flow becomes massively separated and a strong vortex shedding arises at

higher angle of incidences in the separated flow (see figure 4.10). It seems to be the vortex shedding at the suction side which is responsible for the strong increase of the drag (and induced lift) in Figs. 4.7 and 4.8. In regimes in which the unseparated and separated flow remain approximately steady, the lift is fairly independent of the Reynolds number (up to $Re = 6000$ and the angle of incidence of 10 degrees). However, the slope is more than 3 times less steep than predicted by the potential flow theory ($C_L \approx 0.32$ at 10 degrees as compared to $2\pi \sin\alpha = 1.09$ for the same angle of incidence α). This result, is however, in a good agreement with the Xfoil data represented in figure 4.8 where the lift coefficient only very weakly decreases as a function of the Reynolds number.

4.3.4 Characteristics of unsteady, periodic flows

The vortex shedding sets in even if the separation bubble remains relatively limited (see figure 4.11). This has an impact on the Strouhal number (see figure 4.12). For (almost) un-separated flows the Strouhal number is almost independent of the angle of incidence. As soon as the flow separation becomes significant the size of the separation bubble increases with the angle of incidence and tends to yield a lower Strouhal number.

4.4 Three-dimensional flow

Results on the linear stability of the two-dimensional flow past an airfoil have never been published. Beyond their fundamental importance for the understanding of the transition scenario in this configuration they may also be of interest for turbulence modeling because they provide an estimation of the minimal eddy viscosity at which the spanwise structures can be neglected. In the case of three-dimensional simulations, such data make it possible to assess the size of spanwise structures. The scales defined by the linear preferred wavelengths yield relevant information even if, as shown in our study of the wake of the cylinder, they serve only as a qualitative indication of the scales to be considered in a simulation.

4.4.1 Linear instability investigation

For the airfoil we use the same method of linear stability investigation as that described in Sec. 3.3.1. We allowed for three-dimensionality at minimal costs by running a non-linear simulation with just two modes: $m = 0$ and 1 with a variable spanwise wavenumber (wavelength) of the mode 1. The number of collocation points was decreased to 8 in order to put the computing costs (time of simulation runs) within reasonable limits. The aspect ratio of the numerical torus was taken to be $Ar = 1000$. As consequence, if, e.g. a spanwise period of $\lambda = 0.1c$ was to be set, the fundamental 'azimuthal' wavenumber M (see Eqs. (2.40, 2.41)) was equal to $M = \pi D/\lambda \approx 31\,400$. The investigation of the marginal stability consisted thus in sweeping the (Re, λ) parameter plane and in monitoring the amplification (decay) of the mode $m = 1$. We used a 'history' point at $x = 2c$ (one chord length downstream of trailing edge) and $y = 0$ and monitored the spanwise velocity component appearing due to the onset of three-dimensionality.

The difficulty consisted in the absence of any data helping us to estimate *a priori* the critical Reynolds number and the preferred wavelength. This made the investigation time consuming because many runs were only marginally relevant for the accurate determination of the critical parameters and could not be taken into account for plotting the marginal stability curves. This was already a reason to limit the number of investigated angle of incidences. The other, and more important, reason was that the interval between the onset of vortex shedding and the upper limit of the investigated Reynolds numbers (10 000) becomes very narrow at low angle of incidences. The accumulated experience with the circular cylinder wake indicates that the onset of three-dimensionality is situated at significantly higher Reynolds numbers than the primary bifurcation. As a result, we could reasonable assume that at incidences smaller or equal to 4 degrees the three-dimensionality does not set in below $Re = 10^4$. The case of 6 degrees might deserve investigation but it was not tackled.

The computing costs are also higher than for the circular cylinder because of the finer spatial discretization of the boundary layers. The induced fine time step and the relatively large time period of the wake necessitate many time steps of simulation. The time behavior is very far from harmonic and involves many smaller time-scales. An idea of the 'signals' that were used for determining the growth (decay) rates can be obtained from figure 4.13. In this figure, 16 vortex shedding periods are represented, each necessitating about 4000 time-steps. In spite of a two-dimensional simulation the run took 48 hours. A significant number of similar simulations was necessary to produce the linear marginal curves presented below. The method of investigation consisted first in sweeping roughly the spanwise wavenumbers for a given angle of incidence at a more or less arbitrarily chosen Reynolds number. The first guess improved once the first marginal stability curve had been obtained for the first angle of incidence (8^o). We sought for three consecutive wavenumbers such that the decay rate (we rarely hit a Reynolds number above the threshold at the first guess) was minimal for the middle value. This was equivalent to capturing, roughly, the less decaying wavelength. Then we kept this wavenumber and increased the Reynolds number until the instability was captured. Starting from this last Reynolds number value more accurate sweeps were carried out for a variable wavenumber to determine the limits of the instability interval.

We obtained three linear marginal stability curves for a wing at incidence angles of 8, 10 and 12 degrees (see figure 4.4.1). At the angle of incidence 8 degrees, which we started with, we estimated the least decay rate first at $Re = 2000$. It was at $m = 45000$, i.e. at $\lambda = 0.07c$. The last investigated Reynolds numbers were $5400, 5420$ and 5450. At this wavelength we evidence the instability at about $Re = 5500$. The last investigated Reynolds numbers were $5400, 5420$ and 5450. At each of these Reynolds numbers we swept the spanwise wavenumbers M with an increment of 500 . An example of determination of the instability interval is provided in table 4.3. The marginal stability curve of figure 4.4.1a) is a result of about 90 simulations. All the simulations at $Re = 5400$ decayed linearly; therefore the flow is still stable at this Reynolds number. At Reynolds numbers 5420 and 5450 instability intervals were obtained by interpolation between neighboring cases of growth and decay. The so obtained 4 points were used to estimate the position of the cusp of the curve by spline interpolation. This prediction has been verified by sweeping the wavelengths again at $Re = 5415$. This procedure allowed us to determine the critical parameters with a better precision than numerical errors due to insufficient spatial discretization accuracy. We

fundamental mode m	growth/decay rate
15500	-0.0243
16037	interpolation
16800	0.0345
17400	0.0472
18000	0.0528
19200	0.0465
19800	0.0355
20400	0.0205
21000	0.0071
21021	interpolation
21500	-0.0391

Table 4.3: Amplification rates for incidence 12 degrees and the Reynolds number $Re = 2230$ for variable spanwise wavenumber m. The values of m can be converted to wavelengths using the formula $\lambda = 1000\pi/m$.

angle of incidence	Re_{3D}	λ_{3D}
8°	5412.7	$0.0863c$
10°	3580.4	$0.1246c$
12°	2203.3	$0.1708c$

Table 4.4: Results of linear analysis of the stability of the two-dimensional flow: three critical Reynolds number and corresponding preferred spanwise wavelengths at three angles of incidence 8, 10 and 12 degrees of the transition to three-dimensionality.

obtained a critical Reynolds number 5412.7 and critical spanwise wavelength 0.0863 chord length. (See fig.4.4.1a)). Similarly, at 10 degrees, the marginal stability curve results from simulations at Reynolds numbers 3610, 3600, 3590 and 3581 and, that at 12 degrees, from simulations at $Re = 2210$, 2230 and 2300. The resulting linear marginal stability curves are shown in the figures 4.4.1b) and 4.4.1c). The critical parameters are assembled in table 4.4. As expected, the critical Reynolds numbers of the transition to three-dimensionality lie well above those of the primary bifurcation (table 4.2).

4.4.2 Non-linear effects

Fully non-linear simulations with spanwise expansions (2.40, 2.41) truncated at $m_{max} = 6$ were run for the incidence 12 degrees with the periodicity given by the preferred spanwise wavelength. The first run was carried at a Reynolds number significantly above the critical value ($Re = 2700$) until the saturation of the spanwise mode. Then the Reynolds number was decreased down to $Re = 2200$. At $Re = 2200$ the spanwise mode was observed to decay to zero. The amplitudes of oscillation of the fundamental spanwise mode of spanwise

velocity at the point $x = 2c, y = 0$ are represented in figure 4.15. It is seen that not only the bi-stability is absent but also the square-root like behavior of the instability amplitude at the threshold is found. Both features witness of the supercritical nature of the bifurcation. The explanation may be the short spanwise length of the three-dimensional mode and the fact that, as we have seen for the circular cylinder wake, the sub-criticality disappears for the mode A as soon as the spanwise period is set too short. The subcriticality has never been observed for the pure mode B with its very short spanwise scale. Indeed, the spatial structure of the unstable mode resembles rather to that of the B-mode (see figure 4.16). Also if the spanwise wavelength of $0.171c$ is compared rather to the effective thickness of the wing ($t_{eff} = 0.2338c$) a ratio $\lambda/t_{eff} = 0.72$ is obtained, which is close to the values characteristic of the mode B in the cylinder wake.

4.4.3 Large spanwise period of simulation

The sub-criticality cannot be excluded on the basis of the results obtained in the previous subsection. Indeed, it may happen that the preferred spanwise wavelength is shorter than the spanwise period of the onset of sub-criticality (see section 3.4). The latter may correspond to several times the preferred wavelength. The results in chapter 3 showed that a simulation with a spanwise periodicity many (several) times longer than the preferred spanwise wavelength is more likely to reflect the physically relevant flow. Because of the limited time for the elaboration of the results, the high computing costs of the study and the risks of obtaining many negative results we could not repeat exactly the same investigation as for the circular cylinder. Instead we decided to focus on the rise of subharmonic spanwise length scales. The latter appeared to be crucial for bringing the numerical simulations of the wake of a circular cylinder in agreement with experimental observations. To answer the question whether the preferred spanwise wavelength provides a relevant spanwise periodicity for numerical simulations, albeit in transitional regimes, it is interesting to see if in some slightly supercritical regime, subharmonic scales are excited in a three-dimensional simulation. This amounts to an investigation of the stability of the three-dimensional state with the spanwise period given by the linearly preferred wavelength λ_{lin} discussed in section 4.4.2. We chose the angle of incidence of 12^o and the Reynolds number of 2300 (the critical Reynolds being about 2200 - see table 4.4).

For the purpose of this study a similar method of excitation of the short-wave solution as in the case of the circular cylinder was adopted. A saturated state was obtained first with the spanwise period $\lambda = \lambda_{lin} = 0.17c$. This corresponds to the fundamental mode of the Fourier expansion (2.40, 2.41) $M = \pi Ar/\lambda = 18400$. (Recall that $Ar = 1000$.) To investigate the effect of doubling the period, the fundamental mode of the Fourier expansion was divided by 2 ($M = 9200$). The original expansion with $M = 18400$ is thus equivalent to the new one with odd modes $m = 1, 3, \ldots$ identically zero. The initial condition for the new simulation was thus defined by copying the Fourier modes of the previous simulation into even modes of the new one. The numerical method being based, itself, on the same Fourier mode expansion, the non-linear couplings provide no perturbation of the odd modes. For this purpose the subspace of odd modes had to be perturbed artificially. This was done, in the same way as in chapter 3, by copying the original fundamental mode not only to the new

$m = 2$ mode but also to the new fundamental $m = 1$ mode. The procedure was applied for a double and octuple spanwise period (2 λ_{lin} and 8 λ_{lin}). The expansion of the simulation with the spanwise period 2 λ_{lin} was truncated at the 12-th mode, that with spanwise period 8 λ_{lin} at 31-th mode to allow for the use of the fast Fourier transformation.

In figure 4.17 the odd modes, corresponding to the new spanwise scales opened by the double spanwise period, clearly decay. This means, that the linearly preferred spanwise scale remains as the largest one even in this simulation and that no transfer of energy towards the larger, double, scale occurs. In figure 4.18 a similar result is obtained. In this graph, the mode $m = 8$ corresponds to the simulation with the initial spanwise period of $0.171c$. All other represented modes 1 through 7 correspond to the newly opened spanwise scales. After an initial increase the growth of the mode 1 ceases and all subharmonics $m = 1$ through 7 start to decay. Of course, it has to be expected that subharmonic scales arise anyway in the turbulent wake. However, the transition scenario in the wake of an airfoil follows, very likely, a more classical route marked by successive bifurcations.

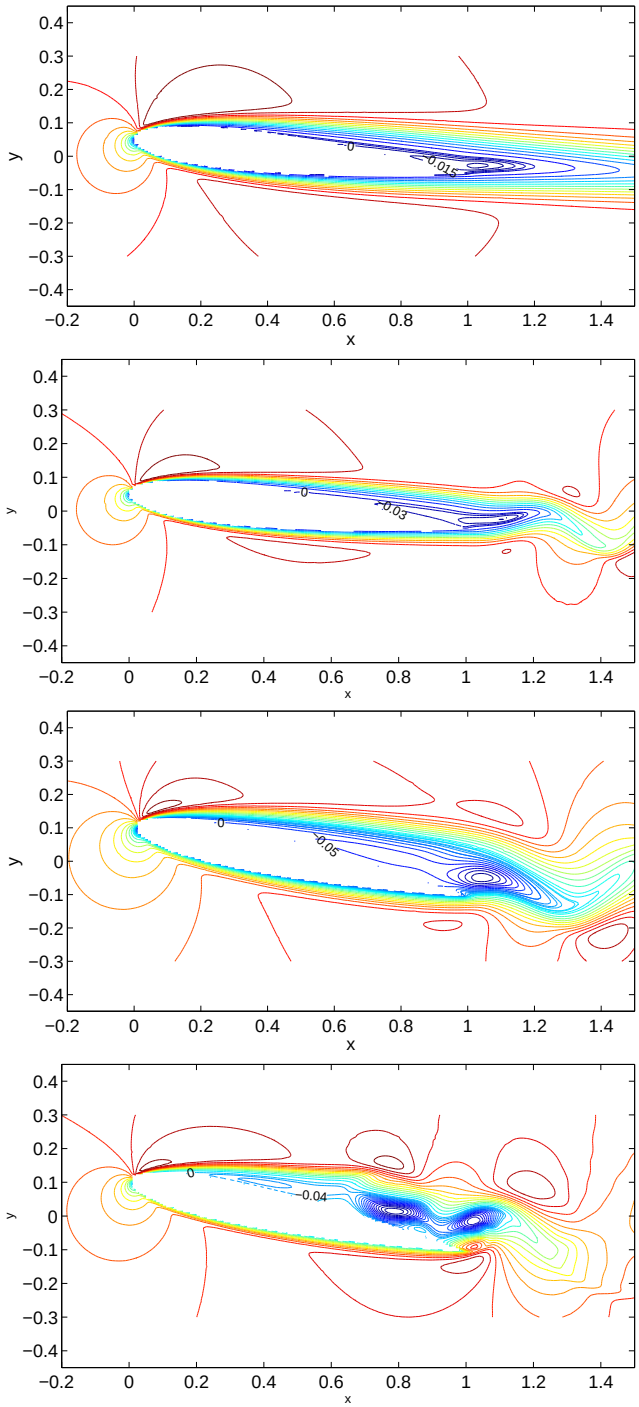

Figure 4.10: Iso-contours of streamwise velocity for $Re = 2000$ and 5000 and angles of attack 6° and 12° (from top to bottom: $Re = 2000$, 6°; $Re = 5000$, 6°; $Re = 2000$, 12°; $Re = 5000$, 12°).

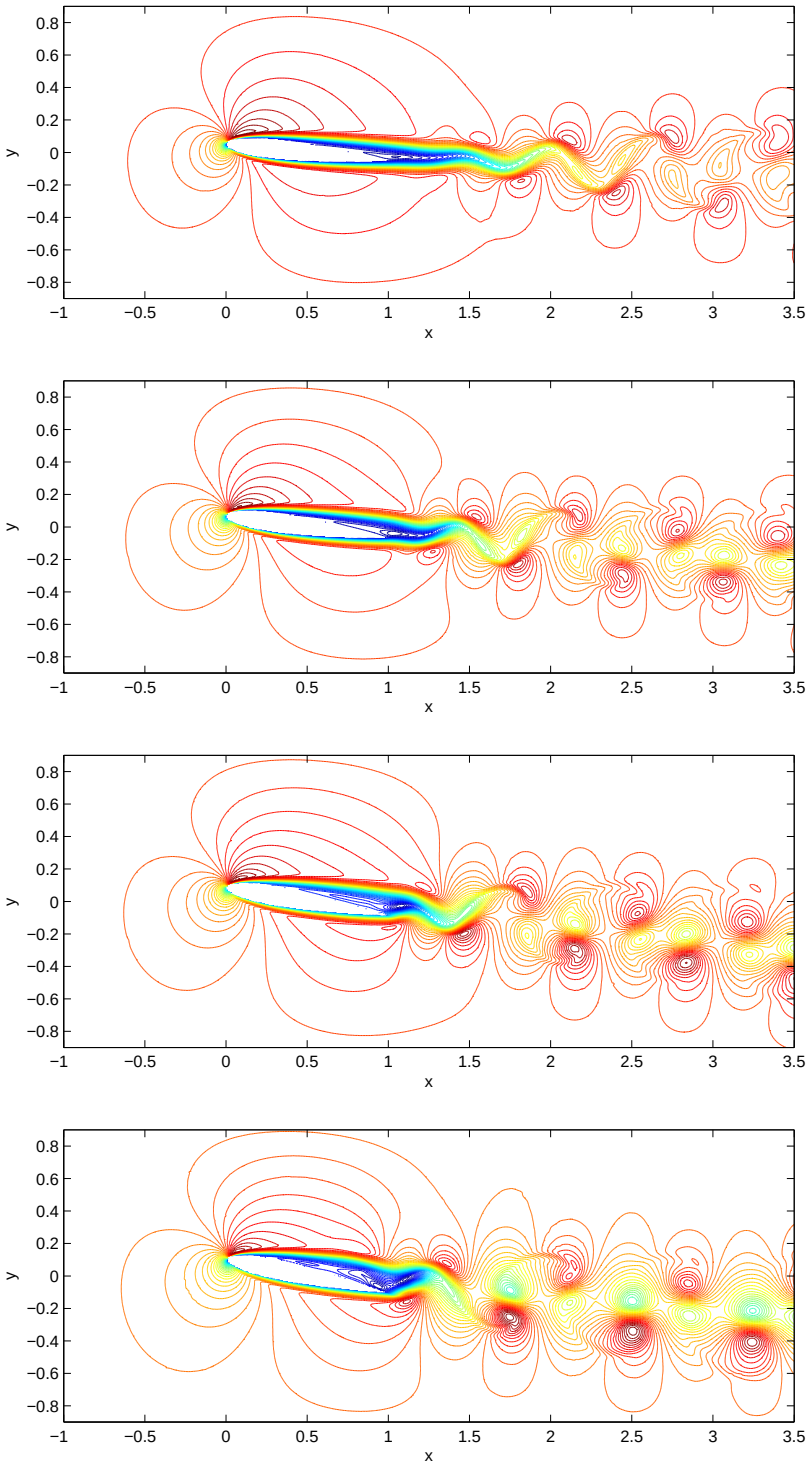

Figure 4.11: Iso-contours of streamwise of velocity (increment of contours: 0.03 of inflow velocity) at $Re = 3000$ and angles of attack $6°, 8°, 10°$ and $12°$ (from top to bottom).

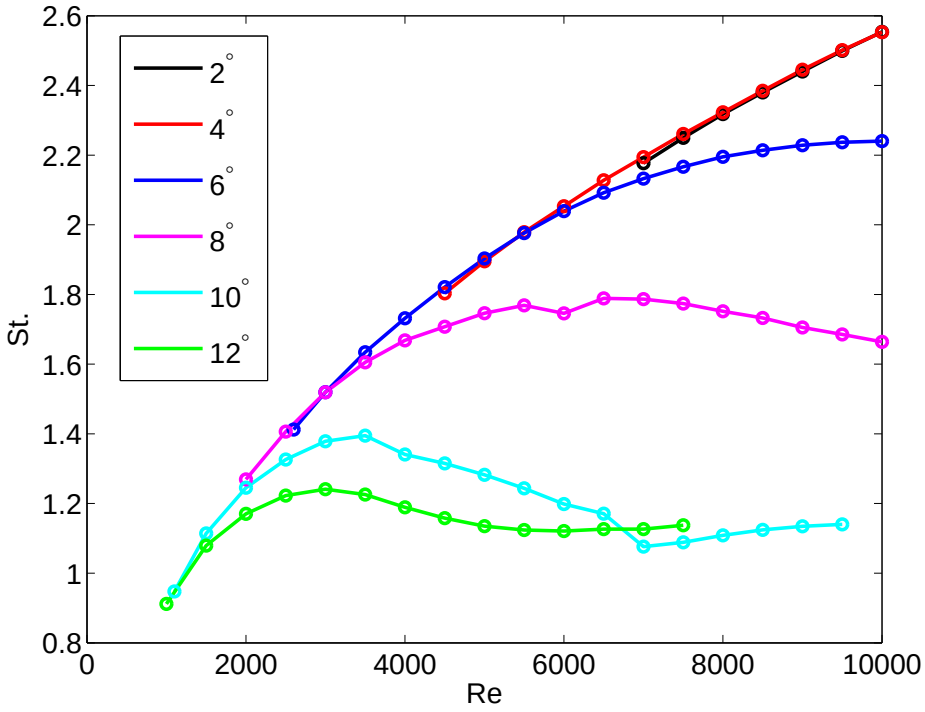

Figure 4.12: Strouhal number as a function of the Reynolds number for increasing angle of incidence.

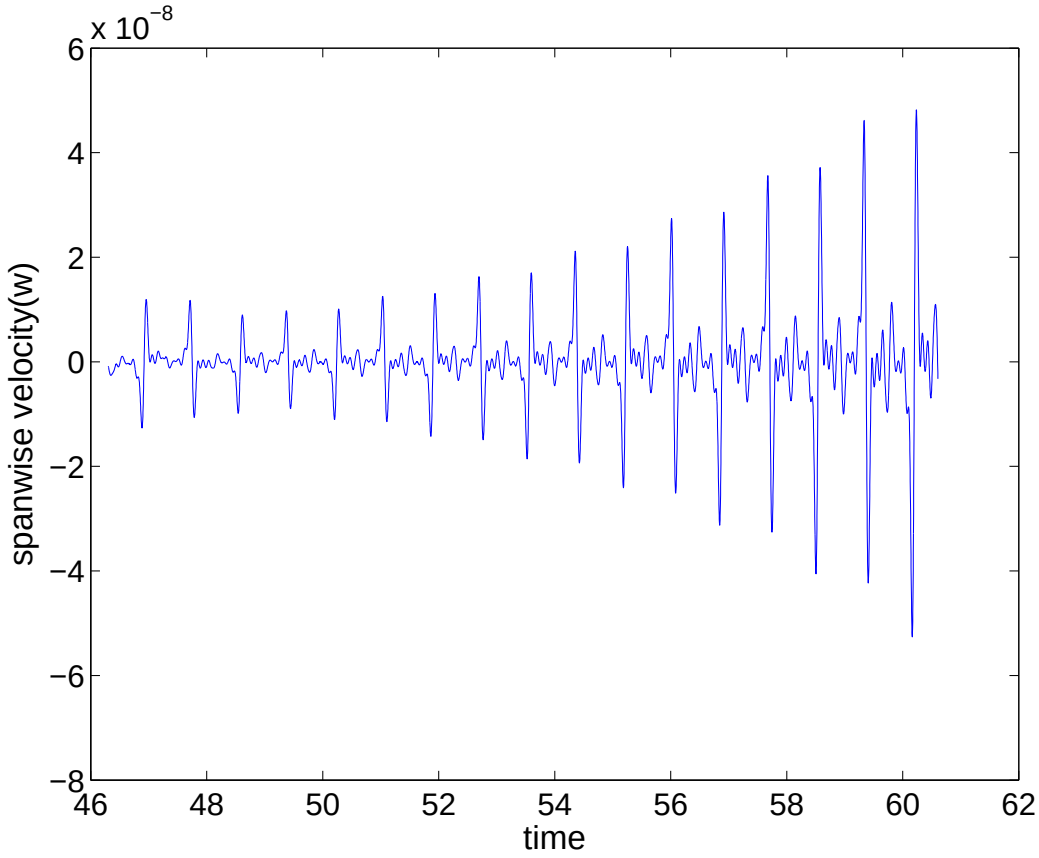

Figure 4.13: Time evolution of spanwise velocity w (mode $m = 1$) at the station $x = 2.0c$ (1 c downstream of the trailing edge of the airfoil).

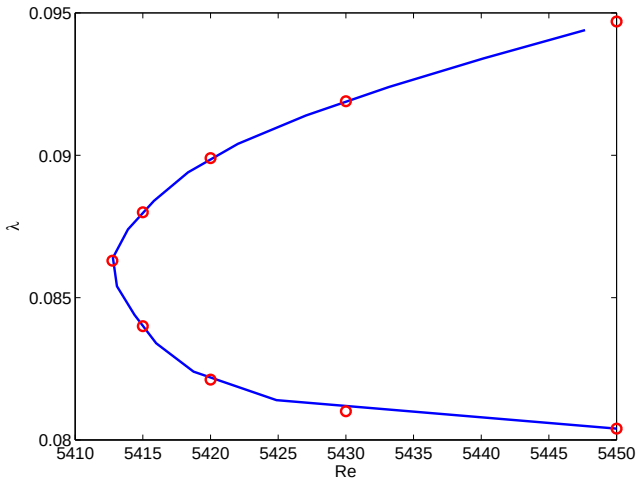

4.14.a

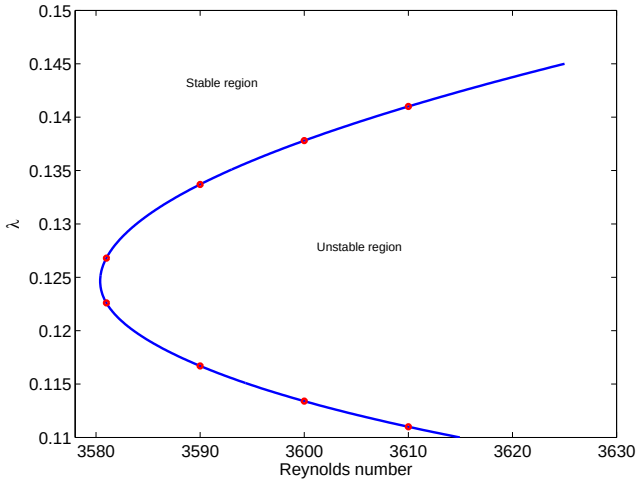

4.14.b

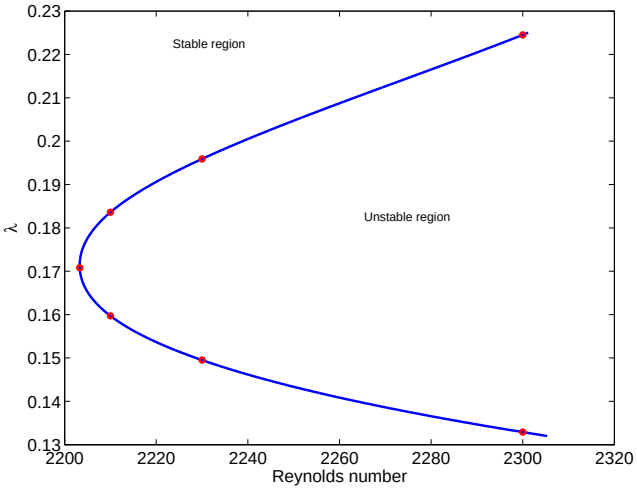

4.14.c

Figure 4.14: Linear marginal stability curves for NACA0012: (a) Angle of incidence 8 degrees, (b) angle of incidence 10 degrees and (c) angle of incidence 12 degrees.

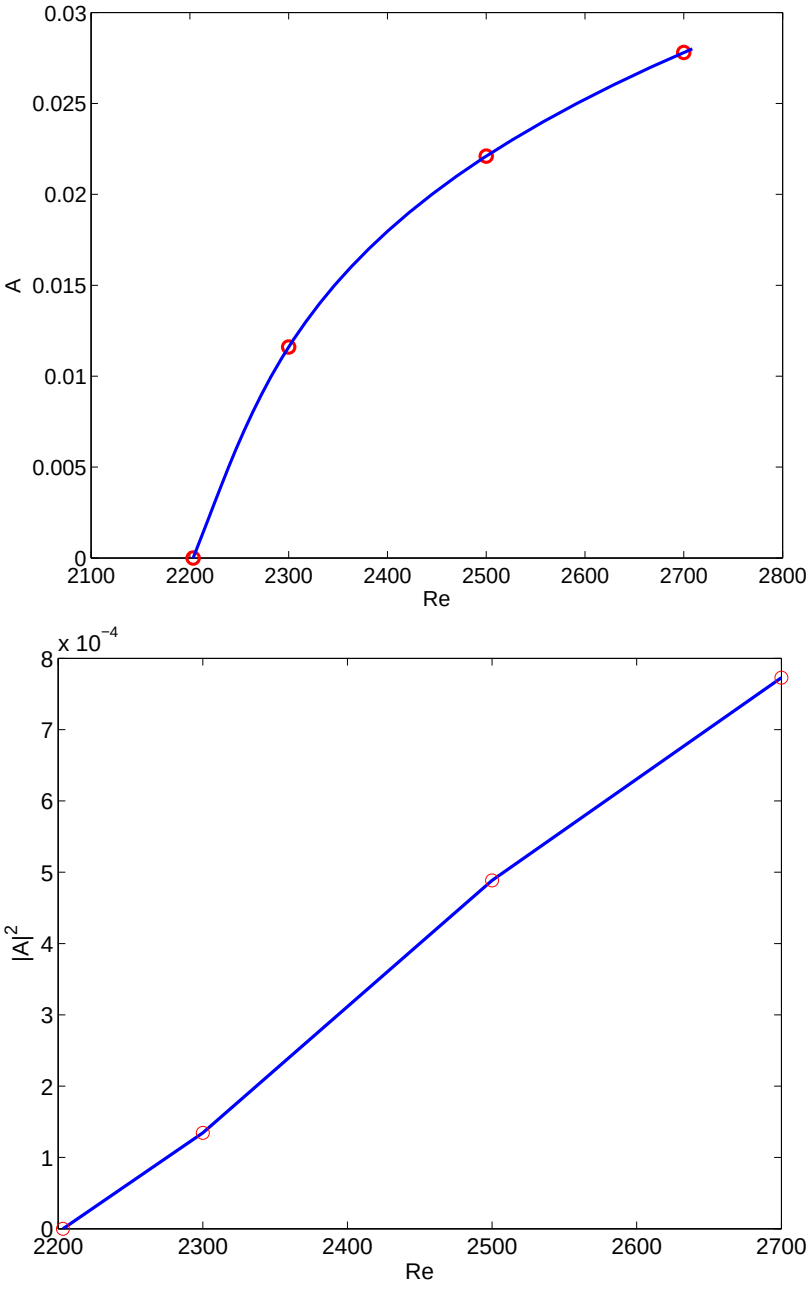

Figure 4.15: Upper figure: Amplitude of oscillation of the fundamental Fourier mode of the spanwise velocity at the point $x = 2c$, $y = 0$ vs. Reynolds number for the angle of incidence of 12 degrees and spanwise period of simulation $0.171c$. Lower figure: the square of the amplitude vs. Reynolds number.

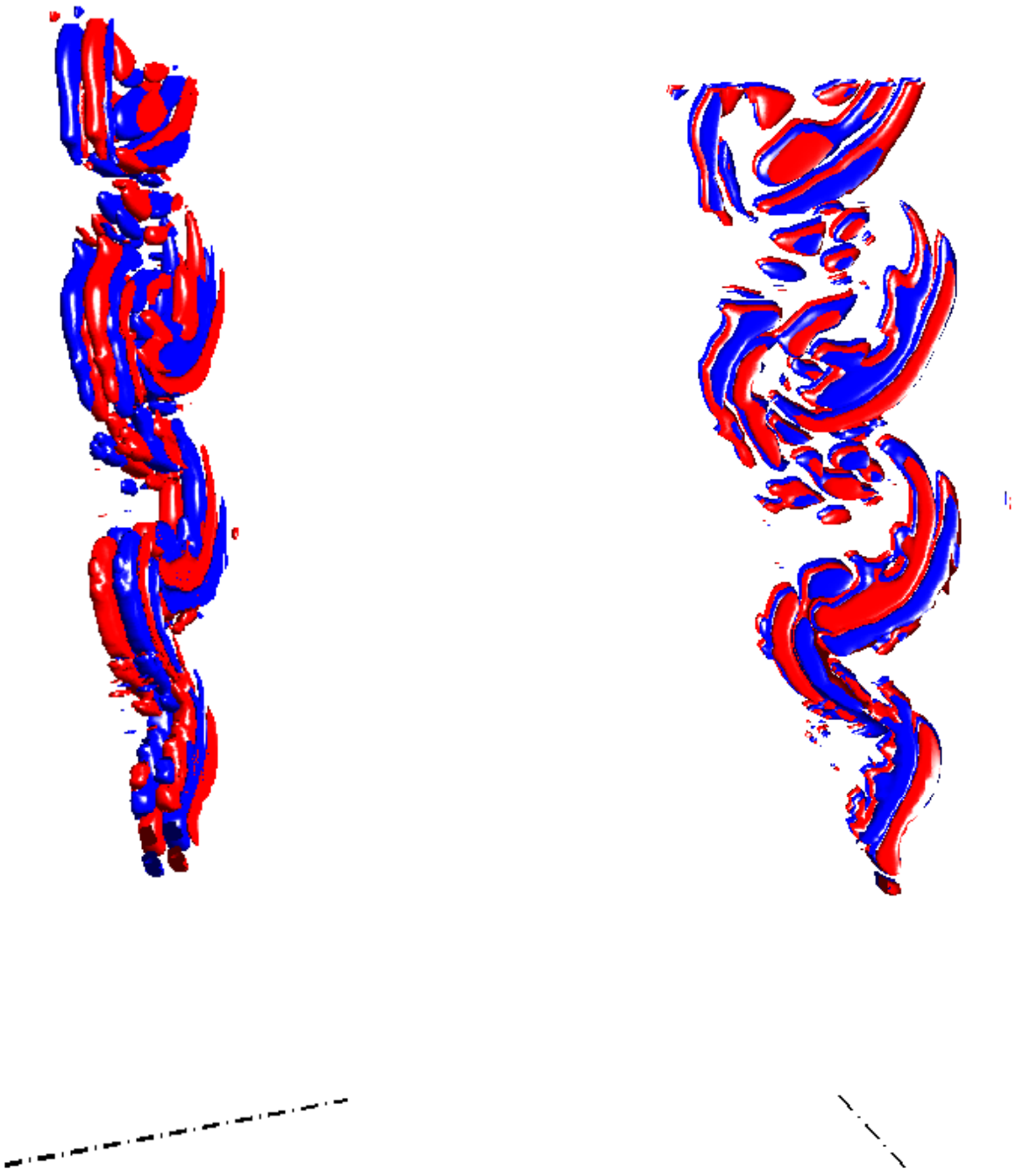

Figure 4.16: Iso-surface of spanwise velocity of the three-dimensional mode at $Re = 2300$, angle of incidence 12^o and with spanwise periodicity $0.171c$ taken at $\pm 5\%$ of inflow velocity. The position of the leading edge of the profile is represented by the dash-dotted line.

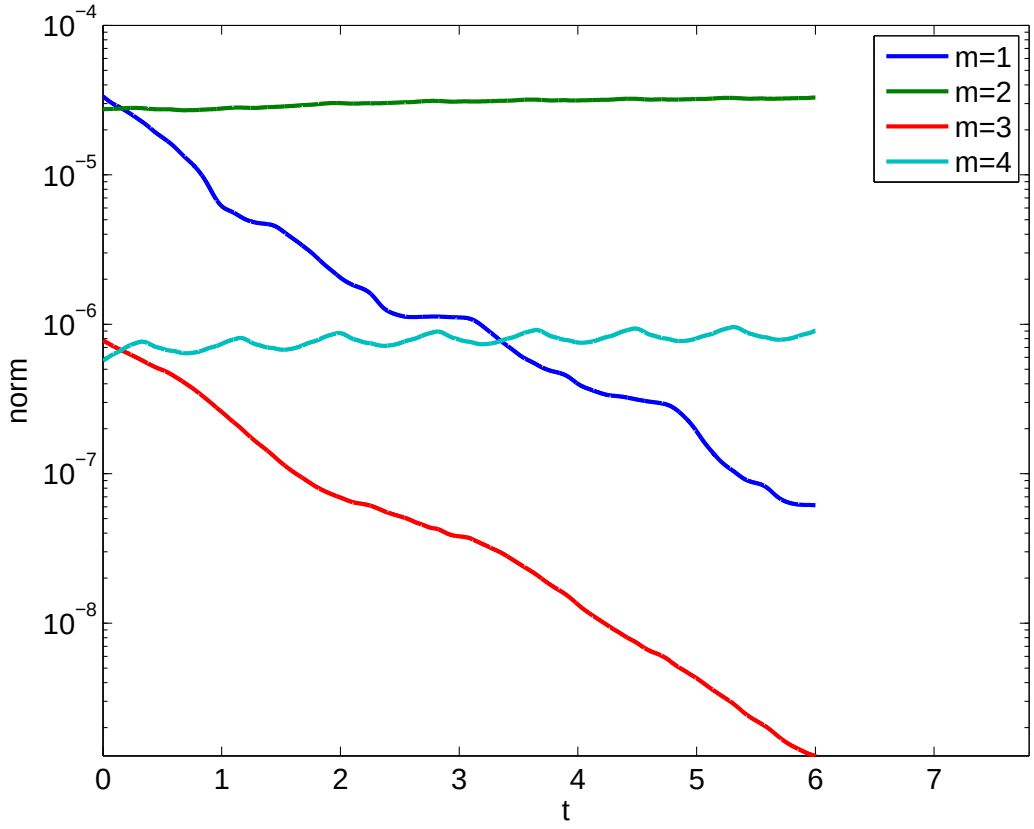

Figure 4.17: Time evolution of L^2 norms (see chapter 3) of Fourier modes 1 and 2 of the simulation with spanwise period $2 \times \lambda_{lin}$ at $Re = 2300$ and angle of incidence 12^o. In this case, mode 2 is the original fundamental mode of the simulation with spanwise period λ_{lin}.

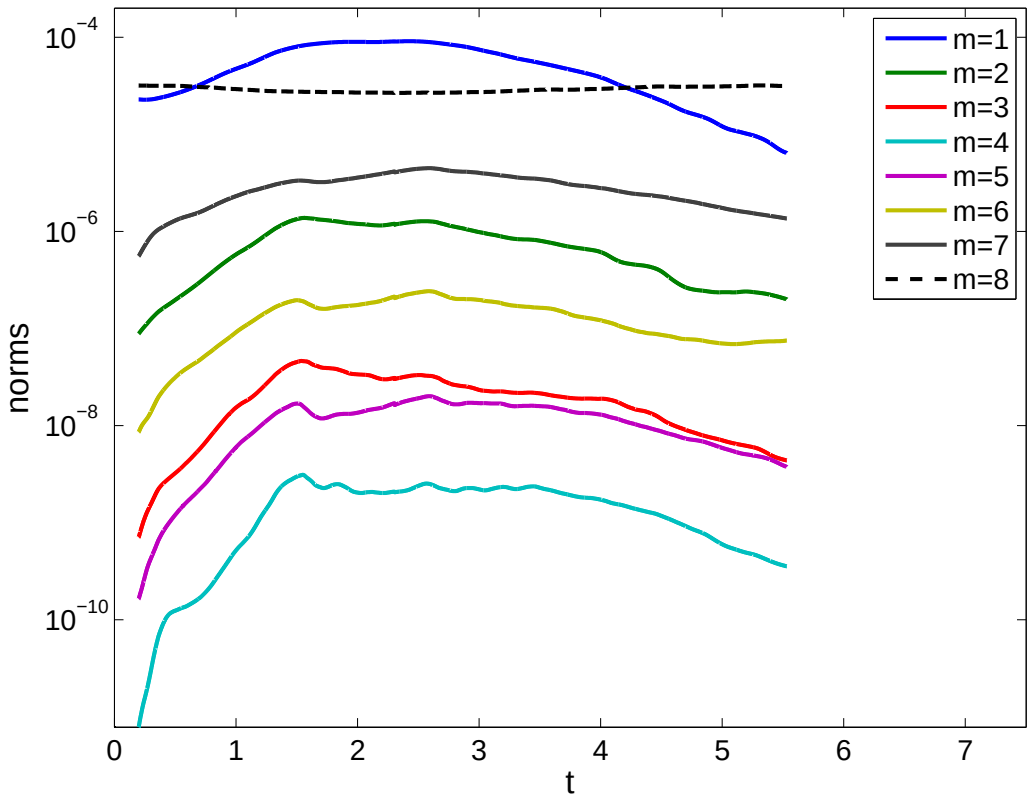

Figure 4.18: Time evolution of L^2 norms of Fourier modes 1 through 8 of the simulation with spanwise period $8 \times \lambda_{lin}$ at $Re = 2300$ and angle of incidence 12^o. Mode 8 is the original fundamental mode.

Chapter 5

Conclusion and perspectives

The present thesis started from the idea that the stability theory developed in the framework of investigations of the transition to turbulence in the wake of an infinite circular cylinder might be transposed to infinite airfoil profiles and might help in designing an efficient simulation method facilitating the investigation of such phenomena like the flow separation and static and dynamic stall with acceptable costs by direct numerical simulations. At the start, the simulation of the circular cylinder wake was tackled only as a testing configuration assuming that, in view of an absence of virtually any new published results for more than ten years, the circular cylinder wake represented a closed and completed chapter. Very soon, however, a closer look at the available bibliography on the transition to three-dimensionality showed significant discrepancies between experimental observations and published numerical data. Surprisingly enough, these discrepancies were never discussed in published numerical papers.

Chronologically, the experimental observations (that by Williamson, 1988*b*)) were published several years before the first linear analysis (that by Noack *et al.*, 1993), which still appeared not to be quite correct mathematically. The later mathematically correct and accurate result have been accepted as satisfactory rather due to their internal mathematical coherence than as a result of a careful validation by experimental data. From the physical viewpoint, their success was only very partial. Of course, the predicted preferred spanwise wavelength of the instability was found in a good agreement with that of the mode A observed to dominate the circular cylinder wake at the Reynolds numbers close to the critical value found by the linear theory, but many features reported from experimental observations were considered only at a very qualitative level or were not discussed at all. Even though Henderson & Barkley (1996) happened to evidence the subcritical nature of the bifurcation triggering the three-dimensionality, absolutely no mention of the bi-stability in the experimental data of Williamson (1988*b*) can be found in their paper. As far as the shorter wave mode B is concerned, it's investigation by Barkley & Henderson (1996) and other authors cited in section 1.2 is much more a nice mathematical exercise than a theoretical study of physical interest because the 2D flow is still taken as the base flow of the bifurcation. As a result, the reported threshold is of no physical relevance and only the weak dependence of the wavelength of the mode B explains a relatively satisfactory agreement between the observed

and predicted wavelength. The weakness of this approach was only partially overcome by Barkley *et al.* (2000) who took account of the reported experimental observation of the B mode well below the previously predicted threshold in an improved non-linear model. Again, however, the latter lacks a deeper physical analysis. It is fitted to the speculative assumption of the existence of a mode B triggering bifurcation, the threshold of which is set to be equal to lowest Reynolds number at which the mode B was reported. A more careful reading of the experimental bibliography shows, however, that a mode B triggering bifurcation was never observed and that the experimental papers clearly mention the progressive transfer of energy between modes B and A. It is thus to be expected that the lowest Reynolds number at which mode B was observed corresponds rather to a situation when it emerges from the experimental noise than to a bifurcation threshold. Last but not least, all experimental observations evidence a chaotic behavior at the very threshold of the three-dimensionality. Again, this fact did not draw the appropriate attention of the numericists. Henderson (1997) came very close to answering the above questions but missed the point of applying his investigation to the physically relevant interval of Reynolds numbers. Since his paper, the focus of the numerical work has shifted rather to the wake of tori and the subject has been abandoned.

In Chapter 3 we adapted a very well tested numerical tool to the task of simulation of flows in infinite geometries. An excellent agreement with already published data showed that the chosen numerical tool is able to provide not only qualitatively reliable data but that quantitative data such as instability thresholds and Strouhal numbers of vortex shedding in the wake can be reproduced within an accuracy of a fraction of percent. This set up a good basis for seeking the answers to physically more relevant questions. As a first stage, we submitted the relevance of the marginal stability curve for the understanding of the behavior of a system undergoing a subcritical bifurcation to a critical examination. We showed, that the linear results provide, in this case, only a very incomplete information and we suggested to investigate what we called a non-linear marginal stability curve connecting points of the Re-λ parameter plane representing the lower limits of the bi-stability interval. In some cases, such a curve might, potentially, assume a similar shape to that of the linear marginal stability curve and might thus provide a quantitatively different but qualitatively similar prediction of the preferred wavelengths of the subcritical regime. In the case of the bifurcation triggering the three-dimensionality in the circular cylinder wake the non-linear marginal stability curve appears, however, to fail in predicting any preferred subcritical wavelength. It opens rather all large spanwise scales. This finding suggested us the idea that, physically, the energy of the wake tends to be redistributed to all large scales, possibly with the only limitation of the real ends of the experimental cylinder or, in our configuration, of the full size of a real torus. In view of the practical impossibility to simulate such a configuration with acceptable numerical costs we attempted to investigate the phenomenon of the subharmonic energy redistribution by taking what we considered the largest practically viable spanwise period (significantly larger than that of Henderson (1997)). In spite of many practical numerical difficulties due to the strongly chaotic behavior of the simulated flow causing a frequent explosion of the time-stepping method we arrived not only at qualitatively relevant results but, luckily enough, the chosen spanwise periodicity appeared to be sufficiently large to bring the simulations close to the reported experimental observations. To sum up briefly the results, we showed that, if sufficiently large spanwise scales are accounted for, the lower limit

of bi-stability interval between the parallel (and non chaotic) vortex shedding and the three-dimensional, chaotic one lies close to $Re = 170$. In the same time we obtained a downward shift of the Strouhal number due to the three-dimensionality in good agreement with the Williamson's curve. As for the co-existence of the modes A and B, we showed that both of them are excited at the only bifurcation existing in this region of Reynolds numbers. What happens is that, due to the subcritical nature of the bifurcation, the linearly unstable mode A is submitted to strongly non-linear effects at its very onset. Its strong growth excites, via non-linear couplings, the mode B not only at the threshold of the linear instability but even down to the lower limit of the bi-stability interval. As a result the threshold of the existence of the mode B could never be observed and the lower Reynolds number limit of observations of its co-existence with the mode A is very fuzzy in the experimental literature, because, very likely, this limit depends on the level of the experimental noise. It can can be concluded that the onset of three-dimensionality in the cylinder wake presents the remarkable feature that a single bifurcation is sufficient to break all symmetries and trigger a full spatio-temporal chaos.

In Chapter 4 we attempted to transpose the results obtained in the configuration of the circular cylinder to that of an infinite NACA wing. In the process, we considered it useful to provide a more systematic investigation of two-dimensional regimes of the wake depending on both the Reynolds number and the angle of incidence. In this approach, we followed closely the method applied with success to the wake of the unheated and heated sphere by the team in which the present thesis has been completed. The numerical efficiency of the used code has made it possible to carry out a fairly complete parametric investigation in the interval of angle of incidences between zero and 12 degrees and for Reynolds numbers up to 10 000.

As most innovative we consider, however, the investigation of the transition to three-dimensionality. We carried out a fairly accurate linear stability analysis for angle of incidences ranging from 8 to 12 degrees. Similar results have, to our knowledge, never been published in this context. From the theoretical viewpoint it is valuable to know where the linear thresholds are situated and what the unstable modes look like. The numerical investigation might have been considered as completed at this point if there were not the results we obtained for the circular cylinder. The practical relevance of the linear stability analysis had to be examined in view of the potential effects of non-linearities and large spanwise scales. The obtained results seem, however, to indicate a significant difference between the wake of a profiled and a bluff body, such as a circular cylinder. The bifurcation giving rise to the unstable mode responsible for the transition to three-dimensionality is supercritical and the mode itself is closer to the mode B than the mode A. A closer look at the spatial distribution of the mode B shown in chapter 3 leads to the conclusion that this mode arises essentially in the boundary layer. It is not surprising that in the flow past profiled bodies where the boundary layers play a much more important role such a mode drives the whole dynamics. As a consequence, the subcriticality and the early transfer of energy to large spanwise scales being associated to the mode A in the bluff body wake, the behavior of the flow past profiled bodies might be different and the transtion to chaos more progressive.

The simulations with large spanwise periodicity at a slightly supercritical Reynolds number that have been preformed present a decay of subharmonic spanwise scales proving that,

in the case of a wing, the linear stability analysis of three-dimensionality is physically relevant in a non empty Reynolds number interval. This might be a good news for many direct numerical simulations. In the same time, the challenge of investigation of the effect of subharmonic scales is shifted to higher Reynolds numbers and will require a mobilization of significant numerical resources. The next aim of such an investigation would be the search for a new bifurcation at which subharmonic scales become unstable. Whatever this result, at high Reynolds numbers the subharmonic scales must be expected to be excited both for profiled and bluff bodies. In view of what we learned in the case of the circular cylinder wake the question can be raised whether simulations in idealized infinite geometries are simpler than in real three-dimensional ones.

Bibliography

Alam, M. & Sandham, N. D. 2000 Direct numerical simulation of 'short' laminar separation bubbles with turbulent reattachment. *J. Fluid Mech.* **410**, 1–28.

Barkley, D. & Henderson, R. D. 1996 Three-dimensional Floquet stability analysis of the wake of a circular cylinder. *J. Fluid Mech.* **322**, 215–241.

Barkley, D., Tuckerman, L.S. & M., Golubitsky 2000 Bifurcation theory for three-dimensional flow in the wake of a circular cylinder. *Physical Review E* **61**, 5247–5252.

Blackburn, H. M. & Lopez, J. M. 2003 On three-dimensinality quasiperiodic Floquet instabilities of two-dimensional bluff body wakes. *Physics of Fluids* **15**, L57–L60.

Blackburn, H. M., Marques, F. & Lopez, J. M. 2005 Symmetry breaking of two-dimensional time-periodic wakes. *J. Fluid Mech.* **522**, 395–411.

Bouchet, G., Mebarek, M. & Dušek, J. 2006 Hydrodynamic forces acting on a rigid fixed sphere in early transitional regimes. *European Journal of Mechanics, B/Fluids* **25**, 321–336.

Chassaing, P. 1997 *Mecanique des fludes*. Collection polytech de l' I. N.P. Tolouse.

Cooley, J. W. & Tukey, J. W. 1965 An algorithm for the machine calculation of complex fourier series. *Math. Comput.* **19**, 297–301.

Deng, Shutian, Jiang, Li & Liu, Chaoqun 2007 DNS for flow separation control around an airfoil by pulsed jets. *Computers & Fluids* **36**, 1040–1060.

Dušek, J. 1996 Spatial structure of the Bénard - von Kármán instability. *European Journal of Mechanics, B/Fluids* **15**, 619–650.

Dušek, J., Gal, P. Le & Fraunié, P. 1994 A numerical and theoretical study of the first Hopf bifurcation in a cylinder wake. *J. Fluid Mech.* **264**, 59–80.

Eisenlohr, H. & Eckelmann, H. 1988 Vortex splitting and its consequences in the vortex street wake of cylinders at low Reynolds number. *Physics of Fluids* **1**, 189–192.

Fischer, P.F. 1989 Spectral element solution of the navier-stokes equations on high performance distributed-memory parallel processors. PhD thesis, Massachussetts Institute of Technology.

Fischer, P. & Mullen, J. 2001 Filter-based stabilization of spectral element methods. *C.R. Acad. Sci. Paris* **332, Série I**, 265–270.

Ghidersa, B. & Dušek, J. 2000 Breaking of axisymetry and onset of unsteadiness in the wake of a sphere. *J. Fluid Mech.* **423**, 33–69.

Henderson, R. D. 1997 Nonlinear dynamics and pattern formation in turbulent wake transition. *J. Fluid Mech.* **352**, 65–112.

Henderson, R. D. & Barkley, D. 1996 Secondary instability in the wake of a circular cylinder. *Physics of Fluids* **8**, 1683–1685.

Hoarau, Y., Braza, M., Ventikos, Y. & Faghani, D. 2006 First stages of the transition to turbulence and control in the incompressible detached flow around a naca 0012 wing. *Int. J. Heat Fluid Flow* **27**, 878–886.

Hoarau, Y., Braza, M., Ventikos, Y., Faghani, D. & Tzabiras, G. 2003*a* Organized modes and the three-dimensional transition to turbulence in the incompressible flow around a naca 0012 wing. *J. Fluid Mech.* **496**, 63–72.

Hoarau, Y., Faghani, D., Braza, M., Perrin, R., Anne-Archard, D. & Ruiz, D. 2003*b* Direct numerical simulation of the three-dimensional transition to turbulence in the incompressi ble flow around a wing. *Flow and turbulence and combustion* **71**, 119–132.

Jenny, M. 2003 Etude de la transition au chaos d'une sphère en ascension ou en chute libre dans un fluide newtonien. PhD thesis, Université Louis Pasteur.

Jenny, M. & Dušek, J. 2004 Efficient numerical method for the direct numerical simulation of the flow past a single light moving spherical body in transitional regimes. *Journal of Computational Physics* **194**, 215–232.

Jeong, J. & Hussain, F. 1995 On the identification of a vortex. *J. Fluid Mech.* **285**, 69–94.

Johnson, T.A. & Patel, V.C. 1999 Flow past a sphere up to a Reynolds number of 300. *J. Fluid Mech.* **378**, 19–70.

Jones, L. E., Sandeberg, R. D. & Sandham, N. D. 2008 Direct numerical simulations of forced and unforced separation bubbles on an airfoil at incidence. *J. Fluid Mech.* **602**, 175–207.

Karniadakis, G. E. & Triantafyllou, G. S. 1992 Three-dimensional dynamics and transition to turbulence in the wake of bluff objects. *J. Fluid Mech.* **238**, 1–30.

Kotouč, M. 2008 Transition à la turbulence du sillage d'une sphère fixe ou libre en convection mixte. PhD thesis, Université Louis Pasteur, Strasbourg I.

Leweke, T. & Provansal, M. 1995 The flow behind rings: bluff body wakes without end effects. *J. Fluid Mech.* **288**, 265–310.

Leweke, T. & Williamson, C. H. K. 1998 Three-dimensional instabilities in wake transition. *European Journal of Mechanics, B/Fluids* **17**, 571–586.

Mittal, Sanjay & Saxena, Priyank 2002 Hysteresis in flow past a naca 0012 airfoil. *Computational methods in applied mechanics and engineering* **191**, 2179–2189.

Natarajan, R. & Acrivos, A. 1993 The instability of the steady flow past spheres and disks. *J. Fluid Mech.* **254**, 323–344.

Noack, B. R., Afanasiev, K., Morzynski, M., Tadmor, G. & Thiele, F. 2003 A hierarchy of low-dimensional models for the transient and post-transient cylinder wake. *J. Fluid Mech.* **497**, 335–363.

Noack, B. R., König, M. & Eckelmann, H. 1993 Three-dimensional stability analysis of the periodic flow around a circular cylinder. *Physics of Fluids* **5**, 1279–1281.

Ormières, D. & Provansal, M. 1999 Transition to turbulence in the wake of a sphere. *Phys. Rev. Lett.* **83**, 80–83.

Patera, A. 1984 A spectral element method for fluid dynamics: laminar flow in a channel expansion. *Journal of Computational Physics* **54** (3), 468–488.

Persillon, H. & Braza, M. 1998 Physical analysis of the transition to turbulence in the wake of a circular cylinder by three-dimensional Navier-Stokes simulation. *J. Fluid Mech.* **365**, 23–88.

Prandtl, L. 1905 Über Flüssigkeitsbewegung bei sehr kleiner Reibung. (Kratzer A. ed.). Verhandlungen des dritten internationalen Mathematiker-Kongresses in Heidelberg von 8. bis 13, August 1904. Leipzig: B. G. Teubner.

Roshko, A. 1954 On the development of turbulent wakes from vortex streets. *NACA Rep. 1191* **1191**, 1–25.

S.A. Orszag, A.T. Patera 1983 Secondary instability of wall bounded shear flows. *J. Fluid Mech.* **128**, 347–385.

Sandham, N. D. 2008 Transitional separation bubbles and unsteady aspects of aerfoil stall. *The Aeronautical Journal* **112**, 395–404.

Schlichting, H. 1955 *Boundary Layer Theory*. New York, McGraw-Hill.

Shan, Hua, Jiang, Li & Liu, Chaoqun 2005 Direct numerical simulation of flow separation around a naca 0012 airfoil. *Computers & Fluids* **34**, 1096–1114.

Shan, Hua, Jiang, Li, Liu, Chaoqun, Love, Michael & Maines, Brant 2008 Numerical study of passive and active flow separation control over a naca 0012 airfoil. *Computers & Fluids* **37**, 975–992.

Sheard, G. J., Thompson, M. C. & Hourigan, K. 2003 From sphere to circular cylinders: the stability and flow structures of bluff ring wakes. *J. Fluid Mech.* **492**, 147–180.

Stoevesandt, B., Shishkin, A., Peinke, J. & Wagner, C. 2006 Direct numerical simulation of the turbulent flow around an airfoil using spectral/hp method. European conference on computational fluid dynamics, TU delft, The Netherland.

Thompson, M. C., Hourigan, K. & Sheridan, J. 1996 Three dimensional instabilities in the wake of a circular cylinder. *Experimental Thermal and Fluid Science* **12**, 190–196.

Thompson, M. C., Leweke, T. & Williamson, C. H. K. 2001 The physical mechanism of transition in bluff body wakes. *Journal of Fluids and Structures* **15**, 607–616.

Tomboulides, A. G. & Orszag, S. A. 2000 Numerical investigation of transitional and weak turbulent flow past a sphere. *J. Fluid Mech.* pp. 45–73.

Williamson, C.H.K. 1988*a* Defining a universal and continuous Strouhal-Reynolds number relationship for the laminar vortex shedding of a circular cylinder at low Reynolds numbers. *Physics of Fluids* **31**, 2742–2744.

Williamson, C.H.K. 1988*b* The existence of two stages in the transition to three-dimensionality of a cylinder wake. *Physics of Fluids* **31**, 3165–3168.

Williamson, C.H.K. 1989 Oblique and parallel modes of vortex shedding in the wake of a circular cylinder at low Reynolds numbers. *J. Fluid Mech.* **206**, 579–627.

Williamson, C.H.K. 1992 The natural and forced formation of spot-like 'vortex dislocations' in the transtion of wake. *J. Fluid Mech.* **243**, 393–441.

Williamson, C. H. K. 1996*a* Mode a secondary instability in wake transition. *Physics of Fluids* **8**, 1680–1682.

Williamson, C. H. K. 1996*b* Three dimensional wake transition. *J. Fluid Mech.* **328**, 345–407.

Wu, Jie-Zhi, Lu, Xi-Yun, Denny, Andrew G., Fan, Meng & Wu, Jain-Ming 1998 Post-stall flow control on an airfoil by local unsteady forcing. *J. Fluid Mech.* **371**, 21–58.

Zhang, H., Fey, U., Noack, B. R., Koenig, M. & Eckelmann, H. 1995 On the transition of the cylinder wake. *Physics of Fluids* **7**, 779–794.